

GRAVITY GRADIENT INVERSIONS USING
UNSTRUCTURED TETRAHEDRAL MESHES

CASSANDRA TYCHOLIZ

Gravity Gradient Inversions using Unstructured Tetrahedral Meshes

by

©Cassandra Tycholiz

A Thesis submitted to the School of Graduate Studies
in partial fulfillment of the requirements
for the degree of

Master of Science

Department of Earth Sciences (Geophysics)

Memorial University of Newfoundland

March 2013

St. John's, Newfoundland



Abstract

Airborne gravity gradiometry is a rapidly growing field. The method is a multi-component technique that measures the spatial rate of change in the Earth's gravitational field. A limited number of inversion programs exist to provide an interpretation of the gravity gradient data and these programs rely on the use of rectilinear meshes. The objective of this project was to use unstructured tetrahedral meshes to recover the three dimensional distribution of the subsurface density contrast. The inversions were subject to a variety of geological constraints and different gravity gradient tensor component combinations. The results indicate that adding geological constraints improves the recovered density contrast models. The advantage of using an unstructured tetrahedral mesh over a rectilinear mesh is that surfaces from three dimensional geological Earth models can be directly incorporated as geological constraints to further refine recovered models. The results also indicate that incorporating additional gravity gradient components into the inversion improves the density contrast model by better defining the size and depth extent of the geologic units. The differences between the inversion models using single versus multiple components were less apparent as more geological constraints were added.

Acknowledgements

I would like to thank my supervisor Dr. Colin Farquharson for his advice, guidance, and encouragement. I would also like to like my committee member Dr. Charles Hurich for his advice and support. I am also grateful to Hormoz Jahandari for his advice on modifying the original gravity forward modelling program and to Dr. Peter Lelièvre for access to his modelling programs as well as his advice and support.

I am grateful to Vale for providing the geologic model that appears in Chapter 3 and the airborne data that appears in Chapter 4.

I would like to acknowledge receipt of an NSERC Scholarship, SEG Scholarship, and School of Graduate Studies for financial support which enabled me to carry out the work for this thesis.

Table of Contents

Abstract	ii
Acknowledgments	iii
Table of Contents	iv
List of Tables	ix
List of Figures	xi
1 Introduction	1
1.1 Gravity method	1
1.2 Geophysical modelling	2
1.2.1 Gravity gradient inversion	4
1.2.2 Geologically-constrained inversion	6
1.3 Voisey's Bay and Mushuau Intrusions	7
1.3.1 General geology	7
1.4 Thesis objectives and outline	9
2 Theory and Methodology	11
2.1 Gravity method	12
2.1.1 Gravitational attraction and potential	12

2.1.2	Gravity gradient	13
2.1.2.1	Units of measure	14
2.1.2.2	Density	14
2.1.2.3	Gravity gradient anomalies	16
2.1.3	Airborne gravity gradiometry	18
2.1.4	Terrain corrections	20
2.2	Geophysical Earth models	20
2.2.1	Mesh type	20
2.2.2	Generating unstructured tetrahedral meshes	21
2.3	Forward modelling	25
2.3.1	Solving the forward problem	25
2.3.2	Programming the forward problem	26
2.4	Minimum-structure inversion	28
2.4.1	Solving the inverse problem	28
2.4.2	Data misfit	29
2.4.3	Model objective function	30
2.4.4	Depth and distance weighting	31
2.4.5	Preparing inversions	32
2.4.6	Geological constraints	33
2.4.6.1	Types of geological constraints	33
2.4.6.2	Implementing geological constraints	34
3	Synthetic data inversions:	
	Voisey's Bay deposits	35
3.1	Overview	35
3.2	Creating the density model	36
3.3	Synthetic airborne gravity gradiometer data	39

3.4	Geologically-unconstrained inversion	40
3.4.1	U_{zz} inversion	43
3.4.2	U_{xx}, U_{xy}, U_{yy} inversion	44
3.4.3	U_{xx}, U_{yz}, U_{zz} inversion	46
3.4.4	$U_{xx}, U_{xy}, U_{xz}, U_{yy}, U_{yz}$ inversion	48
3.4.5	$U_{xx}, U_{xy}, U_{xz}, U_{yy}, U_{yz}, U_{zz}$ inversion	50
3.5	Geologically-constrained inversion: drill holes	54
3.5.1	U_{zz} inversion	54
3.5.2	U_{xx}, U_{xy}, U_{yy} inversion	56
3.5.3	U_{xx}, U_{yz}, U_{zz} inversion	58
3.5.4	$U_{xx}, U_{xy}, U_{xz}, U_{yy}, U_{yz}$ inversion	60
3.5.5	$U_{xx}, U_{xy}, U_{xz}, U_{yy}, U_{yz}, U_{zz}$ inversion	63
3.6	Geologically-constrained inversion: troctolite surface	67
3.6.1	Constrained example A	67
3.6.2	U_{zz} inversion	67
3.6.3	U_{xx}, U_{xy}, U_{yy} inversion	70
3.6.4	U_{xx}, U_{yz}, U_{zz} inversion	70
3.6.5	$U_{xx}, U_{xy}, U_{xz}, U_{yy}, U_{yz}$ inversion	72
3.6.6	$U_{xx}, U_{xy}, U_{xz}, U_{yy}, U_{yz}, U_{zz}$ inversion	72
3.6.7	Constrained example B	77
3.6.8	$U_{xx}, U_{xy}, U_{xz}, U_{yy}, U_{yz}, U_{zz}$ inversion	77
3.7	Geologically-constrained inversion: true model	79
3.7.1	Inversion results	79
3.8	Summary of results	81
3.8.1	Unstructured tetrahedral meshes	81
3.8.2	Geologically unconstrained versus constrained inversion	85

3.8.3	Single versus multiple component inversion	92
4	Real data inversions: Mushuau intrusion	98
4.1	Overview	98
4.2	Airborne gravity gradiometer data	100
4.3	Mushuau Intrusion inversions	101
4.3.1	Inversion results	103
4.4	Asini prospect inversions	105
4.4.1	U_{zz} inversion	105
4.4.2	U_{xx} , U_{xy} , U_{yy} inversion	107
4.4.3	U_{xx} , U_{yz} , U_{zz} inversion	109
4.4.4	U_{xx} , U_{xy} , U_{xz} , U_{yy} , U_{yz} inversion	110
4.4.5	U_{xx} , U_{xy} , U_{xz} , U_{yy} , U_{yz} , U_{zz} inversion	111
4.5	Sarah prospect inversions	114
4.5.1	Example 1	115
4.5.2	U_{zz} inversion	115
4.5.3	Example 2: Layered model	117
4.5.4	U_{zz} inversion	119
4.5.5	U_{xx} , U_{xy} , U_{yy} inversion	120
4.5.6	U_{xx} , U_{yz} , U_{zz} inversion	120
4.5.7	Example 3: Layered model and decimated data set	122
4.5.8	U_{xx} , U_{xy} , U_{xz} , U_{yy} , U_{yz} inversion	122
4.5.9	U_{xx} , U_{xy} , U_{xz} , U_{yy} , U_{yz} , U_{zz} inversion	122
4.6	Summary of results	126
4.6.1	Generating unstructured tetrahedral meshes	126
4.6.2	Geologically-unconstrained inversion	126
4.6.3	Single versus multiple component inversion	130

5	Conclusions	135
5.1	Geophysical modelling	135
5.2	Geological constraints and unstructured tetrahedral meshes	136
5.3	Single and multiple component inversions	137
	Bibliography	139
A	Forward modelling program: <i>gravity_fwd</i>	146
B	Inversion program: <i>vinv</i>	149
C	Voisey's Bay models	153
C.1	Forward modelling files	153
C.2	Data misfit versus model norm	153
C.3	Inversion files	154
D	Mushuau models	156
D.1	Coordinate transform	156
D.2	Data misfit versus model norm	156
D.3	Inversion files	158

List of Tables

2.1	Density range and average density for some common rock types and minerals.	15
2.2	Direction vectors for gravity gradient calculations (modified from Okabe, 1979).	25
3.1	Standard deviation of the data difference (E) for the geologically-unconstrained inversion results.	44
3.2	Maximum density contrast for the geologically-unconstrained inversion results.	46
3.3	Maximum density contrast for the inversion constrained using drill hole data.	56
3.4	Standard deviation of the data difference (E) for the inversion constrained using drill hole data.	58
3.5	Maximum density contrast for the inversion constrained using the troctolite surface.	68
3.6	Standard deviation of the data difference (E) for the inversion constrained using the troctolite surface.	68
3.7	Standard deviation of the data difference (E) and maximum density contrast (g/cm^3) for the six component inversions constrained using the troctolite surface.	79

3.8	Density range for the geologically-unconstrained, constrained using density data from three drill holes, and constrained using the troctolite surface.	93
4.1	The maximum tetrahedron volumes used in the layered model. . . .	118
4.2	Density range for the geologically-unconstrained Asini prospect inversions. Density values are in g/cm^3	133
4.3	Density range for the geologically-unconstrained Sarah prospect inversions. Density values are in g/cm^3	134
A.1	The <i>gravity_fwd.inp</i> input file used for forward modelling.	147
B.1	The <i>vinv.inp</i> input file.	150
B.2	The <i>gravity_inv.inp</i> input file used for minimum-structure inversion. .	151

List of Figures

1.1	The forward problem predicts the expected gravity response from a density model, whereas the inverse problem determines a density model from the measured gravity response.	3
1.2	Geologic map of the Voiseys' Bay and Mushuau Intrusions.	8
2.1	Gravity gradient patterns for a cube in a homogeneous half-space. . .	17
2.2	Comparison of the error levels across four airborne gravity gradiometer installations.	19
2.3	Comparison of rectilinear and unstructured discretization options. The rectilinear mesh has 256 cells and results in a pixellated representation. The unstructured mesh has 183 cells and efficiently generates the complicated geometry (modified from Lelièvre et al., 2012).	22
2.4	Screen-capture of the FacetModeller program for creation of 3D PPCs from cross sections.	24
3.1	Vertical north-south cross section through the Eastern Deeps deposit at 56580 m Easting.	37
3.2	Triangular facets are used to join the nodes together. The purple nodes are on the 56630 m cross section and the red nodes are on the 56580 m cross section.	38

3.3	Perspective view looking down to the north of the PPC for a 3D model based on the Voisey's Bay deposit.	39
3.4	The calculated gradiometer data observed above the Voisey's Bay deposit.	41
3.5	The noise contaminated gradiometer data observed above the Voisey's Bay deposit used for inversion.	42
3.6	A perspective view of the recovered model for the unconstrained inversion result using the U_{zz} component.	45
3.7	A perspective view of the recovered model for the unconstrained inversion result using the U_{xx} , U_{xy} , and U_{yy} components.	47
3.8	A perspective view of the recovered model for the unconstrained inversion result using the U_{xz} , U_{yz} , and U_{zz} components.	49
3.9	A perspective view of the recovered model for the unconstrained inversion result using the U_{xx} , U_{xy} , U_{xz} , U_{yy} , and U_{yz} components.	51
3.10	The predicted gradiometer data for the geologically-unconstrained inversion using six tensor components.	52
3.11	The data difference between the observed and predicted data for the geologically-unconstrained inversion using six tensor components.	53
3.12	A perspective view of the recovered model for the unconstrained inversion result using all six tensor components.	55
3.13	A perspective view of the recovered model using the U_{zz} component and density information from three drill holes.	57
3.14	A perspective view of the recovered model using the U_{xx} , U_{xy} , and U_{yy} components and density information from three drill holes.	59
3.15	A perspective view of the recovered model using the U_{xz} , U_{yz} , and U_{zz} components and density information from three drill holes.	61

3.16	A perspective view of the recovered model using the U_{xx} , U_{xy} , U_{xz} , U_{yy} , and U_{yz} components and density information from three drill holes.	62
3.17	The predicted gradiometer data for the six tensor component inversion using density information from three drill holes as the initial model.	64
3.18	The data difference between the observed and predicted data for the six component inversion using density information from three drill holes as the initial model.	65
3.19	A perspective view of the recovered model using all six tensor components and density information from three drill holes.	66
3.20	A perspective view of the recovered model using the troctolite surface as the initial model and the U_{zz} component.	69
3.21	A perspective view of the recovered model using the troctolite surface as the initial model and the U_{xx} , U_{xy} , and U_{yy} components.	71
3.22	A perspective view of the recovered model using the troctolite surface as the initial model and the U_{xx} , U_{yz} , and U_{zz} components.	73
3.23	A perspective view of the recovered model using the troctolite surface as the initial model and the U_{xx} , U_{xy} , U_{xz} , U_{yy} , and U_{yz} components.	74
3.24	The predicted gradiometer data for the six tensor component inversion using the troctolite surface as the initial model.	75
3.25	The data difference between the observed and predicted data for the six component inversion using the troctolite surface as the initial model.	76
3.26	A perspective view of the recovered model for the inversion result using the troctolite surface as the initial model and all six tensor components.	78
3.27	A perspective view of the recovered model for the inversion result using the troctolite surface as the initial model and all six tensor components. The bounds differ from the previous result.	80

3.28	The predicted gradiometer data for the six tensor component inversion using the true model as the initial model.	82
3.29	The data difference between the observed and predicted data for the six component inversion using the true model as the initial model. . .	83
3.30	A perspective view of the recovered model for the inversion result using the true model as the initial model and all six tensor components. . .	84
3.31	Vertical cross sections through Reid Brook (Easting 53800 m) highlight the effect geological-constraints have on the resulting models.	86
3.32	Vertical cross sections through Discovery Hill (Easting 54900 m) highlight the effect geological-constraints have on the resulting models. . .	87
3.33	Vertical cross sections through the Ovoid (Easting 55850 m) highlight the effect geological-constraints have on the resulting models.	88
3.34	Vertical cross sections through the Extension Zone (Easting 56100 m) highlight the effect geological-constraints have on the resulting models.	89
3.35	Vertical cross sections through Eastern Deeps (Easting 56600 m) highlights the effect geological-constraints have on the resulting models. .	90
3.36	Vertical cross sections through the Extension Zone (Easting 56100 m) highlights the differences between single and multi component inversion results for the geologically-unconstrained scenario.	95
3.37	Vertical cross sections through the Extension Zone (Easting 56100 m) highlights the differences between single and multi component inversion results for the geologically-constrained scenario using three drill holes.	96
3.38	Vertical cross sections through the Extension Zone (Easting 56100 m) highlights the differences between single and multiple component inversion results for the geologically-constrained scenario using the troctolite surface.	97

4.1	The Mushuau intrusion consists of two prospects: the Asini prospect to the north (A) and the Sarah prospect to the south (B through E) (modified from Li et al., 2000).	99
4.2	The flight path over the Mushuau intrusion. The blue dots show the flight lines, lines spacing and sampling along flight lines.	100
4.3	The terrain corrected gradiometer data observed above the Mushuau intrusion.	102
4.4	A perspective view of the recovered model for the unconstrained inversion result using the U_{zz} component.	104
4.5	The subset of gradiometer data used to perform inversion over the Asini prospect.	106
4.6	A perspective view of the recovered model for the unconstrained inversion results using the U_{zz} component showing the 0.20 g/cm^3 isosurface. 108	
4.7	A perspective view of the recovered model for the unconstrained inversion results using the U_{xx} , U_{xy} , U_{yy} components showing the 0.20 g/cm^3 isosurface.	109
4.8	A perspective view of the recovered model for the unconstrained inversion results using the U_{xz} , U_{yz} , U_{zz} components showing the 0.20 g/cm^3 isosurface.	110
4.9	A perspective view of the recovered model for the unconstrained inversion results using the U_{xx} , U_{xy} , U_{xz} , U_{yy} , U_{yz} components showing the 0.20 g/cm^3 isosurface.	111
4.10	The predicted gradiometer data for the six component inversion.	112
4.11	The data difference between the observed and predicted data for the six component inversion.	113

4.12	A perspective view of the recovered model for the unconstrained inversion results using the U_{xx} , U_{xy} , U_{xz} , U_{yy} , U_{yz} , U_{zz} components showing the 0.20 g/cm^3 isosurface.	114
4.13	The subset of gradiometer data used to perform inversion over the Sarah prospect.	116
4.14	A perspective view of the Sarah prospect recovered model for the unconstrained inversion results using the U_{zz} component. All cells below 0.15 g/cm^3 have been removed.	117
4.15	Vertical cross section through the layered model. The maximum tetrahedron volumes applied to each layer are listed in Table 4.1.	118
4.16	A perspective view of the Sarah prospect recovered model for the unconstrained inversion results using the U_{zz} component and the layered mesh. All cells below 0.15 g/cm^3 have been removed.	119
4.17	A perspective view of the Sarah prospect recovered model for the unconstrained inversion results using the U_{xx} , U_{xy} , U_{yy} components and the layered mesh.	121
4.18	A perspective view of the Sarah prospect recovered model for the unconstrained inversion results using the U_{xz} , U_{yz} , U_{zz} components and the layered mesh.	123
4.19	The decimated data set of gradiometer data used to perform inversion over the Sarah prospect.	124
4.20	A perspective view of the Sarah prospect recovered model for the unconstrained inversion results using the U_{xx} , U_{xy} , U_{xz} , U_{yy} , U_{yz} components and the layered mesh.	125
4.21	The predicted gradiometer data for the Sarah prospect six component inversion using the decimated data set.	127

4.22	The data difference for the Sarah prospect between the observed and predicted data for the six component inversion.	128
4.23	A perspective view of the Sarah prospect recovered model for the unconstrained inversion results using all six tensor components and the layered mesh.	129
4.23	Vertical cross sections through the Asini prospect (Northing 6251800 m).	132
C.1	Trade-off curve for Voisey's Bay inversions.	154
D.1	Trade-off curve for Asini prospect inversions.	157

Chapter 1

Introduction

1.1 Gravity method

The gravity method has long been used in exploration to identify and delineate targets of interest: changes in lithology give rise to density contrasts which in turn result in anomalous gravity measurements related to those changes (Telford et al., 1990; Reynolds, 1997). To quantify the density variations, measurements can either be made of the vertical component of gravity using a gravimeter or of the gravity gradient using a gradiometer. In the early 20th century, gravity gradiometry was the first potential field method used for oil exploration (Bell et al., 1997). Measurements were generally good to ± 1 E but collecting data was time consuming and costly: recordings could only be made at 2-3 stations per day at a cost of \$100 per station. Additionally, the results were difficult to interpret over complex geological structures. Technological developments in the easier to use gravimeter led to a decline in gravity gradient measurements in the 1930s. Gravimeter measurements were not as accurate as gradiometer measurements, but data could be collected faster and the results were easier to interpret (Bell et al., 1997). In the past few decades, technological innova-

tions have brought gravity gradiometry back to the forefront as an exploration tool (DiFrancesco et al., 2009).

1.2 Geophysical modelling

Geophysical modelling gives insight into the physical property distribution of the subsurface of the Earth. Modelling has progressed from using generalized formulas and characteristic curves (Nettleton, 1942) to complex computer algorithms. There are two problems that can be solved in geophysical modelling: the forward problem and the inverse problem (Figure 1.1). The forward problem predicts the expected geophysical response from a physical model, whereas the inverse problem determines a physical model from the measured geophysical response (West and Bailey, 1988; Oldenburg and Li, 2004). All modelling begins with the development of a geophysical Earth model.

Earth models are simplified models of the subsurface used for forward modelling and inversion. The models used in geophysical modelling are typically defined over a fixed grid. Each cell in the grid is assigned a uniform physical property value and defines the subsurface physical property distributions. The physical properties of the cell are free to change during the inversion process but the cell boundaries remain fixed.

The forward problem needs to be solved before the inverse problem. This involves calculating the predicted geophysical response assuming the sources and geophysical Earth models are known (Oldenburg and Li, 2004). For gravity data, the geophysical response is easily calculated from a model of densities based on the physics of potential fields (Nettleton, 1942; Telford et al., 1990). The predicted geophysical response can then be compared with the observed data. If the model is a reasonable fit, it is assumed

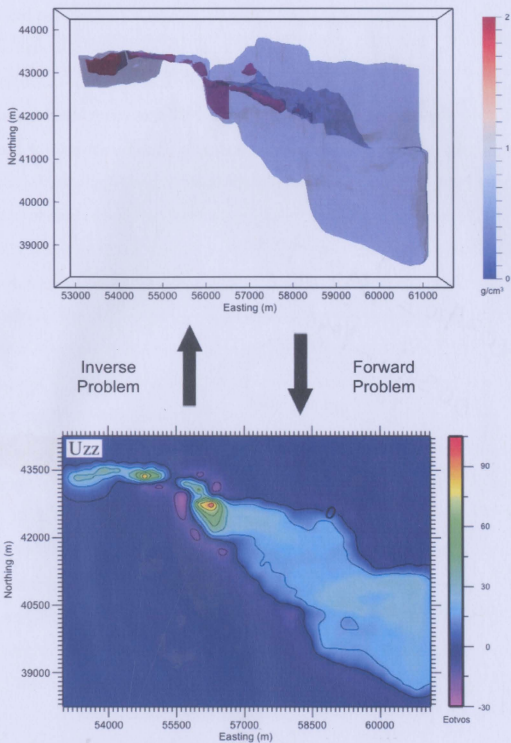


Figure 1.1: The forward problem predicts the expected gravity response from a density model, whereas the inverse problem determines a density model from the measured gravity response.

to resemble the real Earth model (West and Bailey, 1988). Forward modelling is a well-posed problem and a unique answer always exists.

The inverse problem involves calculating a physical property model from the geophysical data. A fundamental difficulty with geophysical inversion is non-uniqueness: the observations may be explained by an infinite number of models equally well. One approach to limit the number of possible models is to perform a minimum-structure inversion. Minimum-structure inversion has been successfully applied in the interpretation of electromagnetic, electric, magnetic, and gravity surveys (*e.g.* Constable et al., 1987; Li and Oldenburg, 1996, 1998). The goal of minimum-structure inversion is to recover the model parameters that give the least spatial variability, *i.e.* the smoothest model. The advantage of generating smooth models is that in theory any structures observed in the model must be real (West and Bailey, 1988). The disadvantage is the models obtained typically have a smeared shape and can bear little resemblance to the true geology.

A minimum-structure inversion is carried out by minimizing an objective function that contains two terms (Li and Oldenburg, 1996, 1998). The first term is the data misfit, which is a measure of how different the synthetic data is from the observed data. The second term is the model objective function, which is a measure of some overall character of the model. The minimization is an underdetermined problem, meaning there are more model parameters than the number of data. As a consequence, there are a number of different models that will fit the observed measurements within a misfit (West and Bailey, 1988).

1.2.1 Gravity gradient inversion

Few modelling programs are capable of inverting gravity gradient data and those that do rely on the use of a rectilinear mesh (*e.g.* Li, 2001; Zhdanov et al., 2004). This is

because the forward modelling is typically done using the expression of Nagy (1966), or similar, for the gravitational attraction of a rectangular prism. The 3D gravity gradient inversion program developed by Li (2001) is an adaptation of his earlier work on 3D inversion of magnetic data (Li and Oldenburg, 2003). Much of the magnetic algorithm is applicable because of the mathematical equivalence between magnetic data and gravity gradiometer data. The program constructs a minimum-structure density contrast distribution by minimizing a model objective function subject to the data and bound constraints on the model. The 3D gravity gradient inversion program developed by Zhdanov et al. (2004) is based on regularized focusing inversion. This program differs from Li (2001) because the focusing inversion constructs a sharper image of the geological target.

A major problem with rectilinear meshes is they are incompatible with triangulated surfaces used to represent lithological contacts in geological models. Using unstructured meshes to construct the physical property model resolves the incompatibility problem by incorporating any known geological surfaces directly. In order to use an unstructured mesh, a forward modelling program was developed using the expression of Okabe (1979), for the gravitational attraction of a tetrahedron.

Gravity gradient data has nine tensor components, five of which are independent. Several authors have investigated the use of single, multiple, or combinations of the components to solve the inverse problem. Li (2001) provides an example using all five independent tensor components (U_{xx} , U_{xy} , U_{xz} , U_{yy} , U_{yz}). Zhdanov et al. (2004) used a combination of $U_{uv} = (U_{xx} - U_{yy})/2$, U_{xy} , and U_{zz} and suggested that using U_{uv} and U_{xy} together produced better results than U_{zz} alone. Similarly, Li (2010) used a combination of U_{uv} and U_{xy} . Fullagar and Pears (2010) suggest that U_{zz} is the best component to use because of its relatively large amplitude and signal to noise ratio. They also suggest inverting the full tensor amplitude if all components

are available. Martinez et al. (2010) compared U_{zz} and a U_{xz} , U_{yz} , U_{zz} combination and showed an improved imaging of known geology when more components were incorporated. Martinez and Li (2011) compared U_{zz} ; U_{xy} and U_{uv} ; and U_{zz} , U_{xy} , and U_{uv} combinations and found improvements in the resulting model structure when using multiple components rather than just U_{zz} . Studies have noted that differences in component performance may be model dependent, *i.e.* results are dependent on the subsurface geometry and consequently do not have a widespread application (Zhdanov et al., 2004; Martinez et al., 2010; Pilkington, 2012).

1.2.2 Geologically-constrained inversion

As mentioned above, a fundamental difficulty with geophysical inversion of gravity data is non-uniqueness of solutions: the observations may be explained by an infinite number of models equally well. Mineral exploration produces large amounts of both geological and geophysical data; one approach to limit the number of possible inversion models is to include the geological data as geological constraints. Previous studies have shown that inversions can be constrained by geologically derived reference models; using this method produces subsurface models that are more consistent with the known geology; and reference models built with a even limited amount of geological information can improve inversion results (Ash, 2007; McGaughey, 2007; Farquharson et al., 2008; Williams, 2008; Lelièvre, 2009; Williams et al., 2009).

Information from surface samples, maps, core logs, cross sections, and volume interpretations can all be used as geological constraints. Geological data needs to be translated into an initial model and bound constraints. The initial model consists of the best estimate of the physical property value in each cell and default values are assigned where data is unavailable. Bound constraints impose a range of physical property values. This is useful if the physical property varies or is difficult to define

(Williams, 2008; Williams et al., 2009).

1.3 Voisey's Bay and Mushuau Intrusions

The examples in this study are all derived from the Voisey's Bay and Mushuau Intrusions on the east coast of Northern Labrador, Canada, but the techniques and approaches presented here are equally applicable to other areas. The Voisey's Bay and Mushuau Intrusions boast several key characteristics that make them suitable for a study of geologically-constrained inversion:

- A pronounced gravity gradient signature
- A variety of rock types with small to large density contrasts
- Well mineralized and understood localities (Voisey's Bay deposits) as well as areas of lesser known rocks with potential for additional sulphide mineralization (Mushuau Intrusion)
- Availability of geological and gravity gradient data courtesy of Vale

1.3.1 General geology

Northern Labrador consists of two contrasting Precambrian structural provinces: the Archean Nain province and the Archean and Paleoproterozoic rocks of the Churchill Province (Kerr and Ryan, 2000; Ryan, 2000). These provinces are separated by a continental suture zone associated with the 1.85 Torngat orogen. The Nain Plutonic Suite straddles the suture and acts as a stitching batholith for the Nain-Churchill boundary (Huminicki et al., 2008; Evans-Lamswood et al., 2000; Ryan, 2000).

The 1.333 Ga Voisey's Bay and the 1.313 Ga Mushuau Intrusions are located within the central portion of the Nain Plutonic Suite (Li et al., 2000). The Voisey's

Bay Intrusion is located approximately 35 km southwest of Nain and the Mushuau Intrusion is located approximately 10 km to the north of the Voisey's Bay Intrusion (Figure 1.2).

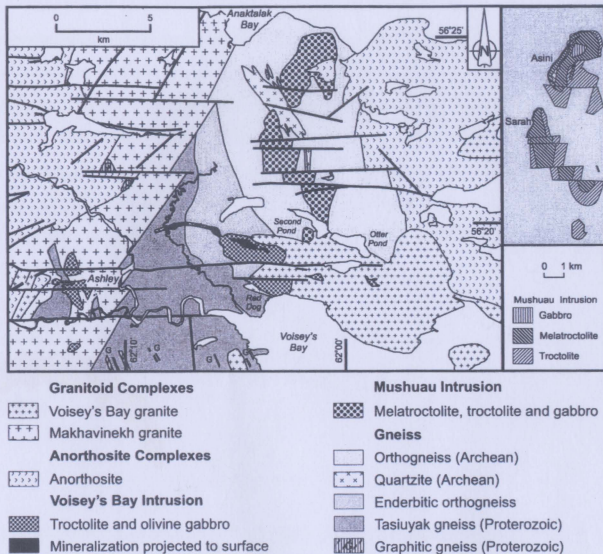


Figure 1.2: Geologic map of the Voisey's Bay and Mushuau Intrusions (Li et al., 2000).

The Voisey's Bay Intrusion hosts several Ni-Cu-Co deposits (Reid Brook Zone, Discovery Hill, Mini-Ovoid, Ovoid, Southeast Extension, and Eastern Deeps). The deposits occur within a troctolite sheet and dyke complex of the Nain Plutonic Suite (Huminicki et al., 2008; Evans-Lamswood et al., 2000; Ryan, 2000). The troctolites

are in turn mostly hosted by Paleoproterozoic enderbitic orthogneiss; the troctolites in the Reid Brook region are hosted by Tasiuyak gneiss (Huminicki et al., 2008; Rawlings-Hinchey et al., 2003).

The Ovoid is the main sulphide deposit currently being mined. It is an ellipsoidal massive sulphide lens with horizontal dimensions of 650 by 350 m and a maximum depth extent of 120 m. Density values in and around the Ovoid vary from less than 3.2 g/cm^3 to greater than 4.6 g/cm^3 . A general correlation exists between the sulphide content and density. Mean densities less than 3.2 g/cm^3 are associated with less than 15% sulphides, densities between 3.2 and 4.6 g/cm^3 are associated with 40–75% sulphides, and densities greater than 4.6 g/cm^3 are indicative of massive sulphides (Ash, 2007; Farquharson et al., 2008).

The Mushuau Intrusion consists of two zones of melatroctolite, troctolite, and gabbro: the Sarah prospect and the Asini prospect. The prospects are hosted by Archean orthogneiss. The mineral potential of the Mushuau Intrusion is poorly constrained, but minor magmatic sulphides are known to occur in the Sarah prospect (Li et al., 2000).

1.4 Thesis objectives and outline

The purpose of this thesis was to investigate 3D inversions of airborne gravity gradient data. The goals of this study were threefold: (i) develop a forward modelling program for gravity gradient data capable of using an unstructured tetrahedral mesh; (ii) further examine the utility of single and multiple component inversions; and (iii) demonstrate how unstructured tetrahedral meshes can be used to prescribe geological constraints. Chapter 2 is an overview of the gravity method, geophysical Earth models, forward modelling, and minimum-structure inversion. The Voisey's Bay syn-

thetic inversion results are presented and discussed in Chapter 3. The synthetic data inversions are performed using five different tensor component combinations to demonstrate the advantages and disadvantages of single and multiple component inversions. The synthetic inversions also show the benefits of including geological constraints in gravity gradient inversions. The Mushuau Intrusion inversion results are presented and discussed in Chapter 4. The real data inversions are used to further investigate the advantages and disadvantages of single and multiple component inversions. Geologically constrained inversions were not investigated because geological data was not provided. Chapter 5 presents the concluding remarks on the merits and drawbacks of using unstructured tetrahedral meshes to prescribe geological constraints; and of using single or multiple tensor components for gravity gradient inversions.

Chapter 2

Theory and Methodology

This chapter contains an overview of the gravity method, geophysical Earth models, forward modelling, and minimum-structure inversion. The gravity method measures changes in the Earth's gravitational field. A discussion of the relevant theory, units of measure, density, anomaly patterns, data acquisition, and terrain corrections is included. Geophysical Earth models are used for forward modelling and inversion. Unstructured tetrahedral meshes are used to discretize the modelling region and a discussion of their generation and storage in computer memory is included. The forward problem is solved using an expression for the gravitational attraction of a tetrahedron. The program *gravity_fwd* is used for generating synthetic gravity gradiometry data sets (Appendix A). The inverse problem is solved by constructing a minimum-structure inversion. The program *vinv* (Versatile INVersion code) is used for solving the inverse problem (Appendix B). The program *vinv* is capable of incorporating global mathematical constraints, such as depth or distance weighting, as well as located geological-constraints. Both types of constraints are necessary to recover geologically realistic models.

2.1 Gravity method

2.1.1 Gravitational attraction and potential

The gravity method is based on two laws derived by Sir Issac Newton: the Universal Law of Gravitation and the Second Law of Motion. Newton proposed that the force of attraction between two bodies of mass is inversely proportional to the square of the distance between the centres of mass and directly proportional to the product of the two masses (Telford et al., 1990; Blakely, 1996; Reynolds, 1997):

$$F = \gamma \frac{Mm}{r^2} \quad (2.1)$$

where γ is the Universal Gravitational constant equal to $6.672 \times 10^{-11} \text{ m}^3/\text{kg}\cdot\text{s}^2$ in SI units; M is the mass at $P_2(x, y, z)$; m is the mass at $P_1(x', y', z')$; the masses are separated by a distance $r = [(x - x')^2 + (y - y')^2 + (z - z')^2]^{\frac{1}{2}}$.

Newton's Second Law of Motion states that a force is equal to mass times acceleration:

$$F = ma \quad (2.2)$$

Acceleration in the vertical direction is due to gravity and Equation 2.2 becomes:

$$F = mg \quad (2.3)$$

By equations (2.1) and (2.3), the acceleration of gravity is (Telford et al., 1990; Blakely, 1996; Reynolds, 1997):

$$g = \gamma \frac{M}{r^2} \quad (2.4)$$

Gravitational acceleration is a conservative field; a conservative field is one in which the amount of work required to move from P_1 to P_2 is independent of the path

taken between the points (Blakely, 1996). It can be represented as the gradient of a scalar potential U , known as Newtonian Potential:

$$g(P_1) = \nabla U(P_1) \quad (2.5)$$

and

$$U(P_1) = \gamma \frac{m}{r} \quad (2.6)$$

For a continuous distribution of mass m Equation 2.6 becomes

$$U(P_1) = \gamma \int_V \frac{dm}{r} = \gamma \int_V \frac{\rho(P_2)}{r} dv \quad (2.7)$$

where v is the volume and ρ is the density of the mass m .

2.1.2 Gravity gradient

Gravity gradient data is multi-component data that measures the change in the gravitational acceleration vector between two points on the Earth's surface *i.e.* it describes the spatial variation of the gravity field.

The full gravity gradient tensor consists of nine components $U_{kl} = \partial^2 U / \partial k \partial l$, where k and l are one of x , y , or z (Pedersen and Rasmussen, 1990; Murphy, 2004):

$$\mathbf{U} = \begin{bmatrix} U_{xx} & U_{xy} & U_{xz} \\ U_{yx} & U_{yy} & U_{yz} \\ U_{zx} & U_{zy} & U_{zz} \end{bmatrix} \quad (2.8)$$

Only five of these components are independent for two reasons. First, gravity is a conservative field and therefore the gradient tensor is symmetric, *i.e.* $U_{kl} = U_{lk}$. Second, for measurements taken above the surface of the Earth, the gravitational

potential obeys the Laplace equation (Pedersen and Rasmussen, 1990):

$$\nabla^2 U(P_1) = \frac{\partial^2 U}{\partial x^2} + \frac{\partial^2 U}{\partial y^2} + \frac{\partial^2 U}{\partial z^2} = 0 \quad (2.9)$$

and the diagonal element U_{zz} is equal to the negative sum of U_{xx} and U_{yy} . Thus, the gradient tensor has five independent components usually taken as U_{xx} , U_{xy} , U_{xz} , U_{yy} , and U_{yz} (Pedersen and Rasmussen, 1990; Murphy, 2004). In practice, the U_{zz} component is typically given, even if both U_{xx} and U_{yy} are also given, because it is the most intuitive to interpret.

2.1.2.1 Units of measure

The normal acceleration due to gravity at the surface of the Earth is 980 cm/s² or 9.80 m/s². The c.g.s. unit of acceleration due to gravity is the Gal where 1 Gal = 1 cm/s². The Gal is named in honour of Galileo who first conducted experiments to measure the acceleration due to gravity (Reynolds, 1997). Gravity anomalies are generally small compared to the normal surface gravity value of 980 cm/s² and the milliGal is often used where 1 mGal = 10⁻³ Gal (Fowler, 2005). The gravity gradient is measured in units of Eotvos (E) where 1 E = 0.1 mGal/km. The Eotvos is named in honour of Hungarian physicist Loránd Eötvös who developed a torsion balance capable of measuring both the horizontal derivative of the horizontal field and the derivative of the vertical field (Bell and Hansen, 1998).

2.1.2.2 Density

Gravity measurements are sensitive to changes in density. Table 2.1 shows densities for a selection of common rocks and metallic minerals. The maximum variation in density between different rocks and minerals is 2 g/cm³. This is a very small change,

Table 2.1: Density range and average density for some common rock types and minerals (modified from Reynolds, 1997).

Material	Density range (g/cm ³)	Average density (g/cm ³)
<i>Sedimentary rocks</i>		
Clay	1.63–2.60	2.21
Gravel	1.70–2.40	2.0
Silt	1.80–2.20	1.93
Soil	1.20–2.40	1.92
Sand	1.70–2.30	2.0
Sandstone	1.61–2.76	2.35
Shale	1.77–3.20	2.4
<i>Igneous rocks</i>		
Rhyolite	2.35–2.70	2.52
Granite	2.50–2.81	2.64
Andesite	2.40–2.80	2.61
Syenite	2.60–2.95	2.77
Basalt	2.70–3.30	2.99
Gabbro	2.70–3.50	3.03
<i>Metamorphic rocks</i>		
Schist	2.39–2.90	2.64
Gneiss	2.59–3.00	2.8
Phyllite	2.68–2.80	2.74
Slate	2.70–2.90	2.79
Granulite	2.52–2.73	2.65
Amphibolite	2.90–3.04	2.96
Eclogite	3.20–3.54	3.37
<i>Metallic minerals</i>		
Copper	no data	8.7
Silver	no data	10.5
Gold	15.6–19.4	17
Pyrite	4.9–5.2	5
Cobaltite	5.8–6.3	6.1
Galena	7.4–7.6	7.5

especially when compared to the range of other physical properties, *e.g.* magnetic susceptibility ($\sim 10^5$), electrical conductivity ($\sim 10^{10}$), and radioactivity (~ 100) (Telford et al., 1990).

2.1.2.3 Gravity gradient anomalies

Gravity gradient data gives information on the size and shapes of anomalous bodies. In addition, different tensor components give different information of the geological attributes of the subsurface. A typical gravity gradient pattern for a dense block in a homogeneous half-space is shown in Figure 2.1 using a right-hand coordinate system where x is North, y is East, and positive z points downwards. The dense block is 100 by 100 by 100 m and is centred at 250 m East and 250 m North. The top surface of the block is located at a depth of 50 m. The horizontal components are used to define edges of geological bodies and map geological contacts (Murphy, 2004). The U_{xx} component outlines the northern and southern edges of the block in a half-space. Similarly, the U_{yy} component highlights the eastern and western edges. The U_{xz} component divides the block into northern and southern halves along the zero line between adjacent high and low values. Similarly, the U_{yz} component divides the block into eastern and western halves. The U_{xz} and U_{yz} components can be used to identify linear features such as faults and lithological contacts. The U_{xy} component shows opposite highs and lows that point to the centre of mass and highlight the corners of the block. The vertical component, U_{zz} , is most similar to the vertical component of gravity, U_z . It maps the density changes and is used to estimate depth and predict the composition of the target (Murphy, 2004).

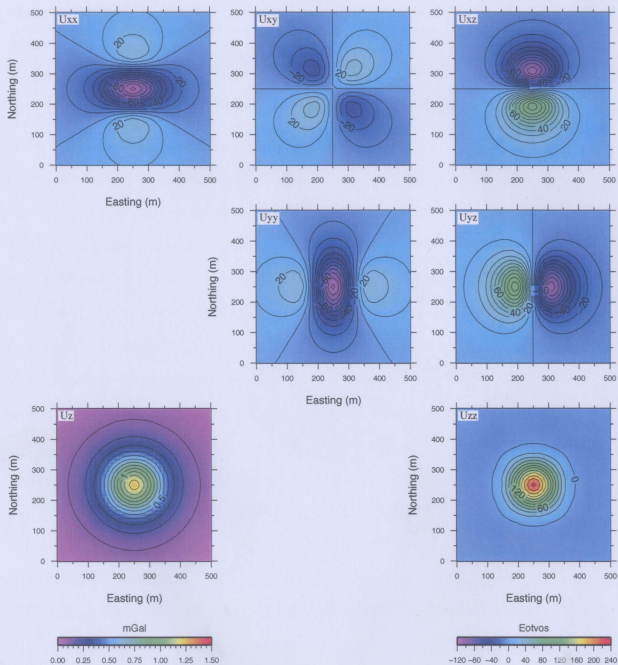


Figure 2.1: Gravity gradient pattern for a dense cube in a homogeneous half-space using a right-hand coordinate system where x is North, y is East, and positive z is downwards. The contour interval is 10 E for U_{xx} , U_{xy} , U_{xz} , U_{yy} , U_{yz} and 20 E for U_{zz} . The vertical component of gravity, U_z is shown for comparison. The contour interval is 0.1 mGal.

2.1.3 Airborne gravity gradiometry

The improvement in gravity instrumentation since the 1980s allows airborne gravity surveys to be undertaken routinely and with a high degree of accuracy. Airborne measurements consist of taking gradiometers into airplanes and helicopters (Nabighian et al., 2005). Two advantages of airborne surveying include the ability to access remote areas which were previously inaccessible and the ability to cover large areas quickly (Reynolds, 1997; Nabighian et al., 2005). The main problem with airborne gravity surveying and moving-platform surveys in general is large disturbing accelerations that result from vehicle motion. These accelerations are a function of external conditions, *e.g.*, wind and turbulence; the platform type and model; the navigational system; and the type of gravity system (Nabighian et al., 2005). This is one of the reasons airborne gradiometry is preferred to gravimetry: gravity gradiometry is not as susceptible to the aircraft accelerations because the same accelerations are measured by two accelerometers. When forming the difference, the acceleration cancels in the gravity gradient measurement (Hansen, 1999).

All commercial gravity gradiometry systems are based on Lockheed Martin technology: ARKeX uses their BlueQube system which consists of a Lockheed Martin Full Tensor Gradiometer; Bell Geospace uses their Air-FTG system which again consists of a Lockheed Martin Full Tensor Gradiometer; and Fugro Airborne Surveys uses the BHPBilliton FALCON system (Dransfield, 2007; DiFrancesco et al., 2009).

Dransfield (2007) provides a comparison of the error levels for the Air-FTG system flown in a Caravan and airship and the Falcon system flown in a Caravan and helicopter (Figure 2.2). The comparison is based on published information from Hatch et al. (2006); Boggs et al. (2007); Dransfield (2007); and Murphy et al. (2007). The noise is presented as the power density calculated by squaring the noise density and multiplying by the survey speed (Murphy et al., 2007). Overall, the Air-FTG system

flown in a Caravan has the highest and most variable error due to its increased sensitivity to aircraft motion. Using an airship in place of the Caravan results in lower error because the airship is very stable and very slow. The Falcon system flown in a Caravan has lower noise than the Air-FTG system due to its lower sensitivity to aircraft motion. The Falcon system flown in a helicopter has similar noise power density to the airship-borne Air-FTG. However, the ability of the helicopter to fly lower has been ignored; flying lower results in greater sensitivity to near-surface geology (Dransfield, 2007).

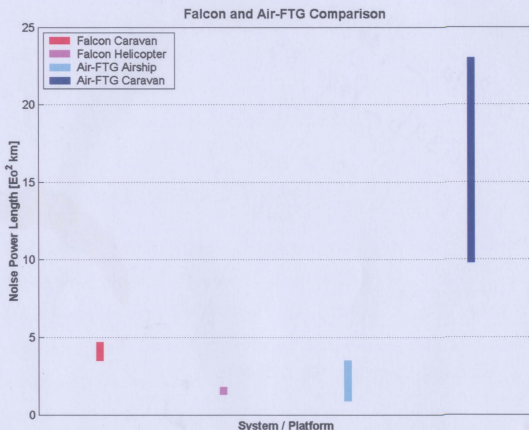


Figure 2.2: Comparison of the error levels across four airborne gravity gradiometer installations. The comparison is given in noise power density where lower noise power density corresponds to better sensitivity and resolution (Dransfield, 2007).

2.1.4 Terrain corrections

Gravity gradient measurements do not require multiple corrections to the measured data in order to obtain the anomaly values, unlike vertical gravity measurements. However, gravity gradient data is highly sensitive to terrain and as such the largest signal in a gravity gradient survey is often due to the terrain (Boggs and Dransfield, 2004; Dransfield, 2007); removing the terrain is an important step in reducing the data to an interpretable product (Martinez and Li, 2011). The density value used to remove the terrain effect is important. If the density value is too high then signal from the target may be removed. If the density value is too low then it will fail to fully remove the terrain effect (Martinez and Li, 2011). Additionally, the accuracy of the elevation data and the navigation data is important. Errors in either of these data sets can introduce large errors in the gravity gradient data (Dransfield, 2007).

2.2 Geophysical Earth models

The Earth model is a 3D spatial variation of anomalous density, *i.e.* $\Delta\rho(x, y, z)$. The density distribution is discretized into an unstructured tetrahedral mesh. The tetrahedral cell boundaries are fixed (*i.e.* their locations are not parameters in the inversion) and the value of anomalous density in each tetrahedral cell is constant. In the forward problem, the anomalous density values are known whereas in the inversion problem the anomalous density values are unknown.

2.2.1 Mesh type

Geological Earth models use triangulated surfaces to represent geological contacts. Triangulated surfaces are flexible enough to mimic complicated subsurface boundaries between the geological regions. The geological contacts can be determined from

drilling and surface mapping (Bosch and McGaughey, 2001; McGaughey, 2007; Fulagar and Pears, 2007).

Geophysical Earth models typically use a rectilinear mesh because numerical modelling can take advantage of the underlying mesh structure. However, rectilinear meshes have some distinct disadvantages: no matter how fine the discretization rectilinear meshes always give a pixellated model (Figure 2.3a); and rectilinear meshes are always incompatible with geological models that use surfaces to represent geological boundaries (Lelièvre et al., 2012).

Discretizing the subsurface using unstructured meshes in place of rectilinear meshes provides several advantages (Lelièvre et al., 2010): unstructured meshes can accurately and efficiently describe complex contacts; and they significantly reduce the size of forward and inverse problems (Figure 2.3b). However, there are also some major disadvantage of working with unstructured grids: there is the increased computing demands due to the limited availability of compression codes; and the process for producing unstructured meshes is more complex and time consuming.

2.2.2 Generating unstructured tetrahedral meshes

There are many publicly available software packages for generating unstructured meshes. This project makes use of Triangle (Shewchuk, 1996, 2002) to generate triangular 2D meshes and TetGen (Si and Gartner, 2004, 2005; Si, 2007) to generate tetrahedral 3D meshes.

TetGen generates 3D tetrahedral meshes from piecewise polygonal complexes (PPC); a PPC consists of non-intersecting planar polygonal facets. The meshing algorithm creates a volumetric mesh by subdividing the PPC facets into triangles. The triangles become the faces of the tetrahedral cells in the mesh. In an exploration scenario, the PPC would contain surfaces defining the boundary of the modelling region, the

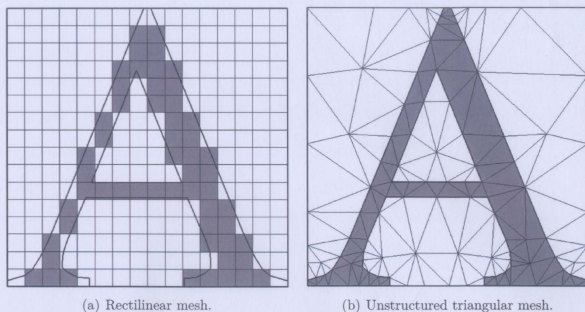


Figure 2.3: Comparison of rectilinear and unstructured discretization options. The rectilinear mesh has 256 cells and results in a pixellated representation. The unstructured mesh has 183 cells and efficiently generates the complicated geometry (modified from Lelièvre et al., 2012).

topography, and any known subsurface geological contacts.

A PPC is stored in a *poly* file. The *poly* file consists of four parts: a list of nodes, a list of facets, a list of holes, and a list of regions. The node list keeps an inventory of the minimum number of nodes to define a PPC. The facet list stores information on how the nodes are connected to create faces. The region attribute list identifies different regions in the PPC and can be used to assign a numerical identifier to the different rock units in a model.

Creating a PPC for a simple model, such as a block, is a straightforward process. In this case, the PPC would consist of eight nodes defining the corners and six square facets. It is difficult to create PPCs for geologically realistic models. In this case, FacetModeller can be used. FacetModeller is a graphical user interface for creating and editing PPCs; it was developed by Gary Blades as part of the High Performance Computing for Geophysical Applications project at Memorial University of

Newfoundland. The platform consists of a 2D working window and a 3D viewer window (Figure 2.4). Nodes are created and edited from georeferenced cross sections in the 2D working window. The cross sections can be in the x, y, or z planes. Triangular facets are used to join the cross sections together. The 3D viewer window lets the user visualize all or part of the model being created.

Several command line switches are used to generate a mesh (Si, 2007). The *-p* flag tetrahedralizes a PPC and outputs three files: *node*, *ele*, and *face*. A *node* file contains a list of three-dimensional points in Cartesian coordinates. An *ele* file contains a list of tetrahedra; each tetrahedron consists of four nodes representing the corner vertices. A *face* file contains a list of triangular faces. The *-p* flag can be used in combination with the *-q* or *-a* flags to generate a quality tetrahedral mesh. The *-q* flag applies a minimum radius-edge ratio and the *-a* flag applies a maximum tetrahedron volume constraint. Different volume constraints can be added to different regions in the mesh. The *-A* flag assigns attributes to identify tetrahedra in certain regions (*e.g.* assign rock properties). The *-n* flag is used to output tetrahedra to a *neigh* file. A *neigh* file can be used to store additional information about the mesh; it specifies neighbour tetrahedral cells. Each cell will have four neighbours except for those located on the boundary of a mesh.

In the case of forward modelling and inversion, data and model values need to be stored. For example, when solving the gravity gradient problem, each cell needs to be assigned a constant density contrast. The density contrast can be assigned as an attribute to each cell.

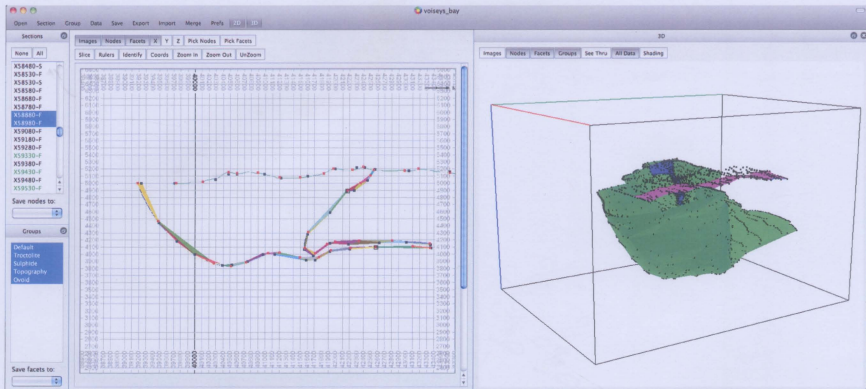


Figure 2.4: Screen-capture of the FacetModeller program for creation of 3D PPCs from cross sections. The left panel overlays two north-south cross sections of the Voisey's Bay deposit. The right panel shows a 3D perspective view of the Voisey's Bay deposit as it is being built from east-to-west. Triangular facets can be coloured randomly or coloured according to predefined groups. In this example, the troctolite is coloured green, the sulphide is coloured blue, and the surface is coloured fuchsia.

2.3 Forward modelling

2.3.1 Solving the forward problem

To solve the forward problem, it is first assumed that a distributed density contrast ρ inside a volume V is the source of gravity gradient measurements above the surface of the Earth. The gravity gradient is given by (Okabe, 1979):

$$U_{kl} = -\gamma \int_V \nabla[\nabla(\rho u) \cdot \mathbf{k}] \cdot \mathbf{l} dV \quad (2.10)$$

where γ is the gravitational constant, $u = -(x^2 + y^2 + z^2)^{-1/2}$, and the unit direction vectors \mathbf{k} and \mathbf{l} are, $\mathbf{k} = (k_x, k_y, k_z)$ and $\mathbf{l} = (l_x, l_y, l_z)$. The unit direction vectors used in the ordinary computation are shown in Table 2.2.

Table 2.2: Direction vectors for gravity gradient calculations (modified from Okabe, 1979).

Component	k_x	k_y	k_z	l_x	l_y	l_z
U_{xx}	1	0	0	1	0	0
U_{xy}	1	0	0	0	1	0
U_{xz}	1	0	0	0	0	1
U_{yy}	0	1	0	0	1	0
U_{yz}	0	1	0	0	0	1
U_{zz}	0	0	1	0	0	1

Next, it is assumed gravity gradient data is available as a set of discrete observation points, $\mathbf{d} = (d_1, d_2, d_3, \dots, d_M)^T$ where M is the total number of data points. If six tensor components are measured at p locations, then $M = 6p$. The density distribution is discretized into a set of tetrahedral cells for numerical calculation. In the forward problem, each cell has a known constant density contrast. The model is denoted as $\Delta\rho = (\Delta\rho_1, \Delta\rho_2, \Delta\rho_3, \dots, \Delta\rho_N)$ where N is the total number of cells in the

model. Then, the forward modelling is given by:

$$\mathbf{d} = \mathbf{G}\boldsymbol{\rho} \quad (2.11)$$

where the sensitivity matrix \mathbf{G} relates the data to the model vector. The elements g_{ij} of \mathbf{G} quantify the contribution of the j th cell to the i th datum; the sensitivity matrix only depends on the geometry of the problem and is independent of the density contrast, $\Delta\rho_j$.

Solving the forward modelling becomes the evaluation of the matrix-vector product in Equation 2.11. The forward problem requires the calculation of each element of the sensitivity matrix, multiplication with the corresponding density values, and summation over all the cells in the model. This process becomes computationally expensive for large problems.

2.3.2 Programming the forward problem

The program *gravity_fwd* is used to solve the forward problem. It was written by Dr. Peter Lelièvre and can be used to generate the vertical component of gravity, the gravity gradient tensor, or magnetic data. The portion of the program used to generate the vertical component of gravity was written by Hormoz Jahandari, a Ph.D Candidate in Dr. Colin Farquharson's research group. Hormoz Jahandari's program was then modified to generate the gravity gradient by the author (Appendix A). The program requires an input file to specify the parameters of the subsurface of the area of interest. The contents of an example file is described in Appendix A.

The gravity gradient due to a tetrahedron of uniform density can be determined by summation over a finite number of edges j and facets i using the expression derived

by Okabe (1979):

$$U_{kl} = \gamma\rho \sum_{i=1}^4 \sum_{j=1}^3 l^i \mathbf{n}_i L_j(i) \quad (2.12)$$

where the direction vector \mathbf{n} specifies the outward normal on the facet i and:

$$L_j(i) = \left[(M_Y \cos \psi - M_X \sin \psi) \cdot \ln[\xi + (\xi^2 + \eta^2 + Z^2)^{1/2}] + M_Z \tan^{-1} \frac{-\xi\eta + (\eta^2 + Z^2) \tan \psi}{Z(\xi^2 + \eta^2 + Z^2)^{1/2}} \right]_{\xi_j}^{\xi_{j+1}} \quad (2.13)$$

Equation 2.13 contains two coordinate system transformations. The first transformation is from the observation Cartesian system (x, y, z) to a tetrahedron surface Cartesian system (X, Y, Z) in which the Z -direction is aligned with the outward normal on the facet i . The transformation is achieved by counterclockwise rotation through angles θ and ϕ :

$$\begin{bmatrix} X \\ Y \\ Z \end{bmatrix} = \begin{bmatrix} \cos\phi & 0 & -\sin\phi \\ 0 & 1 & 0 \\ \sin\phi & 0 & \cos\phi \end{bmatrix} \begin{bmatrix} \cos\theta & \sin\theta & 0 \\ -\sin\theta & \cos\theta & 0 \\ 0 & 0 & 1 \end{bmatrix} \begin{bmatrix} x \\ y \\ z \end{bmatrix} \quad (2.14)$$

In the surface Cartesian system, Z is constant over the facet i . The second transformation is to an edge Cartesian system (ξ, η) achieved by counterclockwise rotation through angle ψ :

$$\begin{bmatrix} \xi \\ \eta \end{bmatrix} = \begin{bmatrix} \cos\psi & \sin\psi \\ -\sin\psi & \cos\psi \end{bmatrix} \begin{bmatrix} X \\ Y \end{bmatrix} \quad (2.15)$$

In the edge Cartesian system, η is constant over the edge j . Finally, M_X , M_Y , and

M_Z are defined as:

$$\begin{aligned}M_X &= (k_x \cos \theta + k_y \sin \theta) \cos \phi - k_z \sin \phi \\M_Y &= -k_x \sin \theta + k_y \cos \theta \\M_Z &= (k_x \cos \theta + k_y \sin \theta) \sin \phi + k_z \cos \phi\end{aligned}\tag{2.16}$$

2.4 Minimum-structure inversion

2.4.1 Solving the inverse problem

The program *vinv* is used to solve the inverse problem. It was written by Dr. Peter Lelièvre and can be used for single (vertical gravity data, gravity gradient data, magnetic data, or first-arrival travel time data) or joint data inversions (vertical gravity data and first-arrival seismic wave travel time data). The program requires a number of input files to specify the parameters of the subsurface of the area of interest. The contents of example files are described in Appendix B.

To solve the inverse problem, it is assumed a set of M gravity gradient data points are available. The objective is to construct the corresponding subsurface density contrast distribution. The modelling region is divided into a set of tetrahedral cells where the density is constant across each cell. In the geologically-unconstrained inverse problem, the density contrast for each cell is unknown and set to a default value of 0 g/cm^3 .

A major problem with geophysical inversion is that it is ill-posed, under-constrained, and non-unique. In order to deal with the non-uniqueness, a minimum-structure inversion is constructed. The goal of minimum-structure inversion is to recover the model parameters that give the least spatial variation, *i.e.* the smoothest model, by minimizing an objective function that contains two terms with bound constraints (Li

and Oldenburg, 1996, 1998; Oldenburg and Li, 2004):

$$\Phi = \phi_d + \chi\phi_m \quad (2.17)$$

subject to

$$a \leq \rho \leq b \quad (2.18)$$

where the data misfit ϕ_d is a measure of how different the predicted data is from the observed data; the model objective function ϕ_m is a measure of some overall character of the model; χ is a trade-off parameter or regularization parameter; and a and b are the lower and upper bound on the density contrast.

The value of χ is greater than zero and determines the emphasis placed on the model objective function versus the data misfit. Smaller values result in a large model norm, small data misfit, and a detailed or over-fit model. Larger values result in a small model norm, large data misfit, and smooth or under-fit model (Oldenburg and Li, 2004).

2.4.2 Data misfit

The data misfit term is used to quantify the difference between the observed dataset and the dataset predicted by the resulting inversion model. The data misfit term is defined as (Oldenburg and Li, 2004; Lelièvre et al., 2010):

$$\phi_d = \sum_{i=1}^M \left(\frac{F[m]_i - d_i}{\sigma_i} \right)^2 \quad (2.19)$$

where d_i is the observed data, $F[m]_i$ is the candidate model where F denotes the forward modelling operator, and σ_i are the estimated uncertainties in the data arising from what is assumed to be random Gaussian noise. In this case, an acceptable misfit

is one that equals the number of data observations. If the data misfit is lower than the number of observations, it is assumed that the predicted gravity dataset is fitting the observed dataset too well and therefore fitting the error associated with the observed dataset.

2.4.3 Model objective function

Since the inversion problem is non-unique and multiple models are able to fit the observed data, a model objective function is necessary to limit the number of density models that satisfy the data misfit. The model objective function is defined as:

$$\begin{aligned}
 \phi_m = & \int_V w_s [w(z)(m - m_{ref})]^2 dv \\
 & + \int_V w_x \left[\frac{\partial(w(z)m)}{\partial x} \right]^2 dv \\
 & + \int_V w_y \left[\frac{\partial(w(z)m)}{\partial y} \right]^2 dv \\
 & + \int_V w_z \left[\frac{\partial(w(z)m)}{\partial z} \right]^2 dv
 \end{aligned} \tag{2.20}$$

The first term measures the difference between the recovered model m and the reference model m_{ref} and the last three terms measure the roughness of the model in the Cartesian axis directions (Li and Oldenburg, 1996; Lelièvre et al., 2010). This type of regularization recovers smooth physical property models since minimization of a roughness measure leads to smoothness. Spatially dependent weighting functions w_s , w_x , w_y , and w_z are used to weight the importance of one model parameter versus another. The function $w(z)$ is a depth or distance weighting function and is described further in Section 2.4.4.

2.4.4 Depth and distance weighting

Gravity data is a potential field that satisfies the Laplace equation when measurements are taken above the surface of the Earth (Section 2.1.2). As a consequence, the gravity data can be reproduced by many different density variations in the modelled Earth (Li and Oldenburg, 1996, 1998). The default solution is to concentrate the density near the surface, regardless of the true depth of the anomalous body. An equivalent solution would be much more mass required at depth to generate the same anomaly that a small amount of mass near the surface would generate; this occurs because the sensitivity of the gradiometer data decays with depth with distance from the source. A large mass at depth gives a larger value for the measure of model structure than less mass near the surface. As a result the minimum-structure inversion prefers the solution with less mass near the surface because both solutions reproduce the data to the same misfit level.

In airborne problems all the data is located above the surface and the common decay of the sensitivity is in the vertical direction. The lack of depth resolution can be overcome by introducing a depth or distance weighting: these types of weighting give cells at depth an equal probability of containing the anomalous density (Li and Oldenburg, 1996, 1998).

A depth weighting function takes into account only the distance below the observed geophysical data:

$$w(z) = \frac{1}{(z_j + z_0)^\beta} \quad (2.21)$$

where z_j is the depth to the j th cell below the surface, z_0 is the average survey height in the input coordinate system, and β is an adjustable parameter used to match the weighting function to the kernel's decay with depth. This form is a suitable first order approximation of the decay of the gravity field where there is a high density of data

observations and the topography is relatively flat.

A distance weighting function is preferred over a depth weighting function whenever geophysical data are irregularly distributed or there is a large range in topography. A distance weighting function is defined by the distance between cells and observation locations and accommodates both lateral and vertical variations in data sensitivity:

$$w(r) = \sqrt{\sum \left(\frac{1}{(r_{ij} + r_0)^\beta} \right)^2} \quad (2.22)$$

where r_{ij} is the distance between cell j and observation i and r_0 is some small stabilizing constant such as half the smallest cell dimension. As for depth weighting, β is chosen to match the weighting function to the kernel's decay with distance.

2.4.5 Preparing inversions

There are a number of steps required to prepare the data and mesh for an inversion (Li and Oldenburg, 1996, 1998):

- define the problem
- define the depth, width, and length of the modelling region
- define the data area
- generate tetrahedral mesh to match the resolution of the data, the desired resolution of the recovered model, and available computing power
- pad the mesh with a buffer of additional cells to prevent boundary effects where anomalies are located near the edge of the mesh
- calculate and remove the regional data trend that accounts for the contribution to the response of all sources located outside the modelling region

2.4.6 Geological constraints

Geological constraints are necessary to limit the number of mathematically-feasible models to those that are entirely consistent with existing geological knowledge (Fullagar and Pears, 2007; Williams, 2008). The program *vinv* is flexible enough to include a wide range of geological information, if available. The formulation provides for several global mathematical constraints that affect the whole model, including depth/distance weighting, together with located geological constraints that apply to individual cells in the form of an initial model. Model bounds can be supplied as either a global or located constraint. An initial model and bounds are used in every inversion but are assigned default values if not explicitly provided by the user. If located geological constraint information is available, it can be used to create detailed non-default initial models and assign density bounds. If any one of these is to be supplied, it must be defined for every cell in the model, but appropriate default values can be used in those cells that lack geological information.

2.4.6.1 Types of geological constraints

Surface samples, maps, core logs (Fullagar and Pears, 2007; Williams, 2008; Williams et al., 2009), cross sections, and volume interpretations can all be used as geological-constraints (Williams, 2008; Williams et al., 2009). These are included to confine the inversion to a geologically reasonable result. Surface samples and core samples may supply actual density measurements. Cross sections and volume interpretations represent 2D and 3D interpretations of subsurface geology from which density values can be estimated.

2.4.6.2 Implementing geological constraints

The initial model consists of a single density value in each cell; if an initial model is not specified a default value of 0 g/cm^3 is used (Williams, 2008; Williams et al., 2009). In a real Earth scenario, there may be several density measurements that lie inside the same inversion cell. By the principle of superposition, the observed gravity response associated with any density distribution inside a small cell will be the same as that observed if the cell contained a single density value equal to the arithmetic mean value (Blakely, 1996). The initial model density in each cell should therefore be the best estimate of the arithmetic mean density in that cell. In a synthetic data scenario, the initial model is chosen based on the true density values.

The bounds model indicates the minimum and maximum density allowed within each cell and provides a way to limit the range of density values within a region where the density is known to vary or is difficult to define exactly (Williams, 2008; Williams et al., 2009). Bounds can be applied with or without a non-default initial model. If an initial model is not supplied or when default values are used in a particular region, the bounds can be used as a global constraint to restrict the density in that region to some approximate limits based on known or expected geology. If an initial model is supplied, the bounds can be used as a local constraint to limit the range of density values. Since the initial density in each cell should be the best estimate of the mean density the bounds can act as a confidence interval on the estimate of the mean. For a real Earth scenario, the bounds should be the best estimate of the limits on the density range and not the maximum range of possible densities within the cell. In a synthetic data scenario, the bounds are chosen based on the true density.

Chapter 3

Synthetic data inversions:

Voisey's Bay deposits

3.1 Overview

A synthetic example based on the Voisey's Bay deposits demonstrates the benefits of including geological constraints in gravity gradient inversions. The inversions are performed using the forward modelling and minimum-structure inversion procedures discussed in Chapter 2. Inversion results are presented using four different initial models. The first is a default, geologically-unconstrained inversion using a zero-density initial model. The next three are all geologically-constrained inversions that differ in the amount of constraints included in the initial model. Varying the number of tensor components included in the inversion is also investigated. Inversion is performed using five different tensor component combinations: (i) U_{zz} ; (ii) U_{xx}, U_{xy}, U_{yy} ; (iii) U_{xz}, U_{yz}, U_{zz} ; (iv) $U_{xx}, U_{xy}, U_{xz}, U_{yy}, U_{yz}$; and (v) $U_{xx}, U_{xy}, U_{xz}, U_{yy}, U_{yz}, U_{zz}$. Data difference plots and predicted data plots are shown only for the six component inversion case due to the redundancy of the plots. All inversions presented show an acceptable data

misfit and reproduce the observed gravity gradient data.

3.2 Creating the density model

The density model was constructed from the geological Datamine model of the Voisey's Bay deposits. The geological contact surfaces were constructed by joining together the relevant downhole contacts. Vertical cross sections were created every 50–100 m from the geological Datamine model (Figure 3.1). The cross sections were loaded into FacetModeller to give a sequence of horizontally stacked 2D outlines of the massive sulphide, disseminated sulphide and troctolite surfaces. These outlines were then joined together between sections using nodes and triangular facets to create the contact surfaces (Figure 3.2). For simplicity, any disseminated sulphide surfaces were taken to be massive sulphide.

The topography surface was generated from point data extracted from Datamine. Triangle was used to create a triangular mesh to connect the points. The original topography data consisted of 33018 points; this was reduced to a more manageable 4088 points. The topography surface was saved as a poly file and imported into FacetModeller. FacetModeller is able to merge two poly files into one and scan and remove duplicate nodes. Any intersecting facets between the troctolite and topography surfaces were identified and fixed: the *-d* flag in Tetgen identifies any intersecting facets and produces list of the intersections. Any intersections were fixed manually using FacetModeller.

The final model contains several sulphide units hosted within a troctolite unit (Figure 3.3). The remaining rock is gneiss. The sulphides and troctolite have density contrasts of 1.65 g/cm^3 and 0.09 g/cm^3 respectively, relative to the background gneiss. The troctolite unit strikes west-northwest in the southern and central regions of the

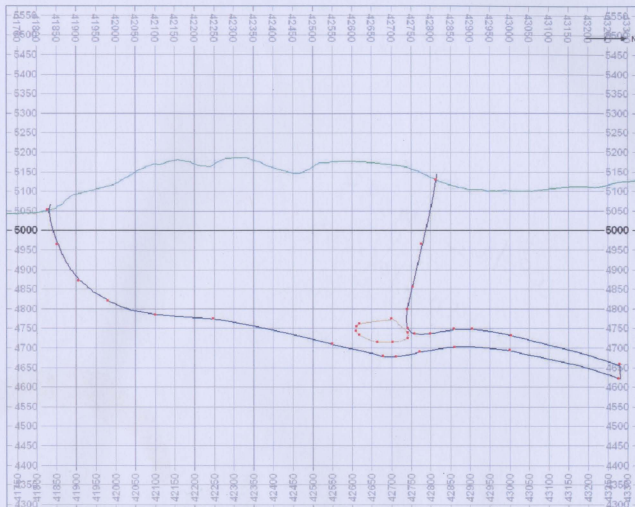


Figure 3.1: Vertical north-south cross section through the Eastern Deeps deposit at 56580 m Easting. The cross section was created from the geological Datamine model and loaded into FacetModeller. The green, blue, and yellow lines show the interfaces from Datamine. The green line marks the topography surface; the blue line marks the boundary between the gneiss and troctolite; and the yellow line marks the boundary between the troctolite and sulphide. The red nodes are used to create facets.

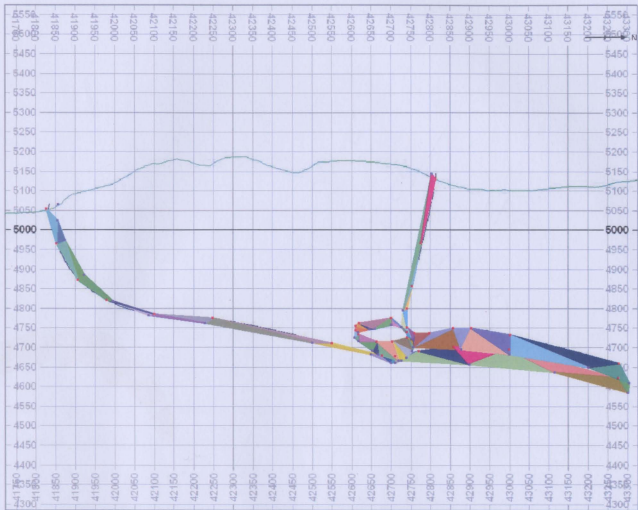


Figure 3.2: Triangular facets are used to join the nodes together. The purple nodes are on the 56630 m cross section and the red nodes are on the 56580 m cross section.

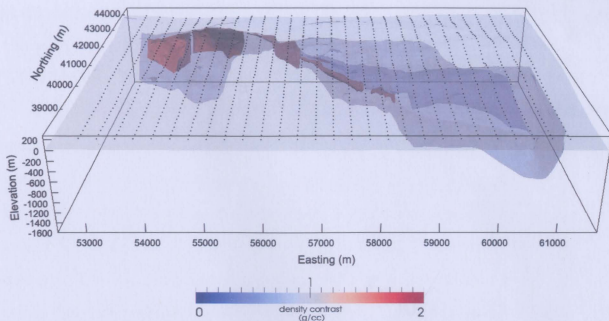


Figure 3.3: Perspective view looking down to the north of the PPC for a 3D model based on the Voisey's Bay deposit. The sulphide surface is shown in red and the troctolite surface is shown in transparent blue. The topography surface is transparent grey and the boundary of the modelling region is shown by black lines. The modelling region is 9200 m by 6500 m by 1880 m (easting by northing by depth) and the topography has an elevation range of 280 m. The observation points are indicated by the black dots and are located at an elevation of 80 m above the topography along 28 north-south lines spaced 300 m apart with station intervals of 150 m.

survey area and strikes west in the northwest region of the survey area. The sulphide deposits occur in the northwest region of the survey area. The sulphide deposits from west to east are: Reid Brook zone, Discovery Hill, Mini-Ovoid, Ovoid, Extension zone, and Eastern Deeps. The Eastern Deeps zone consists of one elongate deposit and two smaller disc like deposits.

3.3 Synthetic airborne gravity gradiometer data

The gravity gradient data is modelled at an elevation of 80 m above the topography surface along 28 north-south lines spaced 300 m apart with a station interval of 150 m

to simulate an airborne survey (Figure 3.4). The data were contaminated with random Gaussian noise with a standard deviation of 2% of the datum and a 2% noise floor before inverting (Figure 3.5).

As discussed in Section 2.1.2.3, the different tensor components give different information on the geological attributes of the subsurface (Figure 3.4). The U_{zz} component has the clearest correspondence with the geology and contains a positive anomaly over the sulphide deposits and troctolite unit. The troctolite edges are well defined and large positive anomalies occur over the Discovery Hill, Ovoid, and Extension Zone deposits. The U_{xx} component outlines the northern and southern edges of the troctolite. Negative anomalies occur over the sulphide deposits and troctolite unit. The U_{yy} component outlines the eastern and western edges of the troctolite. A large positive to negative anomaly dominates the response over the Extension zone outlining the Extension zone and troctolite/gneiss boundary. The U_{xy} component is also dominated by an anomaly over the Extension zone. The U_{xz} component changes sign along the north-south centre of mass of the troctolite. The edges of the troctolite are also outlined by a negative anomaly over the northern edges and a positive anomaly over the southern edges. The U_{yz} component changes sign along the east-west centre of mass of the troctolite. The edges of the troctolite are also outlined by a negative anomaly over the eastern edges and a positive anomaly over the western edges. Overall, the features observed in the calculated gradiometer data are preserved in the noise contaminated gradiometer data (Figure 3.5).

3.4 Geologically-unconstrained inversion

Geologically-unconstrained gravity gradient inversions were performed using a zero-density initial model. The same mesh was used for all inversions; a quality mesh

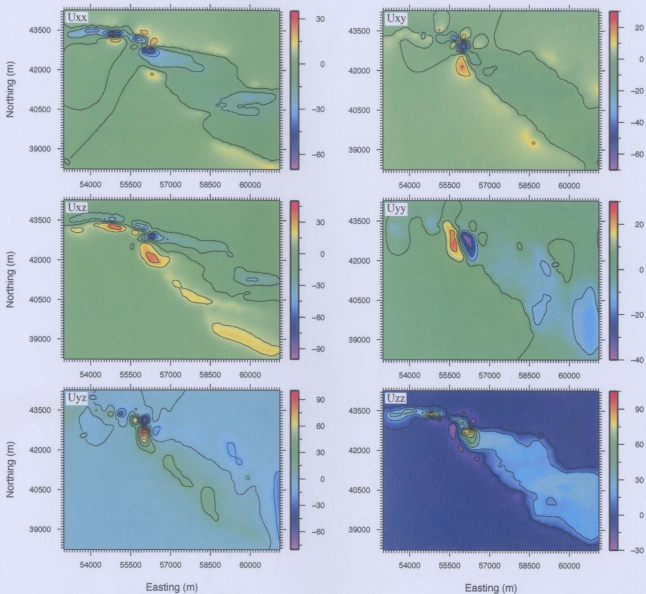


Figure 3.4: The calculated gradiometer data observed above the Voisey's Bay deposit shown in Figure 3.3. Units are in Eotvos. Contour interval is 15 E for U_{xx} , U_{xz} , U_{yz} , and U_{zz} and 10 E for U_{xy} and U_{yy} .

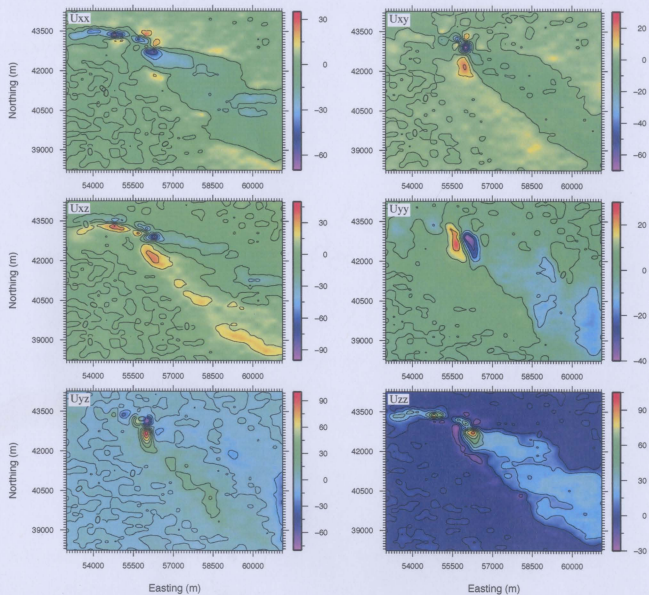


Figure 3.5: The noise contaminated gradiometer data observed above the Voisey's Bay deposit used for inversion. Units are in Eotvos. Contour interval is 15 E for U_{xx} , U_{xz} , U_{yz} , and U_{zz} and 10 E for U_{xy} and U_{yy} .

was generated using a minimum radius-edge ratio of $q = 1.414$ and a maximum tetrahedron volume of $a = 1,000,000 \text{ m}^3$ giving a total of 254,670 cells. The density bounds were applied as a global constraint to the entire mesh and constrained to a lower bound of 0 g/cm^3 and an upper bound of 5 g/cm^3 . These bounds were selected to allow for an unrestricted recovery of a positive density contrast while maintaining a plausible density range. A distance weighting was used with $\beta = 2$ and $r_0 = 1$ (Equation 2.22).

3.4.1 U_{zz} inversion

The single-component inversion serves as a base model to compare whether the addition of more components increases the quality of the resulting model (Martinez and Li, 2011). A series of preliminary inversions using a coarse mesh and a range of *chifact* values were carried out in order to select the optimal regularization parameter using a plot of data misfit versus the model objective function (Appendix C.2). The ideal *chifact* will reproduce a data misfit value ϕ_d that equals the total number of data points within a 5% error margin. A *chifact* value of one was found to provide the optimal trade-off between model structure and data misfit; it is used for all the inversions in this chapter.

The predicted data and difference data maps are omitted for brevity (see Figure 3.10 and Figure 3.11 for an example of predicted data and difference data maps). The predicted data resembles the data in Figure 3.4 and the difference between the observed and predicted data is suitably random. The range of values seen between the observed and predicted data are an indication of the noise in the data which the recovered model does not fit. The standard deviation of the data difference is used to determine the estimated noise level (Martinez et al., 2010; Martinez and Li, 2011). The standard deviation calculated from the data difference map is 2.91 E (Table 3.1).

The density contrast model was created using 1148 data points and the data misfit is 1105.60, well within the 5% error margin .

Table 3.1: Standard deviation of the data difference (E) for the geologically-unconstrained inversion results.

Inversion	U_{xx}	U_{xy}	U_{xz}	U_{yy}	U_{yz}	U_{zz}
U_{zz}	-	-	-	-	-	2.91
U_{xx}, U_{xy}, U_{yy}	2.33	2.04	-	1.04	-	-
U_{xz}, U_{yz}, U_{zz}	-	-	2.82	-	3.79	2.40
$U_{xx}, U_{xy}, U_{xz}, U_{yy}, U_{yz}$	2.27	1.92	2.84	1.09	3.59	-
$U_{xx}, U_{xy}, U_{xz}, U_{yy}, U_{yz}, U_{zz}$	2.02	1.79	2.69	1.19	3.33	2.64

The recovered density contrast ranges from 0–0.339 g/cm³ (Table 3.1), well below the true maximum anomalous density. A perspective view of the recovered density contrast model is shown in Figure 3.6. All cells below 0.0855 g/cm³ are removed to highlight the recovered troctolite unit (Figure 3.6a) and all cells below 0.20 g/cm³ are removed to highlight the recovered sulphide deposits (Figure 3.6b). Two low density contrast features are observed along with several spurious features located along the boundary of the modelling region (Figure 3.6a). The surface edge of the troctolite pluton is recovered in the east and the near surface feeder dyke is recovered in the west. The deeper feeder dyke system located north of the eastern body is not detected. Two high density contrast bodies are recovered (Figure 3.6b). The larger body is associated with the Extension zone deposit and the smaller is associated with the Discovery Hill deposit. The results are poor as neither recovered body is representative of the shape, size, or density of the true sulphide deposits.

3.4.2 U_{xx}, U_{xy}, U_{yy} inversion

The first three-component inversion makes use of the horizontal gradients of the horizontal components of gravity following the example of Zhdanov et al. (2004) and Li

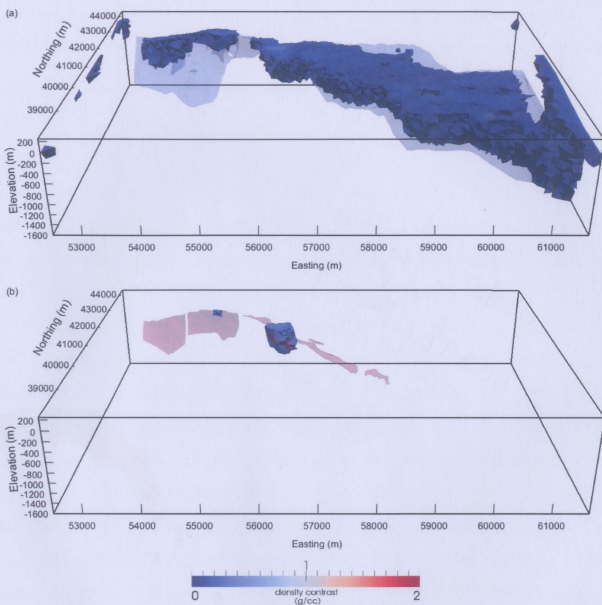


Figure 3.6: A perspective view of the recovered model for the unconstrained inversion result using the U_{zz} component. (a) All cells less than 0.0855 g/cm^3 have been removed to highlight the recovered troctolite unit; the true troctolite model is shown by the transparent blue overlay. (b) All cells less than 0.20 g/cm^3 have been removed to highlight the recovered sulphide deposits; the true sulphide model is shown by the transparent red overlay.

Table 3.2: Maximum density contrast for the geologically-unconstrained inversion results.

Inversion	$\Delta\rho_{max}$ (g/cm ³)
U_{zz}	0.339
U_{xx}, U_{xy}, U_{yy}	0.511
U_{xz}, U_{yz}, U_{zz}	0.478
$U_{xx}, U_{xy}, U_{xz}, U_{yy}, U_{yz}$	0.614
$U_{xx}, U_{xy}, U_{xz}, U_{yy}, U_{yz}, U_{zz}$	0.755

(2010). Zhdanov et al. (2004) and Li (2010) used $U_{uv} = (U_{xx} - U_{yy})/2$ rather than using the U_{xx} and U_{yy} components separately. Table 3.1 lists the standard deviation of the data difference. The density contrast model was created using 3444 data points and the data misfit is 3311.70, well within the 5% error margin.

The recovered density contrast ranges from 0–0.511 g/cm³, an improvement over the U_{zz} inversion (Table 3.2). A perspective view of the recovered model is shown in Figure 3.7. Two low density contrast features are observed along with several spurious features located along the boundary of the modelling region (Figure 3.7a). The surface edge of the troctolite pluton is recovered in the east and the near surface feeder dyke is recovered in the west. The deeper feeder dyke system located north of the eastern body is not detected. Three dense bodies are recovered (Figure 3.7b). The recovered bodies are associated with the Discovery Hill, the Ovoid, and the Extension zone deposits (west to east). Similar to the U_{zz} inversion, the recovered bodies are not representative of the shape, size, or density of the true sulphide deposits.

3.4.3 U_{xz}, U_{yz}, U_{zz} inversion

The second three-component inversion makes use of the horizontal and vertical gradients of the vertical component of gravity following the example of Martinez et al. (2010). Table 3.1 lists the standard deviation of the data difference. The density

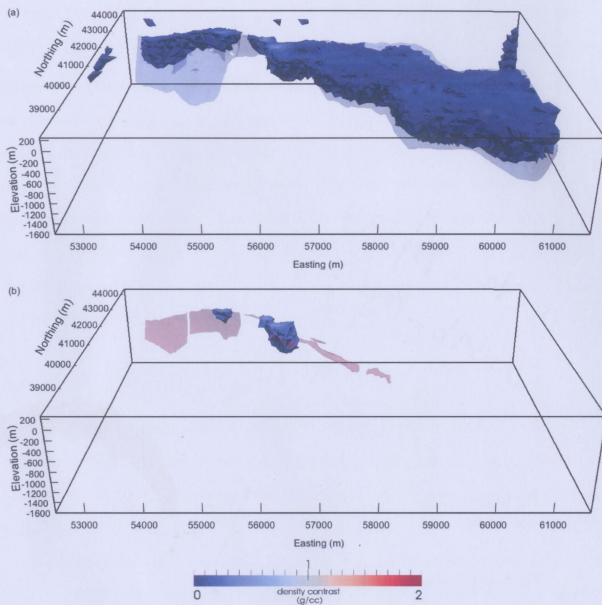


Figure 3.7: A perspective view of the recovered model for the unconstrained inversion result using the U_{xx} , U_{xy} , and U_{yy} components. (a) All cells less than 0.0855 g/cm^3 have been removed to highlight the recovered troctolite unit; the true troctolite model is shown by the transparent blue overlay. (b) All cells less than 0.20 g/cm^3 have been removed to highlight the recovered sulphide deposits; the true sulphide model is shown by the transparent red overlay.

contrast model was created using 3444 data points and the data misfit is 3274.53, well within the 5% error margin.

The recovered density contrast ranges from 0–0.478 g/cm³, an improvement over the U_{zz} result (Table 3.2). A perspective view of the recovered model is shown in Figure 3.8. Two low density contrast features are observed along with several spurious features located along the boundary of the modelling region (Figure 3.8a). The surface edge of the troctolite pluton is recovered in the east and the near surface feeder dyke is recovered in the west. The deeper feeder dyke system located north of the eastern body is not detected. Three dense bodies are recovered (Figure 3.8b). From west to east, the recovered bodies are associated with the Discovery Hill, the Ovoid, and the Extension Zone deposits. Similar to the two previous inversions, the recovered bodies are not representative of the shape, size, or density of the true sulphide deposits.

3.4.4 U_{xx} , U_{xy} , U_{xz} , U_{yy} , U_{yz} inversion

This inversion makes use of five independent tensor components following the example of Li (2001). Table 3.1 lists the standard deviation of the data difference. The density contrast model was created using 5740 data points and the data misfit is 5657.00, well within the 5% error margin.

The recovered density contrast is 0–0.614 g/cm³, an improvement over all previous inversion results (Table 3.2). A perspective view of the recovered model is shown in Figure 3.9. Two low density contrast features are observed along with several small spurious features located along the boundary of the modelling region (Figure 3.9a). The surface edge of the troctolite pluton is recovered in the east and the near surface feeder dyke is recovered in the west. The deeper feeder dyke system located north of the eastern body is not detected. Three dense bodies are recovered (Figure 3.9b). The recovered bodies are associated with the Discovery Hill, the Ovoid, and the Extension

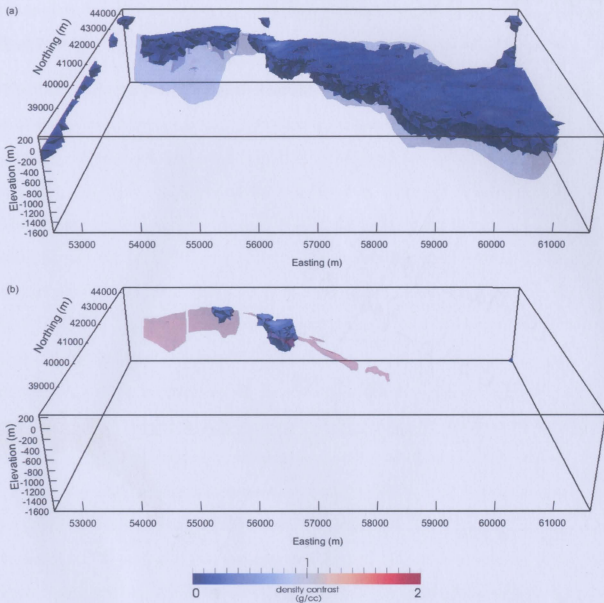


Figure 3.8: A perspective view of the recovered model for the unconstrained inversion result using the U_{xz} , U_{yz} , and U_{zz} components. (a) All cells less than 0.0855 g/cm^3 have been removed to highlight the recovered troctolite unit; the true troctolite model is shown by the transparent blue overlay. (b) All cells less than 0.20 g/cm^3 have been removed to highlight the recovered sulphide deposits; the true sulphide model is shown by the transparent red overlay.

zone deposits (west to east). Similar to the previous inversions, the recovered bodies are not representative of the shape, size, or density of the true sulphide deposits.

3.4.5 U_{xx} , U_{xy} , U_{xz} , U_{yy} , U_{yz} , U_{zz} inversion

The final geologically-unconstrained inversion uses the full tensor gradient. Figure 3.10 shows the predicted gradiometer data and Figure 3.11 shows the data difference between the observed and predicted data. The predicted data resembles the data in Figure 3.4. The standard deviation of the data difference is listed in Table 3.1. The density contrast model was created using 6888 data points and the data misfit is 6603.99, well within the 5% error margin. The largest difference between the observed and predicted data coincides with the location of the largest signal in the data, *i.e.* over the Ovoid and Extension zone deposits. Away from the largest signal in the data, the data difference is suitably random. This is expected because the minimum-structure inversion produces as simple a model as possible. In a minimum-structure inversion, the low signal background data are slightly over-fit whereas the high signal data are slightly under-fit resulting in a reasonable overall measure of misfit.

The recovered density contrast ranges from 0–0.755 g/cm³, an improvement over all previous inversion results (Table 3.2). A perspective view of the recovered model is shown in Figure 3.12. Two low density contrast features are observed along with several small spurious features located along the boundary of the modelling region (Figure 3.12a). The surface edge of the troctolite pluton is recovered in the east and the near surface feeder dyke is recovered in the west. The distance between the two troctolite bodies is also minimized compared to previous results. The deeper feeder dyke system located north of the eastern body is not detected. Five dense bodies are recovered (Figure 3.12b). The recovered bodies are associated with the Reid Brook zone, Discovery Hill, the Ovoid, and the Extension zone deposits (west to

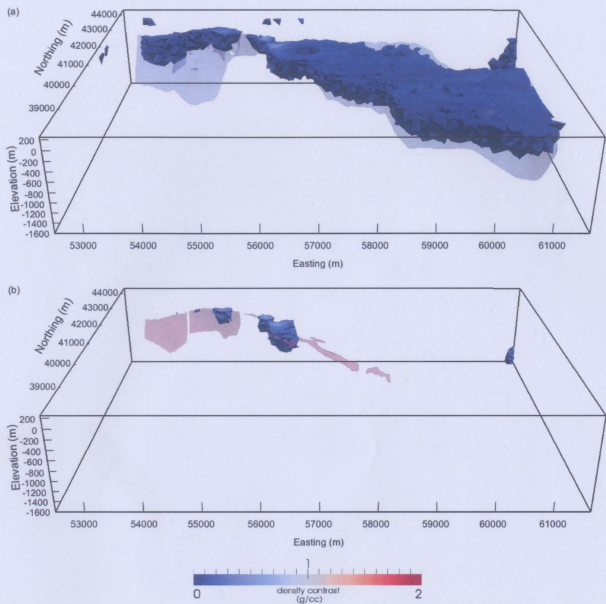


Figure 3.9: A perspective view of the recovered model for the unconstrained inversion result using the U_{xx} , U_{xy} , U_{xz} , U_{yy} , and U_{yz} components. (a) All cells less than 0.0855 g/cm^3 have been removed to highlight the recovered troctolite unit; the true troctolite model is shown by the transparent blue overlay. (b) All cells less than 0.20 g/cm^3 have been removed to highlight the recovered sulphide deposits; the true sulphide model is shown by the transparent red overlay.

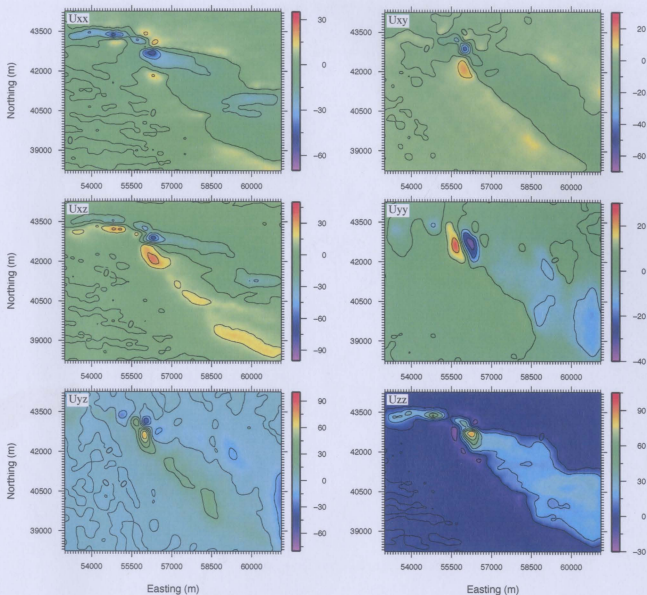


Figure 3.10: The predicted gradiometer data for the geologically-unconstrained inversion using six tensor components. Units are in Eotvos. Contour interval is 15 E for U_{xx} , U_{xz} , U_{yz} , and U_{zz} and 10 E for U_{xy} and U_{yy} .

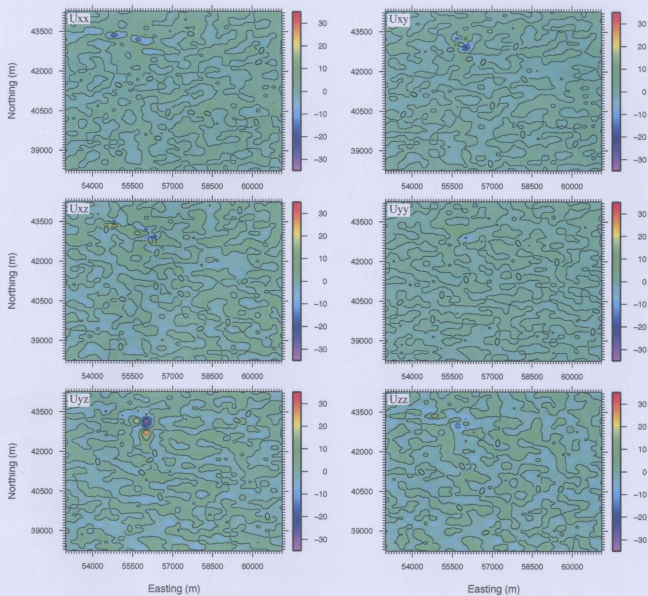


Figure 3.11: The data difference between the observed and predicted data for the geologically-unconstrained inversion using six tensor components. Units are in Eotvos. Contour interval is 10 E.

east). Similar to the previous inversions, the recovered bodies are not representative of the shape, size, or density of the true sulphide deposits.

3.5 Geologically-constrained inversion: drill holes

The first geologically-constrained inversion uses the same mesh as the geologically-unconstrained inversion. Instead of a zero-density initial model, a small amount of density information is added from three vertical drill holes. Drill hole A is located at (54930, 43380, 175), drill hole B is located at (55880, 43150, 70), and drill hole C is located at (56130, 42750, 75) (Figure 3.13a). The drill hole locations were selected based on anomalies in the gravity gradient data (Figure 3.4 and 3.5). The cells intersected by the drill holes were assigned the true density values of 0 g/cm^3 if gneiss was intersected, 0.09 g/cm^3 if troctolite was intersected, and 1.65 g/cm^3 if sulphide was intersected. A default value of 0 g/cm^3 was assigned where no information was available. In total, only 19 cells were assigned non-default density values. The density bounds were applied on a cell by cell basis. Cells with a density value of 0 g/cm^3 were assigned a lower bound of 0 g/cm^3 and an upper bound of 1.7325 g/cm^3 ; cells with a density value of 0.09 g/cm^3 were assigned a lower bound of 0.0855 g/cm^3 and an upper bound of 0.0945 g/cm^3 ; and cells with a density value of 1.65 g/cm^3 were assigned a lower bound of 1.5675 g/cm^3 and an upper bound of 1.7325 g/cm^3 . The bounds for the troctolite unit and sulphide deposits are $\pm 10\%$ the true density value. A distance weighting was used with $\beta = 2$ and $r_0 = 1$ (Equation 2.22).

3.5.1 U_{zz} inversion

The recovered density contrast ranges from 0 – 1.57 g/cm^3 , an improvement over the geologically-unconstrained results (Table 3.2 and 3.3). The standard deviation is

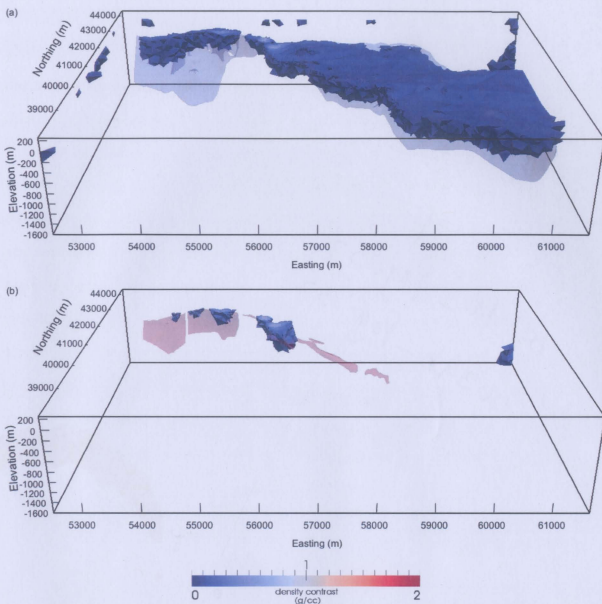


Figure 3.12: A perspective view of the recovered model for the unconstrained inversion result using all six tensor components. (a) All cells less than 0.0855 g/cm^3 have been removed to highlight the recovered troctolite unit; the true troctolite model is shown by the transparent blue overlay. (b) All cells less than 0.20 g/cm^3 have been removed to highlight the recovered sulphide deposits; the true sulphide model is shown by the transparent red overlay.

listed in Table 3.4. The data misfit is 1159.79, well within the 5% error margin. Figure 3.13 shows a perspective view of the recovered density contrast model. One low density contrast feature is observed along with several spurious features located along the boundary of the modelling region (Figure 3.13a). There are more spurious features than previously observed in the geologically-unconstrained results (Figure 3.6a), particularly along the western edge. The surface edge of the troctolite pluton is recovered in the east and the near surface feeder dyke is recovered in the west. The deeper feeder dyke system located north of the pluton is not detected. Three high density contrast features are recovered (Figure 3.13b). As expected, the dense bodies are associated with the drill holes through the Discovery Hill, Ovoid, and Extension zone deposits (west to east). The results are an improvement over the geologically-unconstrained inversion result (Figure 3.6b) because the maximum density is close to the true density. However, the results are still not representative of the shape or size of the true sulphide deposits and overall the recovered deposits are larger and less dense than the true deposits.

Table 3.3: Maximum density contrast for the inversion constrained using drill hole data.

Inversion	$\Delta\rho_{max}$ (g/cm ³)
U_{zz}	1.57
U_{xx}, U_{xy}, U_{yy}	1.57
U_{xz}, U_{yz}, U_{zx}	1.57
$U_{xx}, U_{xy}, U_{xz}, U_{yy}, U_{yz}$	1.57
$U_{xx}, U_{xy}, U_{xz}, U_{yy}, U_{yz}, U_{zx}$	1.57

3.5.2 U_{xx}, U_{xy}, U_{yy} inversion

The recovered density contrast ranges from 0–1.57 g/cm³; an improvement over the geologically-unconstrained inversion and the same range as the U_{zz} inversion (Table

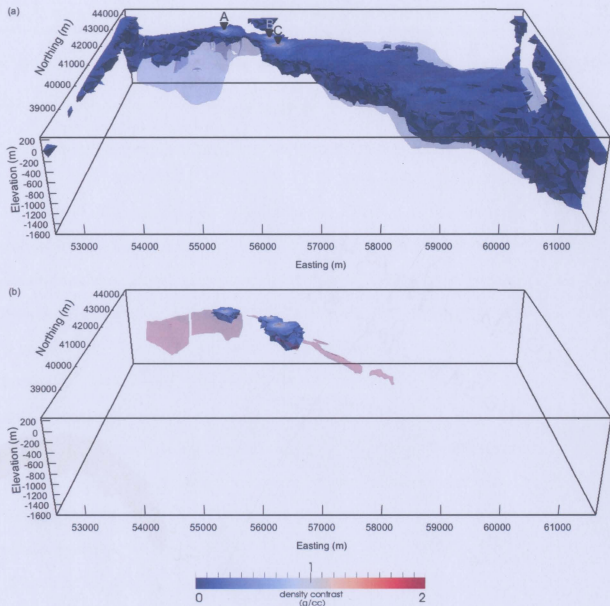


Figure 3.13: A perspective view of the recovered model using the U_{zz} component and density information from three drill holes. (a) All cells less than 0.0855 g/cm^3 have been removed to highlight the recovered troctolite unit; the true troctolite model is shown by the transparent blue overlay. The black triangles point to the drill hole locations: drill hole A is located at (54930, 43380, 175), drill hole B is located at (55880, 43150, 70), and drill hole C is located at (56130, 42750, 75). (b) All cells less than 0.20 g/cm^3 have been removed to highlight the recovered sulphide deposits; the true sulphide model is shown by the transparent red overlay.

Table 3.4: Standard deviation of the data difference (E) for the inversion constrained using drill hole data.

Inversion	U_{xx}	U_{xy}	U_{xz}	U_{yy}	U_{yz}	U_{zz}
U_{zz}	-	-	-	-	-	2.64
U_{xx}, U_{xy}, U_{yy}	2.28	1.91	-	1.15	-	-
U_{xz}, U_{yz}, U_{zz}	-	-	2.83	-	3.52	2.62
$U_{xx}, U_{xy}, U_{xz}, U_{yy}, U_{yz}$	2.24	1.85	2.89	1.16	3.45	-
$U_{xx}, U_{xy}, U_{xz}, U_{yy}, U_{yz}, U_{zz}$	2.09	1.79	2.78	1.25	3.34	2.79

3.2 and 3.3). The standard deviation is listed in Table 3.4. The data misfit is 3606.24, well within the 5% error margin. Figure 3.14 shows a perspective view of the recovered density contrast model. One low density contrast feature is observed along with several minor spurious features located along the boundary of the modelling region (Figure 3.14a). There are less spurious features than previously observed in the U_{zz} inversion (Figure 3.13a). The surface edge of the troctolite pluton is recovered in the east and the near surface feeder dyke is recovered in the west. The deeper feeder dyke system located north of the pluton is not detected. Three dense bodies are recovered (Figure 3.14b). As expected, the dense bodies are associated with the drill holes through the Discovery Hill, Ovoid, and Extension zone deposits (west to east). The results represent an improvement over the geologically-unconstrained inversion result (Figure 3.7b), but the results are still not representative of the shape or size of the true sulphide deposits.

3.5.3 U_{xz}, U_{yz}, U_{zz} inversion

The recovered density contrast ranges from 0–1.57 g/cm³; an improvement over the geologically-unconstrained inversion and the same range as the previous two inversions (Table 3.2 and 3.3). The standard deviation is listed in Table 3.4. The data misfit is 3565.65, well within the 5% error margin. A perspective view of the recovered density

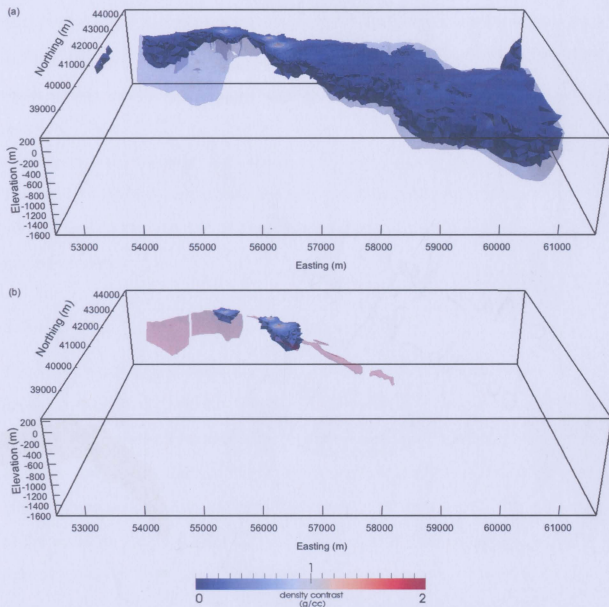


Figure 3.14: A perspective view of the recovered model using the U_{xx} , U_{xy} , and U_{yy} components and density information from three drill holes. Figure 3.13a shows the drill hole locations. (a) All cells less than 0.0855 g/cm^3 have been removed to highlight the recovered troctolite unit; the true troctolite model is shown by the transparent blue overlay. (b) All cells less than 0.20 g/cm^3 have been removed to highlight the recovered sulphide deposits; the true sulphide model is shown by the transparent red overlay.

contrast model is shown in Figure 3.15. One low density contrast feature is observed along with several minor spurious features located along the boundary of the modelling region (Figure 3.15a). The surface edge of the troctolite pluton is recovered in the east and the near surface troctolite feeder dyke is recovered in the west. The deeper feeder system located north of the pluton is not detected. Three dense bodies are recovered (Figure 3.15b). As expected, the dense bodies are associated with the drill holes through the Discovery Hill, Ovoid, and Extension zone deposits (west to east). The results represent an improvement over the geologically-unconstrained inversion result (Figure 3.8b), but are still not representative of the shape or size of the true sulphide deposits.

3.5.4 U_{xx} , U_{xy} , U_{xz} , U_{yy} , U_{yz} inversion

The recovered density contrast ranges from 0–1.57 g/cm³ (Table 3.3). The standard deviation is listed in Table 3.4. The data misfit is 5956.72, well within the 5% error margin. A perspective view of the recovered density contrast model is shown in Figure 3.16. One low density contrast feature is observed along with minor spurious features located along the boundary of the modelling region (Figure 3.16a). The surface edge of the troctolite pluton is recovered in the east and the near surface troctolite feeder dyke is recovered in the west. The deeper feeder system located north of the pluton is not detected. Four dense bodies are recovered (Figure 3.16b). As expected, the dense bodies are associated with the drill holes through the Discovery Hill, Ovoid, and Extension zone deposits (west to east). The results represent an improvement over the previous results, both geologically-unconstrained and constrained, but still do not represent the shape or size of the true sulphide deposits.

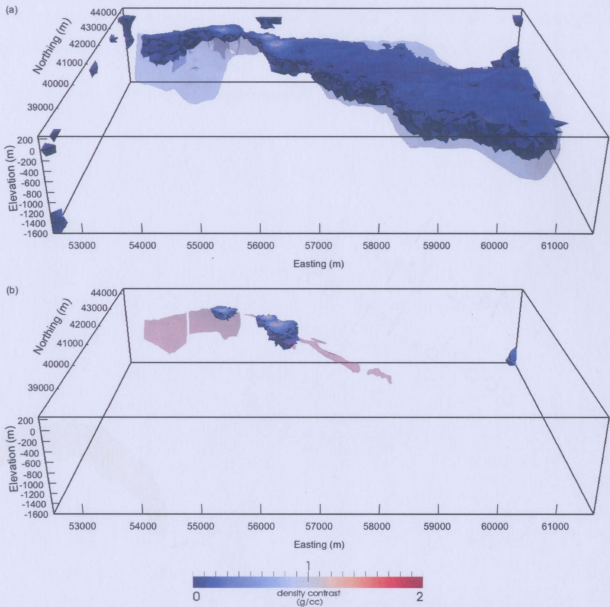


Figure 3.15: A perspective view of the recovered model using the U_{xz} , U_{yz} , and U_{zz} components and density information from three drill holes. Figure 3.13a shows the drill hole locations. (a) All cells less than 0.0855 g/cm^3 have been removed to highlight the recovered troctolite unit; the true troctolite model is shown by the transparent blue overlay. (b) All cells less than 0.20 g/cm^3 have been removed to highlight the recovered sulphide deposits; the true sulphide model is shown by the transparent red overlay.

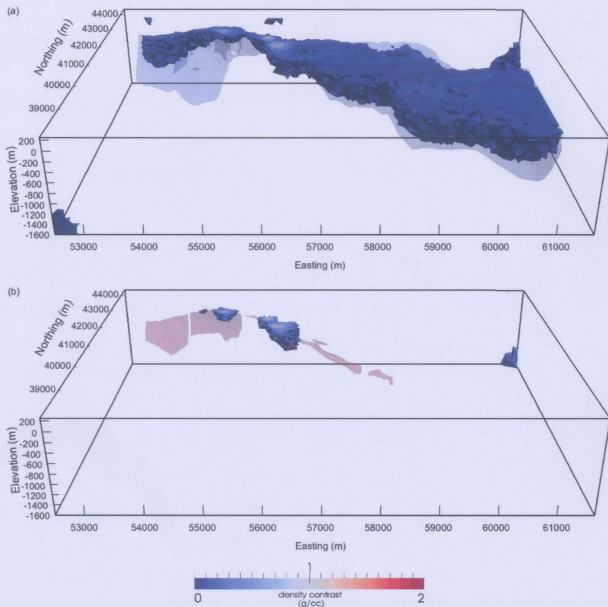


Figure 3.16: A perspective view of the recovered model using the U_{xx} , U_{xy} , U_{xz} , U_{yy} , and U_{yz} components and density information from three drill holes. Figure 3.13a shows the drill hole locations. (a) All cells less than 0.0855 g/cm^3 have been removed to highlight the recovered troctolite unit; the true troctolite model is shown by the transparent blue overlay. (b) All cells less than 0.20 g/cm^3 have been removed to highlight the recovered sulphide deposits; the true sulphide model is shown by the transparent red overlay.

3.5.5 U_{xx} , U_{xy} , U_{xz} , U_{yy} , U_{yz} , U_{zz} inversion

Figure 3.17 shows the predicted gradiometer data and Figure 3.18 shows the data difference between the observed and predicted data. The standard deviation is listed in Table 3.4. The data misfit is 7175.80, well within the 5% error margin. The largest difference between the observed and predicted data coincides with the location of the largest signal in the data. Elsewhere, the data difference is suitably random. This is expected and was previously mentioned in Section 3.4.5.

The recovered density contrast ranges from 0–1.57 g/cm³ (Table 3.3). A perspective view of the recovered density contrast model is shown in Figure 3.19. One low density contrast feature is observed along with several minor spurious features located along the boundary of the modelling region (Figure 3.19a). The surface edge of the troctolite pluton is recovered in the east and the near surface troctolite feeder dyke is recovered in the west. The deeper feeder system located north of the pluton is not detected. Five dense bodies are recovered (Figure 3.19b). The three largest dense bodies are associated with the drill holes through the Discovery Hill, Ovoid, and Extension zone deposits (west to east). The two smaller dense bodies are associated with the Reid Brook deposit and the western edge of the Discovery Hill deposit. The results represent an improvement over the previous results, both geologically-unconstrained and constrained, but still do not represent the shape or size of the true sulphide deposits.

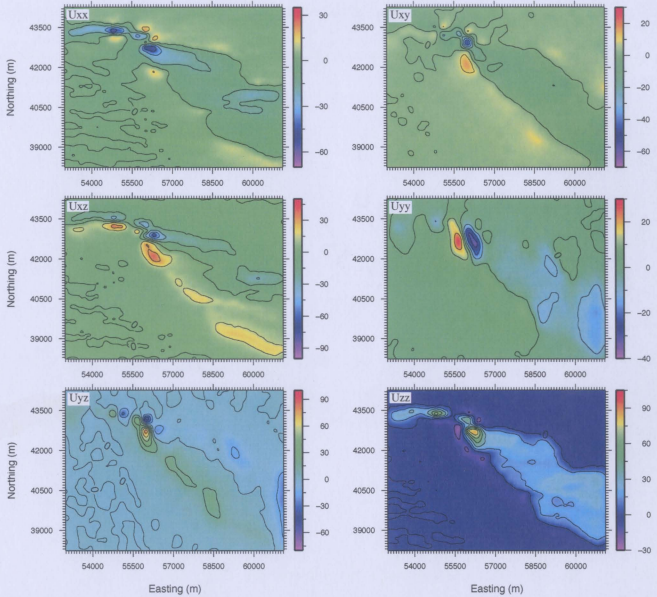


Figure 3.17: The predicted gradiometer data for the six tensor component inversion using density information from three drill holes as the initial model. Units are in Eotvos. Contour interval is 15 E for U_{xx} , U_{xz} , U_{yz} , and U_{zz} and 10 E for U_{xy} and U_{yy} .

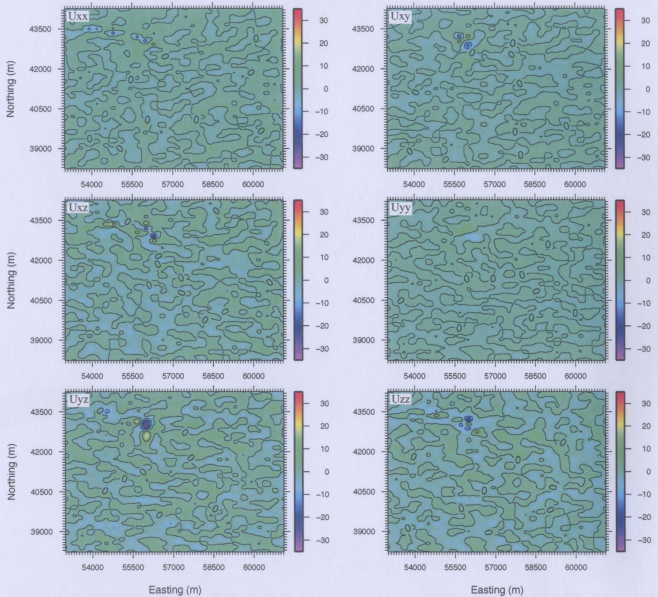


Figure 3.18: The data difference between the observed and predicted data for the six component inversion using density information from three drill holes as the initial model. Units are in Eotvos. Contour interval is 10 E.

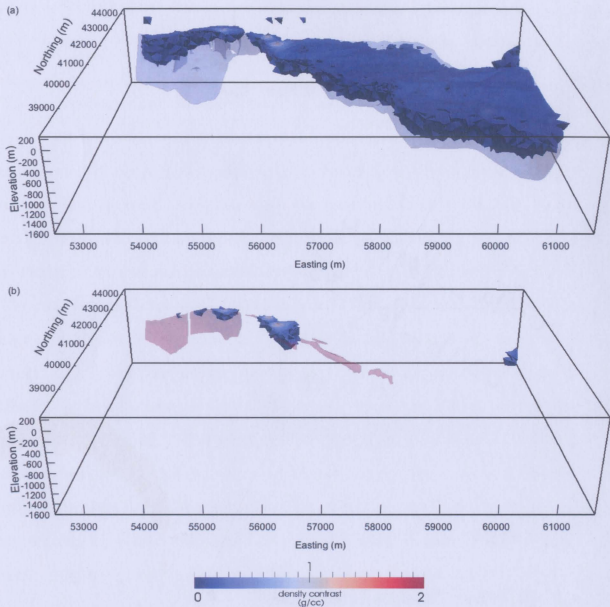


Figure 3.19: A perspective view of the recovered model using all six tensor components and density information from three drill holes. Figure 3.13a shows the drill hole locations. (a) All cells less than 0.0855 g/cm^3 have been removed to highlight the recovered troctolite unit; the true troctolite model is shown by the transparent blue overlay. (b) All cells less than 0.20 g/cm^3 have been removed to highlight the recovered sulphide deposits; the true sulphide model is shown by the transparent red overlay.

3.6 Geologically-constrained inversion: troctolite surface

3.6.1 Constrained example A

The next geologically-constrained example assumes that a volume model of the troctolite unit has been created from surface mapping and drilling. Unlike the initial models used in the previous inversions, this model incorporates the troctolite surface directly into the mesh. A quality mesh was generated using a minimum radius-edge ratio of $q = 5$ and a maximum tetrahedron volume of $a = 2,000,000,000 \text{ m}^3$ applied to the troctolite unit and no maximum tetrahedron volume applied to the gneiss unit. The resulting mesh consists of 245,632 cells; 103,616 cells are designated troctolite and 142,016 cells are designated gneiss. The initial density for both the troctolite and gneiss units is the true density contrast, *i.e.* 0.09 g/cm^3 and 0 g/cm^3 , respectively. The troctolite is allowed to vary between a lower bound of 0.0855 g/cm^3 and an upper bound of 1.7325 g/cm^3 . The upper bound allows for any high density material to be incorporated into the solution (*i.e.* sulphide deposits). The gneiss is allowed to vary between a lower bound of 0 g/cm^3 and an upper bound of 0.0045 g/cm^3 . A major assumption is that any sulphide deposits are entirely located within the troctolite unit. A distance weighting was used with $\beta = 2$ and $r_0 = 1$ (Equation 2.22).

3.6.2 U_{zz} inversion

The recovered density contrast ranges from $0\text{--}1.62 \text{ g/cm}^3$ (Table 3.5). The standard deviation of the data is listed in Table 3.6. The data misfit is 1168.77, well within the 5% error margin. A perspective view of the recovered density contrast is shown in Figure 3.20. Several improvements are observed in the recovered model. The spurious

features observed in previous inversion results are no longer present and the troctolite surface is accurately reproduced (Figure 3.20a); this is expected as the troctolite surface was used directly in the initial model and the gneiss bounds did not overlap with the troctolite bounds. Several high density bodies are recovered associated with the Reid Brook, Discovery Hill, Ovoid, Extension zone, and Eastern Deeps deposits (Figure 3.20b). Both the Reid Brook and Eastern Deeps deposits went undetected in previous inversion results. The recovered Ovoid and Extension Zone deposits are smaller and denser than in previous inversion results because the troctolite surface limited the lateral and depth extent of both deposits; in the previous inversion results the lateral and depth extent of these deposits extended beyond the boundary of the troctolite.

Table 3.5: Maximum density contrast for the inversion constrained using the troctolite surface.

Inversion	$\Delta\rho_{max}$ (g/cm ³)
\bar{U}_{zz}	1.62
U_{xx}, U_{xy}, U_{yy}	1.65
U_{xz}, U_{yz}, U_{zz}	1.73
$U_{xx}, U_{xy}, U_{xz}, U_{yy}, U_{yz}$	1.73
$U_{xx}, U_{xy}, U_{xz}, U_{yy}, U_{yz}, U_{zz}$	1.73

Table 3.6: Standard deviation of the data difference (E) for the inversion constrained using the troctolite surface.

Inversion	U_{xx}	U_{xy}	U_{xz}	U_{yy}	U_{yz}	U_{zz}
\bar{U}_{zz}	-	-	-	-	-	2.65
U_{xx}, U_{xy}, U_{yy}	2.51	1.67	-	1.17	-	-
U_{xz}, U_{yz}, U_{zz}	-	-	2.99	-	3.07	2.60
$U_{xx}, U_{xy}, U_{xz}, U_{yy}, U_{yz}$	2.38	1.66	3.03	1.18	3.10	-
$U_{xx}, U_{xy}, U_{xz}, U_{yy}, U_{yz}, U_{zz}$	2.23	1.63	2.87	1.24	3.07	2.74

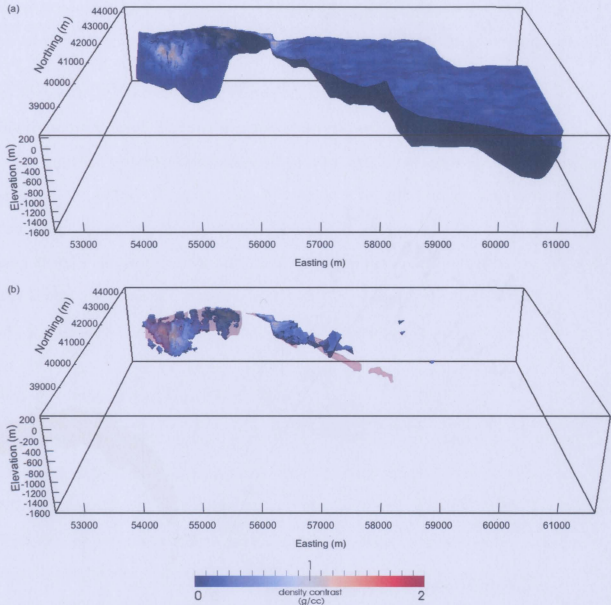


Figure 3.20: A perspective view of the recovered model using the troctolite surface as the initial model and the U_{zz} component. (a) All cells less than 0.0855 g/cm^3 have been removed to highlight the recovered troctolite unit; the true troctolite model is shown by the transparent blue overlay. (b) All cells less than 0.20 g/cm^3 have been removed to highlight the recovered sulphide deposits; the true sulphide model is shown by the transparent red overlay.

3.6.3 U_{xx} , U_{xy} , U_{yy} inversion

The recovered density contrast ranges from 0–1.65 g/cm³ (Table 3.5). The standard deviation of the data is listed in Table 3.6. The data misfit is 3557.15, well within the 5% error margin. A perspective view of the recovered density contrast is shown in Figure 3.21. Overall the recovered model is similar to the U_{zz} recovered model discussed previously. The spurious features observed along the boundary of the modelling region in previous inversion results are no longer present and the troctolite unit is accurately defined (Figure 3.21a). Several high density features are recovered (Figure 3.21b). Improvements in the recovered model are the detection of the Reid Brook and Eastern Deeps deposits; and the recovered shape, size, and density contrast of the Ovoid and Extension zone deposits when compared to the models recovered from the geologically-unconstrained inversions and those constrained using drill hole data.

3.6.4 U_{xz} , U_{yz} , U_{zz} inversion

The recovered density contrast ranges from 0–1.73 g/cm³ (Table 3.5). The standard deviation of the data is listed in Table 3.6. The data misfit is 3534.91, well within the 5% error margin. A perspective view of the recovered density contrast is shown in Figure 3.22. Overall, the result is similar to the previous two inversions. The spurious features observed in previous inversion results along the boundary of the modelling region are no longer present and the troctolite unit is accurately defined (Figure 3.22a). Several high density features are recovered and a number of small spurious features are observed near the surface within the eastern portion of the troctolite unit (Figure 3.22b). Improvements in the recovered model are the detection of the Reid Brook and Eastern Deeps deposits; and the recovered shape, size, and density contrast of the Ovoid and Extension zone deposits when compared to the models recovered from

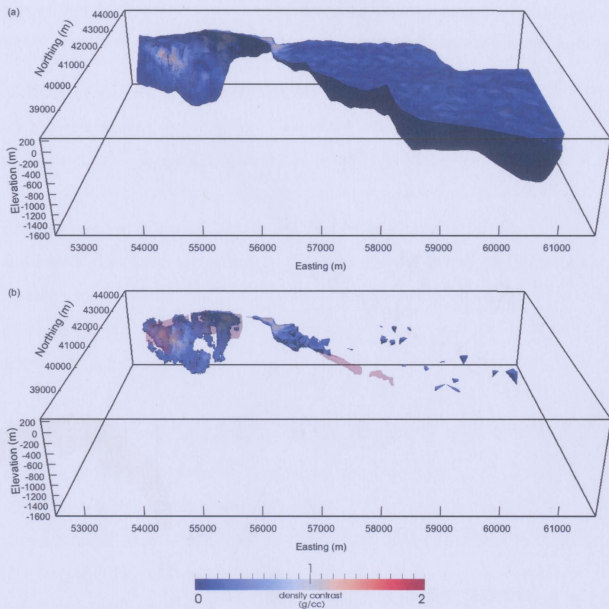


Figure 3.21: A perspective view of the recovered model using the troctolite surface as the initial model and the U_{xx} , U_{xy} , and U_{yy} components. (a) All cells less than 0.0855 g/cm^3 have been removed to highlight the recovered troctolite unit; the true troctolite model is shown by the transparent blue overlay. (b) All cells less than 0.20 g/cm^3 have been removed to highlight the recovered sulphide deposits; the true sulphide model is shown by the transparent red overlay.

the geologically-unconstrained inversions and those constrained using drill hole data.

3.6.5 U_{xx} , U_{xy} , U_{xz} , U_{yy} , U_{yz} inversion

The recovered density contrast ranges from 0–1.73 g/cm³ (Table 3.5). The standard deviation of the data is listed in Table 3.6. The data misfit is 5938.44, well within the 5% error margin. A perspective view of the recovered density contrast is shown in Figure 3.23. The spurious features observed in previous inversion results along the boundary of the modelling region are no longer present and the troctolite unit is accurately defined (Figure 3.23a). Several high density contrast features are observed and overall the results are similar to the three previous inversions (Figure 3.23b). Similar to the previous results, the most notable improvements in the recovered model are the detection of the Reid Brook and Eastern Deepes deposits; and the recovered shape, size, and density contrast of the Ovoid and Extension zone deposits.

3.6.6 U_{xx} , U_{xy} , U_{xz} , U_{yy} , U_{yz} , U_{zz} inversion

Figure 3.24 shows the predicted gradiometer data and Figure 3.25 shows the data difference between the observed and predicted data. The standard deviation of the data is listed in Table 3.6. The data misfit is 7133.60, well within the 5% error margin. The largest difference between the observed and predicted data is located over the Reid Brook and Discovery Hill deposits in the U_{xx} , U_{xy} , U_{xz} , and U_{zz} components, otherwise the data difference is suitably random. This is expected and was previously discussed in Section 3.4.5.

The recovered density contrast ranges from 0–1.73 g/cm³ (Table 3.5). A perspective view of the recovered density contrast is shown in Figure 3.26. The spurious features along the boundary of the modelling region are no longer present and the troctolite unit is accurately defined (Figure 3.26a). Several high density contrast

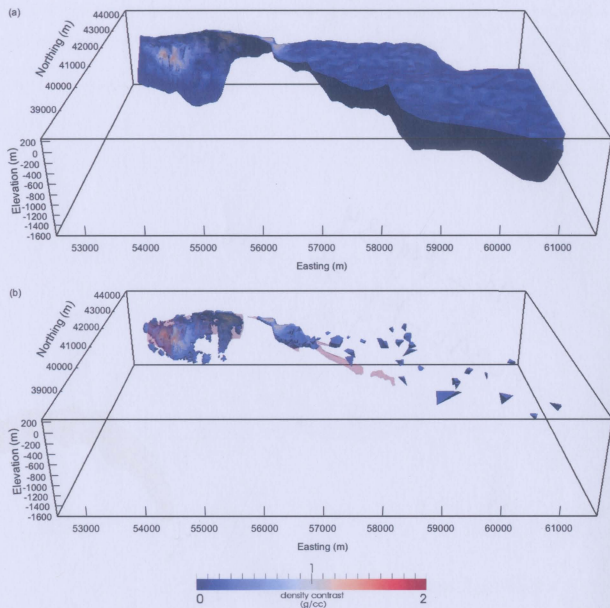


Figure 3.22: A perspective view of the recovered model using the troctolite surface as the initial model and the U_{xz} , U_{yz} , and U_{zz} components. (a) All cells less than 0.0855 g/cm^3 have been removed to highlight the recovered troctolite unit; the true troctolite model is shown by the transparent blue overlay. (b) All cells less than 0.20 g/cm^3 have been removed to highlight the recovered sulphide deposits; the true sulphide model is shown by the transparent red overlay.

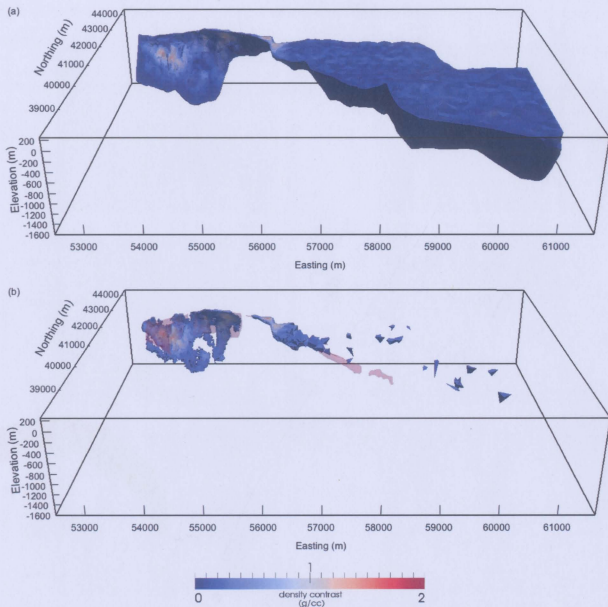


Figure 3.23: A perspective view of the recovered model using the troctolite surface as the initial model and the U_{xx} , U_{xy} , U_{xz} , U_{yy} , and U_{yz} components. (a) All cells less than 0.0855 g/cm^3 have been removed to highlight the recovered troctolite unit; the true troctolite model is shown by the transparent blue overlay. (b) All cells less than 0.20 g/cm^3 have been removed to highlight the recovered sulphide deposits; the true sulphide model is shown by the transparent red overlay.

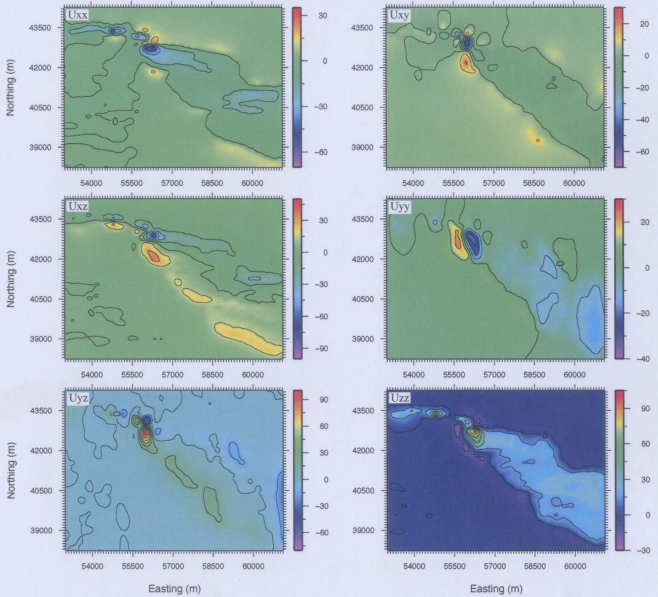


Figure 3.24: The predicted gradiometer data for the six tensor component inversion using the troctolite surface as the initial model. Units are in Eotvos. Contour interval is 15 E for U_{xx} , U_{xz} , U_{yz} , and U_{zz} and 10 E for U_{xy} and U_{yy} .

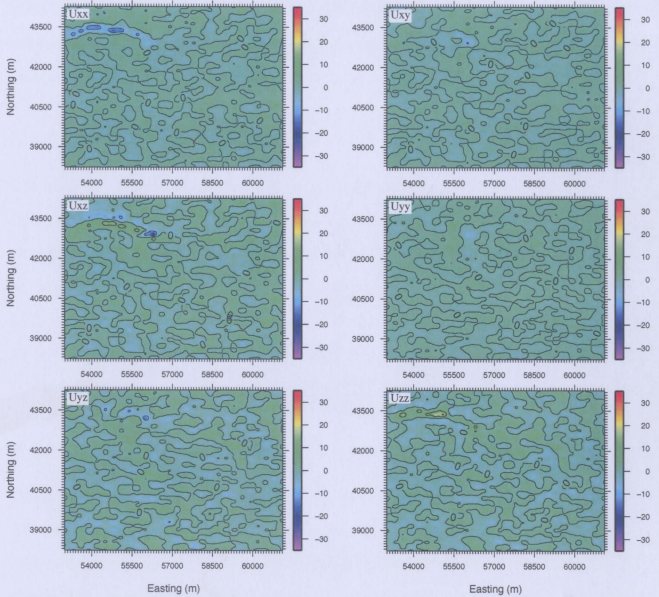


Figure 3.25: The data difference between the observed and predicted data for the six component inversion using the troctolite surface as the initial model. Units are in Eotvos. Contour interval is 10 E.

features are observed (Figure 3.26b) and overall the results are similar to the four previous inversions. Similar to the previous results, the most notable improvements in the recovered model are the detection of the Reid Brook and Eastern Deeps deposits; the Eastern Deeps sulphide is detectable to an Easting of 57100 m and a depth of approximately 500 m. A second notable improvement is the recovered shape, size and density contrast of the Ovoid and Extension zone deposits.

3.6.7 Constrained example B

Constrained example B differs from constrained example A in the bounds used to constrain the inversion: as before the troctolite is allowed to vary between a lower bound of 0.0855 g/cm^3 and an upper bound of 1.7325 g/cm^3 but the gneiss is allowed to vary between a lower bound of 0 g/cm^3 and an upper bound of 1.7325 g/cm^3 . The high upper bound for both units allows high density material (*i.e.* sulphide deposits) to be incorporated. Again, a distance weighting was used with $\beta = 2$ and $r_0 = 1$ (Equation 2.22).

3.6.8 $U_{xx}, U_{xy}, U_{xz}, U_{yy}, U_{yz}, U_{zz}$ inversion

Due to the redundancy of the results, only the six component inversion is shown. The six component inversion adequately represents how changing the density bounds affects the resulting model. The recovered density contrast ranges from $0-0.754 \text{ g/cm}^3$ (Table 3.7). The standard deviation of the data difference is listed in Table 3.7. The data misfit is 7168.94, well within the 5% error margin. A perspective view of the recovered density contrast is shown in Figure 3.27. Overall, the result closely resembles the geologically-unconstrained results (Figures 3.12): five dense bodies are recovered associated with the Reid Brook, Discovery Hill, Ovoid, and Extension Zone deposits (west to east). The maximum density anomaly is too low, and the shape and size of

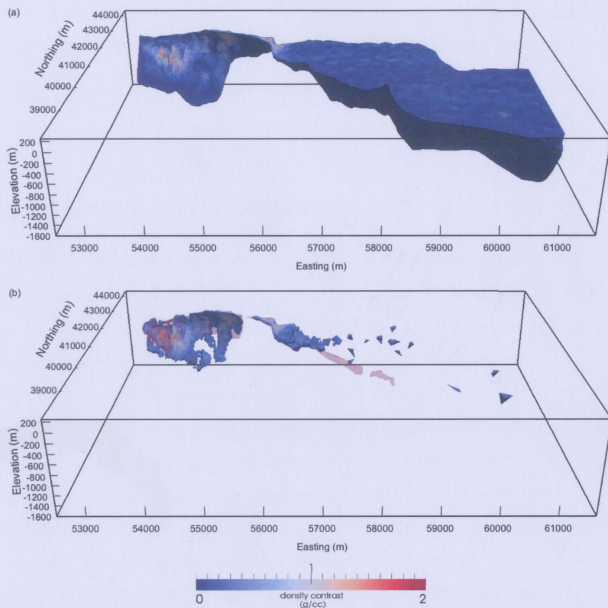


Figure 3.26: A perspective view of the recovered model for the inversion result using the troctolite surface as the initial model and all six tensor components. (a) All cells less than 0.0855 g/cm^3 have been removed to highlight the recovered troctolite unit; the true troctolite model is shown by the transparent blue overlay. (b) All cells less than 0.20 g/cm^3 have been removed to highlight the recovered sulphide deposits; the true sulphide model is shown by the transparent red overlay.

the deposits is not recovered.

Table 3.7: Standard deviation of the data difference (E) and maximum density contrast (g/cm^3) for the six component inversions constrained using the troctolite surface.

Inversion	U_{xx}	U_{xy}	U_{xz}	U_{yy}	U_{yz}	U_{zz}	$\Delta\rho_{max}$
Constrained Example A	2.23	1.63	2.87	1.24	3.07	2.74	1.73
Constrained Example B	1.47	1.34	1.98	0.80	2.47	1.75	0.754

3.7 Geologically-constrained inversion: true model

The final example is a geologically-constrained inversion result using the true density model as the initial model. In this case, it is assumed the sulphide, troctolite, and gneiss units are fully defined by surface mapping and drilling; the sulphide and troctolite surfaces were included in the initial model and bound constraints were applied. The sulphide units were assigned a density of $1.65 \text{ g}/\text{cm}^3$ with a lower bound of $1.5675 \text{ g}/\text{cm}^3$ and an upper bound of $1.7325 \text{ g}/\text{cm}^3$. The troctolite unit was assigned a density of $0.09 \text{ g}/\text{cm}^3$ with a lower bound of $0.0855 \text{ g}/\text{cm}^3$ and an upper bound of $0.0945 \text{ g}/\text{cm}^3$. The gneiss unit was assigned a density of $0 \text{ g}/\text{cm}^3$ with a lower density bound of $0 \text{ g}/\text{cm}^3$ and an upper bound of $0.0045 \text{ g}/\text{cm}^3$. The bounds for troctolite unit and sulphide deposits are $\pm 10\%$ the true density value. A distance weighting was used with $\beta = 2$ and $r_0 = 1$ (Equation 2.22).

3.7.1 Inversion results

Due to the redundancy of the results, only the six tensor component inversion is presented here. Figure 3.28 shows the predicted gradiometer data and Figure 3.29 shows the data difference between the observed and predicted data. Overall, the data difference is suitably random. The standard deviation of the data difference is 2.01 E

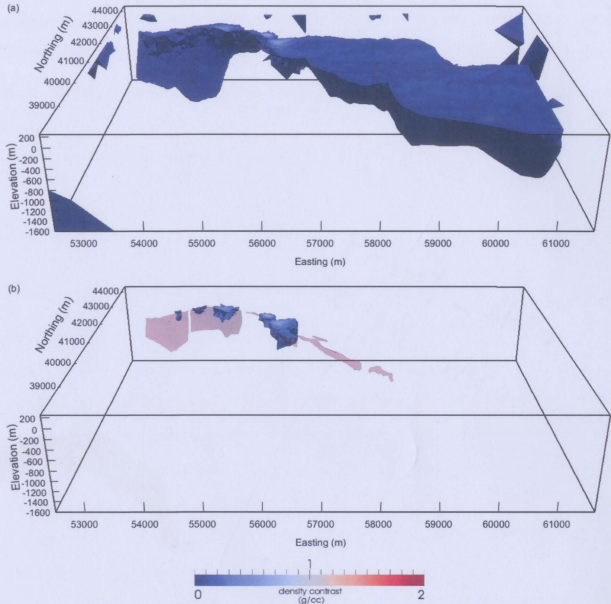


Figure 3.27: A perspective view of the recovered model for the inversion result using the troctolite surface as the initial model and all six tensor components. The bounds differ from the previous result. (a) All cells less than 0.0855 g/cm^3 have been removed to highlight the recovered troctolite unit; the true troctolite model is shown by the transparent blue overlay. (b) All cells less than 0.20 g/cm^3 have been removed to highlight the recovered sulphide deposits; the true sulphide model is shown by the transparent red overlay.

for the U_{xx} component, 1.66 E for the U_{xy} component, 2.67 E for the U_{xz} component, 1.25 E for the U_{yy} component, 3.18 E for the U_{yz} component, and 2.48 E for the U_{zz} component. The data misfit is 6983.85, well within the 5% error margin.

The recovered density contrast ranges from 0–1.5675 g/cm³. A perspective view of the recovered model is shown in Figure 3.30. As expected, the inversion model resembles the initial model and faithfully reproduces the sulphide and troctolite units. This is not surprising since the initial density model was accurately defined.

3.8 Summary of results

3.8.1 Unstructured tetrahedral meshes

The Voisey's Bay modelling mesh contained surfaces for the boundary of the modelling region, the topography, and geological contacts between the sulphide, troctolite, and gneiss units. Creating the *poly* file using FacetModeller was time consuming because the model had to include all known geology in order to generate synthetic data using the forward modelling program *gravity_fwd*. The main advantage was the geological contacts could be incorporated directly into the mesh and no information was lost by converting to a rectilinear mesh, *i.e.* the fine scale structure could be represented by the unstructured tetrahedral mesh.

It was difficult to generate a high quality mesh for two reasons. First, TetGen would stall if too many surfaces were incorporated or if high quality was demanded, *i.e.* if a small minimum radius-edge ratio and/or a small maximum tetrahedron volume was specified (Section 2.2.2). Second, if the problem has a large amount of data and the mesh has a large number of cells, the memory necessary to solve the problem can exceed the available computer memory.

One way to reduce the number of cells in the mesh and thus reduce the size of the

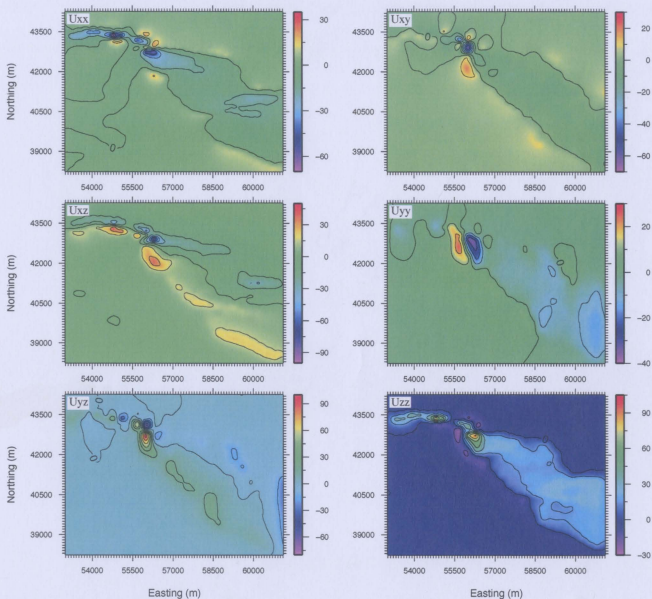


Figure 3.28: The predicted gradiometer data for the six tensor component inversion using the true model as the initial model. Units are in Eotvos. Contour interval is 15 E for U_{xx} , U_{xz} , U_{yz} , and U_{zz} and 10 E for U_{xy} and U_{yy} .

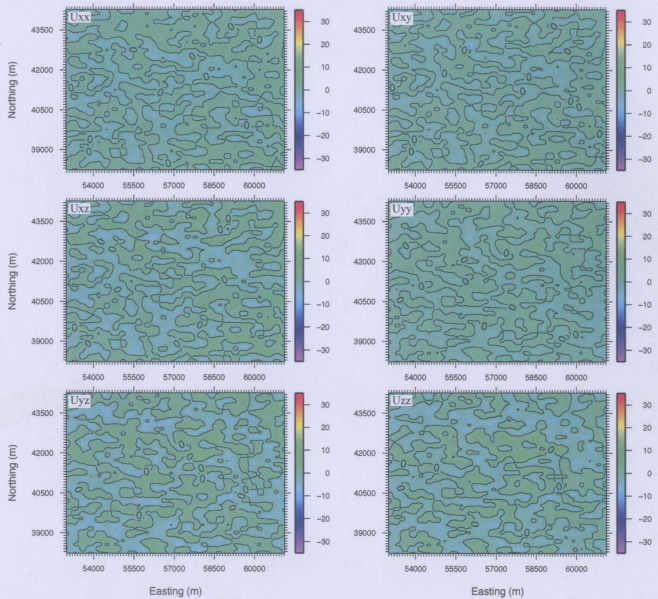


Figure 3.29: The data difference between the observed and predicted data for the six component inversion using the true model as the initial model. Units are in Eotvos. Contour interval is 10 E.

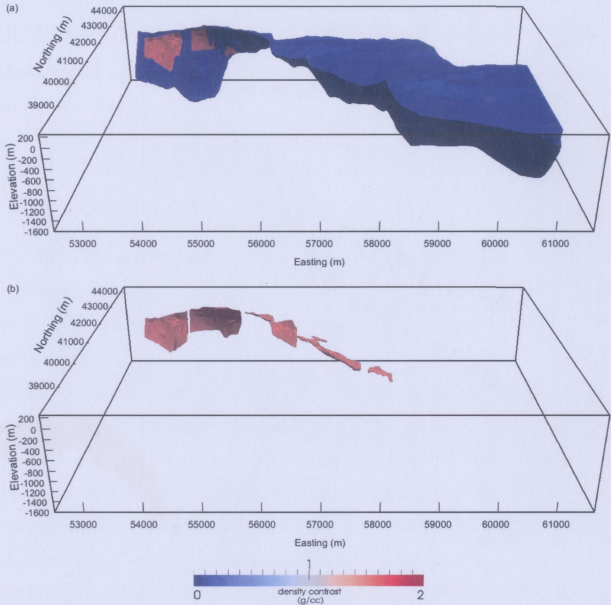


Figure 3.30: A perspective view of the recovered model for the inversion result using the true model as the initial model and all six tensor components. (a) All cells less than 0.0855 g/cm^3 have been removed to highlight the recovered troctolite unit. (b) All cells less than 0.20 g/cm^3 have been removed to highlight the recovered sulphide deposits.

problem is to utilize any available geological data. For example, when the troctolite surface is incorporated into the mesh, the cells within the troctolite unit can have a smaller maximum tetrahedron volume while the cells outside of the troctolite unit can have a larger maximum tetrahedron volume. This assumes that all cells outside of the troctolite unit are known to be gneiss and as a result tight bounds are applied to all the gneiss cells.

3.8.2 Geologically unconstrained versus constrained inversion

The discussion on geologically-constrained inversions focuses on the six tensor component inversion results, but the discussion is equally applicable to the inversion results that used less tensor components. Vertical cross-sections are used to demonstrate the effect adding geological constraints has on the resulting models. The cross-sections intersect the Reid Brook (Figure 3.31); Discovery Hill (Figure 3.32); Ovoid (Figure 3.33); Extension zone (Figure 3.34); and Eastern Deepes (Figure 3.35).

A common first step in many exploration programs is to perform geologically-unconstrained inversions to obtain subsurface estimates of the density. The recovered models constructed using a zero-density initial model are typical of minimum-structure inversion: the features are diffuse and smeared out and the maximum anomalous density is less than that of the massive sulphide (Figures 3.31a-3.35a). Some of the key features are resolved in the models; such as the surface edge of the troctolite and the approximate location of the Discovery Hill, Ovoid, and Extension zone deposits. Overall, the recovered shape, size, and density contrast is not representative of the true sulphide deposits. In the context of mineral exploration, this would be a valuable result in a green field situation but the value is diminished once a target has been identified and its delineation has begun.

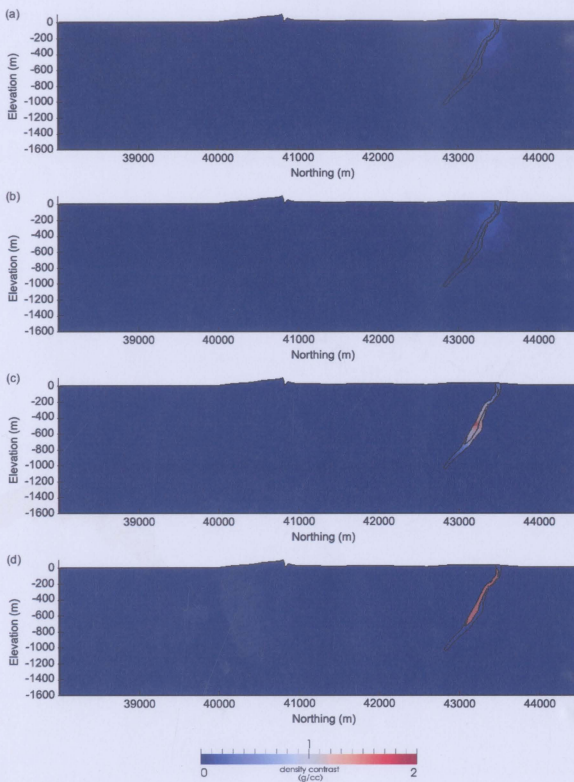


Figure 3.31: Vertical cross sections through Reid Brook (Easting 53800 m) highlight the effect geological-constraints have on the resulting models: (a) geologically-unconstrained; (b) constrained using three drill holes; (c) constrained using the troctolite surface; and (d) constrained using the true model. The inversion results are shown using all six tensor components. The black outline shows the true model.

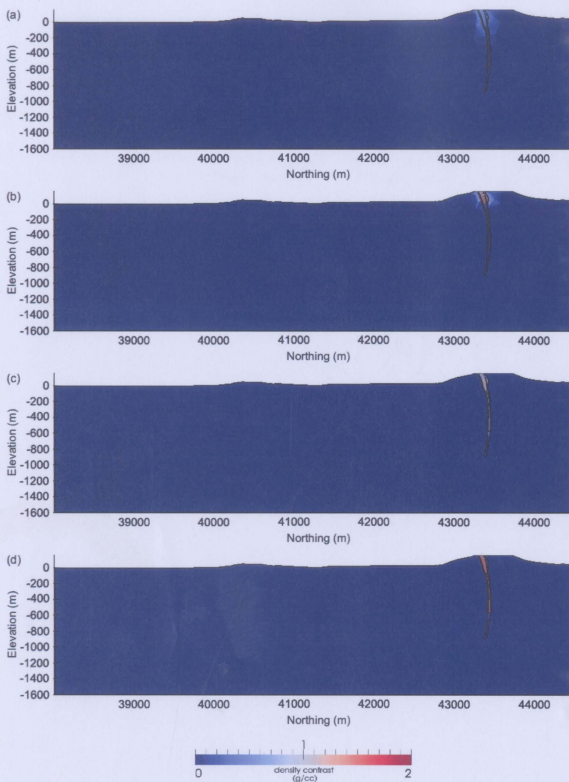


Figure 3.32: Vertical cross sections through Discovery Hill (Easting 54900 m) highlight the effect geological-constraints have on the resulting models: (a) geologically-unconstrained; (b) constrained using three drill holes; (c) constrained using the troctolite surface; and (d) constrained using the true model. The inversion results are shown using all six tensor components. The black outline shows the true model.

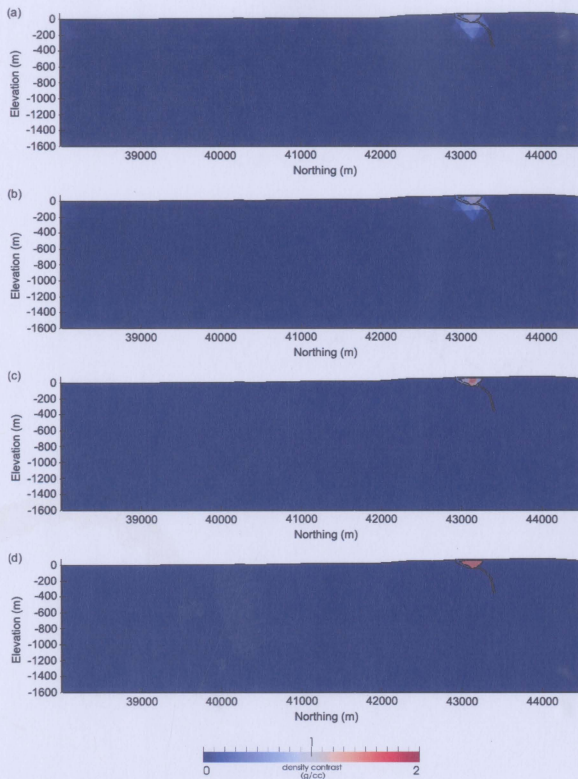


Figure 3.33: Vertical cross sections through the Ovoid (Easting 55850 m) highlight the effect geological-constraints have on the resulting models: (a) geologically-unconstrained; (b) constrained using three drill holes; (c) constrained using the troctolite surface; and (d) constrained using the true model. The inversion results are shown using all six tensor components. The black outline shows the true model.

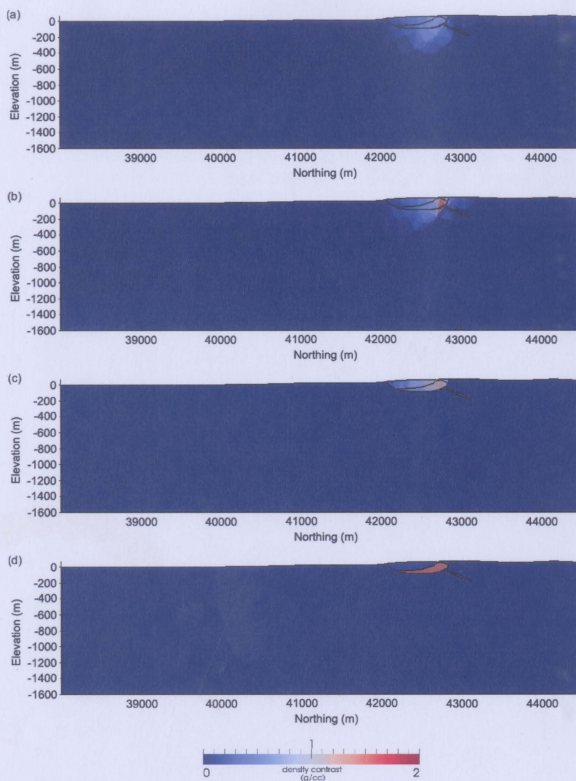


Figure 3.34: Vertical cross sections through the Extension Zone (Easting 56100 m) highlight the effect geological-constraints have on the resulting models: (a) geologically-unconstrained; (b) constrained using three drill holes; (c) constrained using the troctolite surface; and (d) constrained using the true model. The inversion results are shown using all six tensor components. The black outline shows the true model.

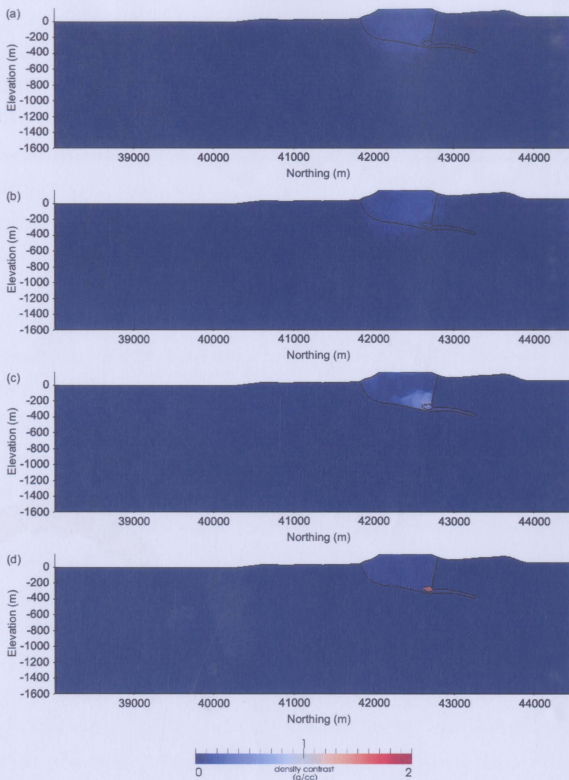


Figure 3.35: Vertical cross sections through Eastern Deeps (Easting 56600 m) highlights the effect geological-constraints have on the resulting models: (a) geologically-unconstrained; (b) constrained using three drill holes; (c) constrained using the troctolite surface; and (d) constrained using the true model. The inversion results are shown using all six tensor components. The black outline shows the true model.

A reliable inversion result can only be recovered by including geology-based constraints as well as the standard mathematical constraints (Ash, 2007; McGaughey, 2007; Farquharson et al., 2008; Williams, 2008; Lelièvre, 2009; Williams et al., 2009). Several geologically-constrained inversion scenarios were investigated. The first scenario used density data from three drill holes located at (56130, 42750, 75), (55880, 43150, 70), and (54930, 43380, 175) (Figures 3.31b-3.35b); the second scenario used a volume model of the troctolite (Figures 3.31c-3.35c); and the final scenario used the true model to constrain the inversion (Figures 3.31d-3.35d).

The first geologically-constrained scenario used density data from three drill holes. In the vicinity of the drill hole (Figures 3.32b-3.34b) the model is improved over the default model (Figures 3.32a-3.34a). In comparison, when the model is examined away from any drill holes (Figures 3.31b and 3.35b) the results are nearly identical to the geologically-unconstrained models (Figures 3.31a and 3.35a). Overall, the recovered models show improvement over the geologically-unconstrained models: the maximum anomalous density is within an acceptable range for the massive sulphide (5% less than the true density). However, the improvement did not extend beyond the location of the drill holes. Also, the features in all the recovered models were still diffuse and smeared out. In the context of mineral exploration, this would be a valuable result at the early stages of a drilling program.

The second geologically-constrained scenario used a volume model of the troctolite unit. This is the first example to take advantage of incorporating a geological surface into the initial model. Two cases were investigated and the results show that including a geological surface can improve the inversion result if the density bounds are selected carefully. In the first case the density bounds restricted the range on the gneiss unit (0-0.0045 g/cm³) but allowed the troctolite unit to contain high density material (0.0855-1.7325 g/cm³). The resulting models (Figures 3.31c-3.35c) are clearly better

than the unconstrained models (Figures 3.31a-3.35a) as well as those constrained using a small amount of density data from drill holes (Figure 3.31b-3.35b). More importantly, these models are also an improvement over the initial model used to constrain the inversions. There is notable improvement in the detection of the Reid Brook (Figure 3.31c) and the Eastern Deeps deposits (Figure 3.35c). These deposits were undetected in the previous two inversion scenarios. With appropriate bounds, the troctolite surface also constrained the shape, size, and density contrast of the Ovoid (Figure 3.33c) and Extension zone deposits (Figure 3.34c). In the second case the density bounds allowed both the gneiss ($0-1.7325 \text{ g/cm}^3$) and troctolite ($0.0855-1.7325 \text{ g/cm}^3$) units to contain high density material. The resulting model was no better than the geologically-unconstrained result.

The final geologically-constrained scenario used the true model to constrain the inversion. As expected, the inversion model resembles the initial model and faithfully reproduces the troctolite unit and sulphide deposits (Figures 3.31d-3.35d). This is not surprising since the initial model was accurately defined.

3.8.3 Single versus multiple component inversion

The effect single and multiple components have on the resulting inverted model structure and recovered density contrast was investigated. The recovered maximum density anomaly (Table 3.8) and vertical cross-sections are used to demonstrate the effect adding more tensor components has on the resulting models. The cross-sections intersect the Extension Zone through Easting 56100 m (Figures 3.36-3.38).

For the geologically-unconstrained inversions, noticeable improvements were observed in the model structure and density contrast values (Figure 3.36). The results show that the single component inversion contains a larger, less dense body (Figure 3.36a) whereas the six component inversion contains a smaller, more dense body (Fig-

Table 3.8: Density range for the geologically-unconstrained, constrained using density data from three drill holes, and constrained using the troctolite surface. Density values are in g/cm^3 .

Components	Unconstrained	Drill holes	Troctolite surface
U_{zz}	0-0.339	0-1.57	0-1.62
U_{xx}, U_{xy}, U_{yy}	0-0.511	0-1.57	0-1.65
U_{xx}, U_{yz}, U_{zz}	0-0.478	0-1.57	0-1.73
$U_{xx}, U_{xy}, U_{xz}, U_{yy}, U_{yz}$	0-0.614	0-1.57	0-1.73
$U_{xx}, U_{xy}, U_{xz}, U_{yy}, U_{yz}, U_{zz}$	0-0.755	0-1.57	0-1.73

ure 3.36e). Incorporating the additional gradient components into the inversion significantly improves density results over single component inversion by better defining the depth extent of the ore bodies. Not only have the results from the six component inversion tightened the boundaries of the recovered troctolite and ore bodies but have also shifted the centre of density contrast corresponding to the ore body towards the proper position indicated by the true model boundaries. Overall, the results contain less spurious features and become more compact with a higher maximum density anomaly (Table 3.8) as more tensor components are used to construct the model.

For the geologically-constrained inversions using density data from three drill holes, noticeable improvements were observed in model structure but the maximum density anomaly stayed the same (Table 3.8). Near the drill holes, the results are similar regardless of how many tensor components are used (Figure 3.37). This is not surprising as the density data is accurately defined in the cells that are intersected by the drill holes. When the results are examined away from any drill holes, there is a clear improvement in model structure as more tensor components are used to construct the model. Overall, the results contain less spurious features and anomalous bodies become more compact.

For the geologically-constrained inversions using the troctolite surface, increasing

the number of components in the inversion does not result in a noticeable difference in the model structure or maximum anomalous density (Figure 3.38 and Table 3.8). When the geology is well constrained, computation time can be reduced by using the U_{zz} or three tensor components only.

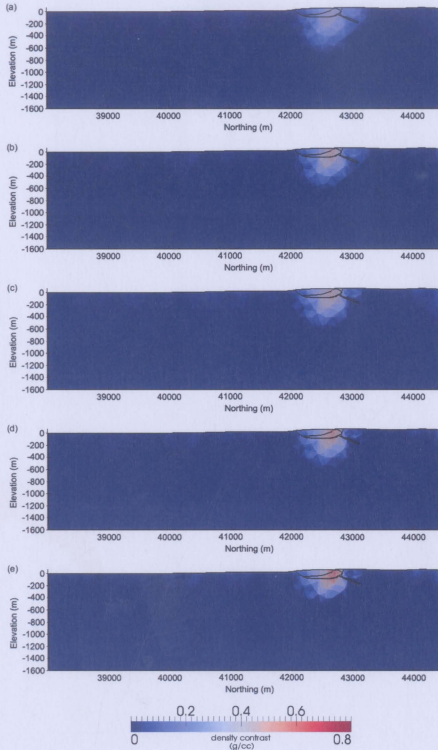


Figure 3.36: Vertical cross sections through the Extension Zone (Easting 56100 m) highlights the differences between single and multi component inversion results for the geologically-unconstrained scenario: (a) U_{zz} ; (b) U_{xx}, U_{xy}, U_{yy} ; (c) U_{xz}, U_{yz}, U_{zz} ; (d) $U_{xx}, U_{xy}, U_{xz}, U_{yy}, U_{yz}$; and (e) $U_{xx}, U_{xy}, U_{xz}, U_{yy}, U_{yz}, U_{zz}$. The black outline shows the true model.

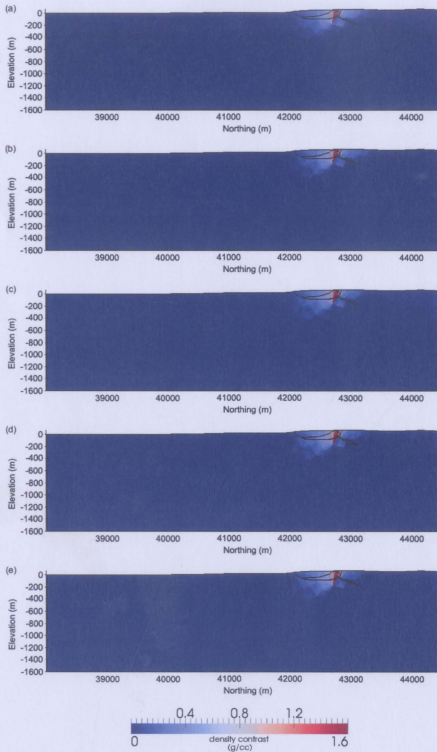


Figure 3.37: Vertical cross sections through the Extension Zone (Easting 56100 m) highlights the differences between single and multi component inversion results for the geologically-constrained scenario using three drill holes: (a) U_{zz} ; (b) U_{xx}, U_{xy}, U_{yy} ; (c) U_{xx}, U_{yz}, U_{zz} ; (d) $U_{xx}, U_{xy}, U_{xz}, U_{yy}, U_{yz}$; and (e) $U_{xx}, U_{xy}, U_{xz}, U_{yy}, U_{yz}, U_{zz}$. The black outline shows the true model.

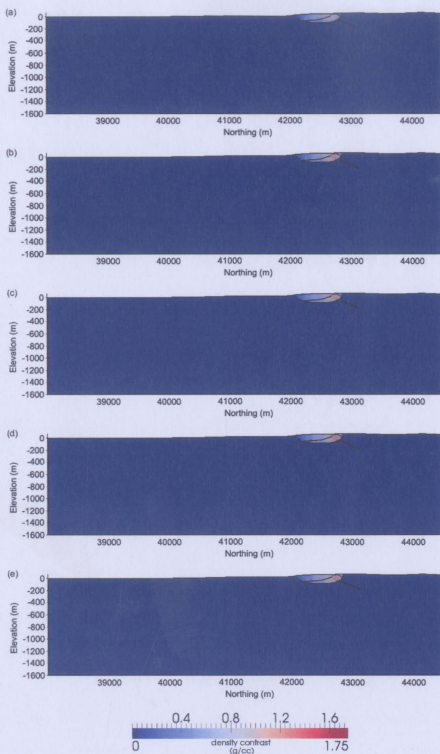


Figure 3.38: Vertical cross sections through the Extension Zone (Easting 56100 m) highlights the differences between single and multiple component inversion results for the geologically-constrained scenario using the troctolite surface: (a) U_{zz} ; (b) U_{xx} , U_{xy} , U_{yy} ; (c) U_{xx} , U_{yz} , U_{zz} ; (d) U_{xx} , U_{xy} , U_{xz} , U_{yy} , U_{yz} ; and (e) U_{xx} , U_{xy} , U_{xz} , U_{yy} , U_{yz} , U_{zz} . The black outline shows the true model.

Chapter 4

Real data inversions: Mushuau intrusion

4.1 Overview

An example based on the Mushuau intrusion (Figures 1.2 and 4.1) demonstrates the use of single versus multiple components in gravity gradient inversions using a real data set collected by Bell Geospace Inc. in 2006 and 2007. The inversions are performed using the forward modelling and minimum-structure inversion procedures discussed in Chapter 2. Inversion is attempted using five different tensor component combinations: (i) U_{zz} ; (ii) U_{xx} , U_{xy} , U_{yy} ; (iii) U_{xz} , U_{yz} , U_{zz} ; (iv) U_{xx} , U_{xy} , U_{xz} , U_{yy} , U_{yz} ; and (v) U_{xx} , U_{xy} , U_{xz} , U_{yy} , U_{yz} , U_{zz} . The combinations are the same ones previously used for the Voisey's Bay deposits synthetic data inversions (Chapter 3). Computer memory limitations were encountered when attempting to invert the full data set. The full dataset was broken into two smaller datasets to reduce the overall problem size. The smaller of the two datasets is located over the Asini prospect and the larger of the two datasets is located over the Sarah prospect. Data difference

plots and predicted data plots are only shown for the six component inversion cases due to the redundancy of the plots. All inversions show an acceptable data misfit and reproduce the observed gravity gradient data. Geologically-constrained inversions were not investigated because geological data was not available.

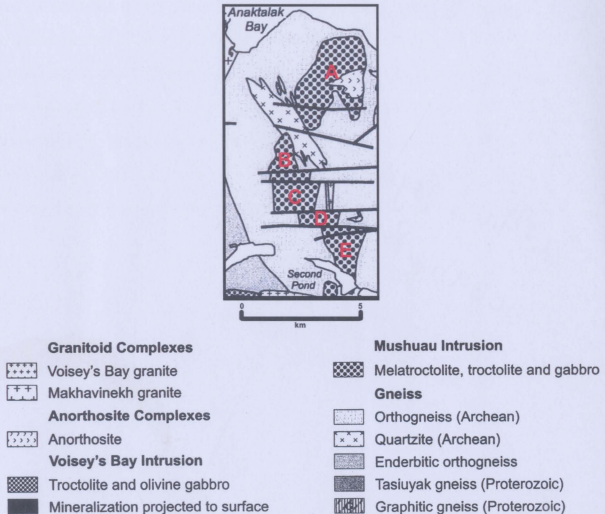


Figure 4.1: The Mushuau intrusion consists of two prospects: the Asini prospect to the north (A) and the Sarah prospect to the south (B through E) (modified from Li et al., 2000).

4.2 Airborne gravity gradiometer data

The data was provided by Vale and flown by Bell Geospace Inc. in 2006 and 2007 using the Air-FTG gravity gradiometer (Bell Geospace, 2007). Two sets of surveys were initially designed in the same area, the main survey (Garland Lake property) and an extension survey (Voisey's Bay). The Mushuau intrusion is located within the extension survey. The extension survey was flown in a north-south direction with lines spaced 200 m apart (Figure 4.2). Tie lines were flown in an east-west direction at a lines spacing of 1000 m. The planned flight height was at 80 m altitude standard tie-drape while maintaining a constant distance from the ground, but due to topography variations the flight altitude varies from approximately 60-500 m. A subset of the extension survey data is used to perform inversions over the Mushuau intrusion.

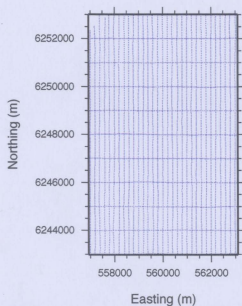


Figure 4.2: The flight path over the Mushuau intrusion. The blue dots show the flight lines, lines spacing and sampling along flight lines.

Prior to data delivery, Bell Geospace Inc. completed routine proprietary processing and corrections for residual aircraft motion and self-gradient to the acquired data. They also demodulated, filtered, and levelled the data before removing the terrain

effect using a density of 2.80 g/cm^3 (Figure 4.3). Estimates of the measurement uncertainties were not provided, so uncertainties of 10 E were assumed for the inversions. The data were also transformed from a left-handed coordinate system to a right-handed coordinate system before inverting (Appendix D.1).

As previously discussed (Section 2.1.2.3), the different tensor components give different information on the geological attributes of the subsurface (Figure 4.3). Overall, the gravity gradient anomaly over the Asini prospect dominates the response with a smaller anomaly over the Sarah prospect. The U_{zz} component contains a large positive anomaly over the Asini prospect and a smaller positive anomaly over the Sarah prospect. The U_{xx} component delineates the extent of the northern and southern edges of the Asini and Sarah prospect troctolites; both prospects are identified by the large negative anomalies associated with them. The U_{yy} component delineates the extent of the eastern and western edges of the Asini and Sarah prospect troctolites; similar to the U_{xx} component, both prospects are identified by large negative anomalies. The U_{xy} component identifies any corners. The U_{xz} component changes sign along the north-south centre of mass of the Asini prospect troctolites and along the northeast-southwest centre of mass of the Sarah prospect troctolites. The U_{yz} component changes sign along the east-west centre of mass of the Asini prospect troctolites and along the northeast-southwest centre of mass of the Sarah prospect troctolites.

4.3 Mushuau Intrusion inversions

The modelling region is 6400 m by 10400 m by 2222 m (Easting by Northing by depth) and the topography has an elevation range of 422 m. A quality mesh was generated by using a minimum radius-edge ratio of $q = 2$ and a maximum tetrahedron volume of $a = 2,000,000$ giving a total of 231,770 cells.

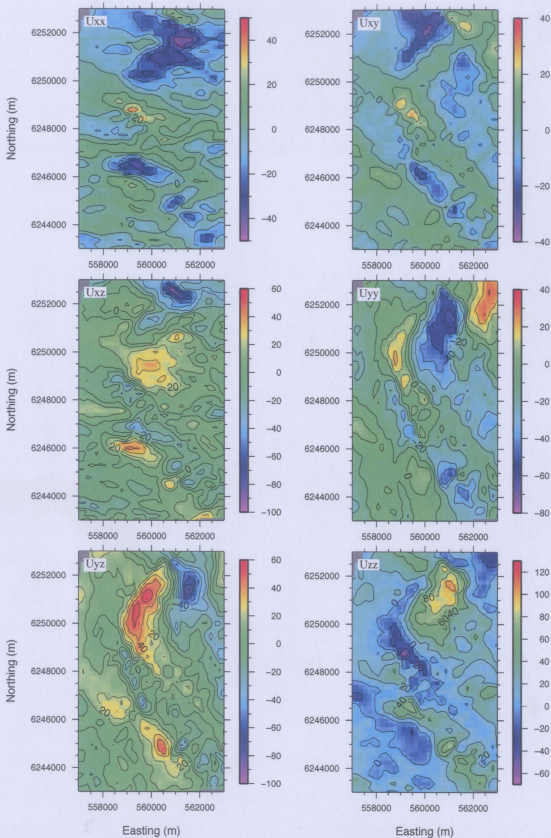


Figure 4.3: The terrain corrected gradiometer data observed above the Mushuau intrusion. Units are in Eotivs. Contour interval is 5 E for the U_{xx} , U_{xy} , U_{xz} , U_{yy} , and U_{yz} components and 10 E for the U_{zz} component.

Geologically-unconstrained gravity gradient inversions were performed using a zero-density initial model so that no assumptions were made about the geologic features. The density bounds were applied as a global constraint to the entire mesh and constrained to a lower bound of -5.0 g/cm^3 and an upper bound of 5.0 g/cm^3 . These bounds were selected to allow an unrestricted recovery of density contrasts while still maintaining a plausible range of densities. A distance weighting was used with $\beta = 1.5$ and $r_0 = 1$ (Equation 2.22).

4.3.1 Inversion results

The single-component inversion serves as a base model to compare whether the addition of more components increases the quality of the resulting model (Martinez and Li, 2011). A series of preliminary inversions varying the *chifact* value was carried out in order to select the optimal regularization parameter (Appendix D.2). The ideal *chifact* will reproduce a data misfit value ϕ_d that equals the total number of data points multiplied by the *chifact* value within a 5% error margin. A *chifact* value of 0.75 was found to provide the optimal trade-off between model structure and data misfit; it is used for all the inversions in this chapter.

The predicted data and difference data maps are omitted for the sake of brevity. The range of values seen between the observed and predicted data are an indication of the noise in the data which the recovered model does not fit. The standard deviation calculated from the data difference is 8.52 E. The density contrast model was created using 5854 data points and the data misfit is 4248.08, well within the 5% error margin.

The recovered density contrast ranges from -0.181 – 0.362 g/cm^3 . A perspective view of the recovered density contrast model is shown in Figure 4.4 with all cells between 0 and 0.15 g/cm^3 removed for clarity. There are several high and low density contrast bodies remaining. The large dense feature located in the northern portion of

the modelling region corresponds to the troctolites of the Asini prospect. A smaller dense feature is located to the northwest of the Asini prospect, but it is not known what the dense feature correlates with. There are also several smaller dense features located south of the Asini prospect. These smaller bodies are trending northwest-southeast and correspond to the troctolites of the Sarah prospect. The centrally located low density body corresponds to the Archean aged quartzite. It is not known what the remaining low density features correlate with.

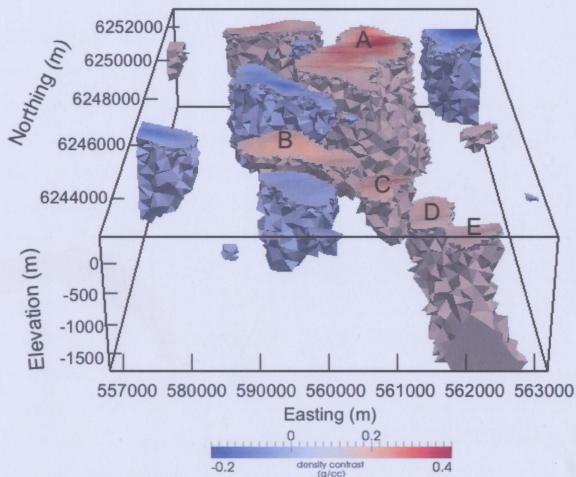


Figure 4.4: A perspective view of the recovered model for the unconstrained inversion result using the U_{zz} component. All cells between 0 and 0.15 g/cm^3 have been removed. The Asini prospect is denoted by the A and the Sarah prospect is denoted by B through E.

Inversions using more than a single component were not obtained due to computer

memory limitations. The available computer memory was 26 gigabytes: the single component inversion required 13 gigabytes of memory and the three component inversion required 33 gigabytes of memory. Consequently, a subset of the data (from over the Asini prospect) was selected to attempt inversions with three or more tensor components.

4.4 Asini prospect inversions

Following from the results obtained from the Mushuau intrusion, a subset of the data was selected to perform inversions over the Asini prospect (Figure 4.5). The smaller problem size enables three, five, and six component inversions to be performed.

The modelling region is 4800 m by 4400 m by 2190 m (Easting by Northing by depth) and the topography has an elevation range of 386 m. A quality mesh was generated by using a minimum radius-edge ratio of $q = 2$ and a maximum tetrahedron volume of $a = 600,000$ giving a total of 157,574 cells. The same mesh was used for all inversions. This mesh is finer than the mesh previously used for the Mushuau intrusion inversion.

Geologically-unconstrained gravity gradient inversions were performed using a zero-density initial model so that no assumptions were made about the geologic features. The density bounds were applied as a global constraint to the entire mesh and constrained to a lower value of -5 g/cm^3 and an upper bound of 5 g/cm^3 . A distance weighting was used with $\beta = 1.5$ and $r_0 = 1$ (Equation 2.22).

4.4.1 U_{zz} inversion

The single-component inversion serves as a base model to compare whether the addition of more components increases the quality of the resulting model (Martinez and

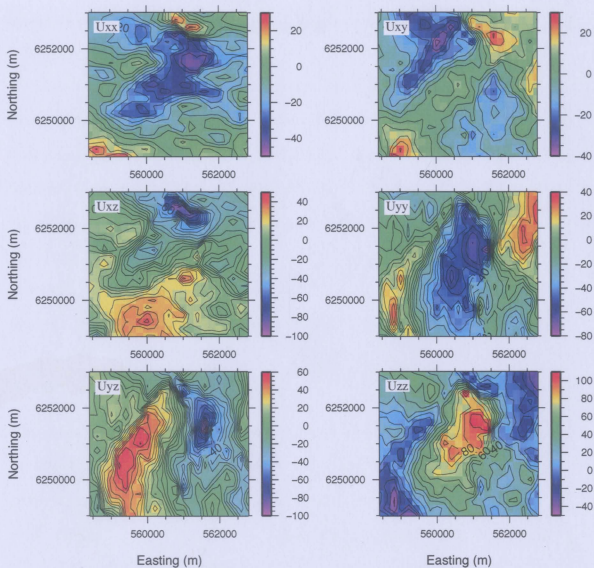


Figure 4.5: The subset of gradiometer data used to perform inversion over the Asini prospect. Units are in Eotvos. Contour interval is 10 E for U_{xx} , U_{xy} , U_{xz} , U_{yy} , and U_{yz} and 20 E for U_{zz} .

Li, 2011). The predicted data and difference data maps are omitted for brevity. The range of values seen between the observed and predicted data are an indication of the noise in the data which the recovered model does not fit. The standard deviation calculated from the data difference is 8.55 E, which is consistent with the noise level observed in the full model inversion of 8.52 E. The density model was created using 1799 data points and the data misfit is 1313.63, well within the 5% error margin.

The recovered density contrast ranges from -0.212 – 0.350 g/cm³ (Table 4.2). A perspective view of the recovered model is shown in Figure 4.6 with all cells below 0.20 g/cm³ removed for clarity. As expected, the result is similar to the northern portion of the model obtained by inverting the U_{zz} component for the entire data set (Figure 4.4). The remaining high density contrast shows two dense features. The large, centrally located dense feature corresponds to the troctolites of the Asini prospect. A second, smaller dense feature is located to the northwest of the Asini prospect. It is not known what the dense feature correlates with.

4.4.2 U_{xx} , U_{xy} , U_{yy} inversion

The standard deviation of the data difference is 7.37 E for the U_{xx} component, 6.96 E for the U_{xy} component, and 9.85 for the U_{yy} component. The density model was created using 5397 data points and the data misfit is 3887.05, well within the 5% error margin.

The recovered density contrast ranges from -0.112 – 0.285 g/cm³ (Table 4.2). A perspective view of the recovered model is shown in Figure 4.7. Two dense features are observed. The features have a lower maximum density contrast when compared to the U_{zz} model. The centrally located dense feature corresponding to the Asini prospect is more compact than the U_{zz} model with the boundaries being significantly tightened to the source location of the structure. The second dense feature located in

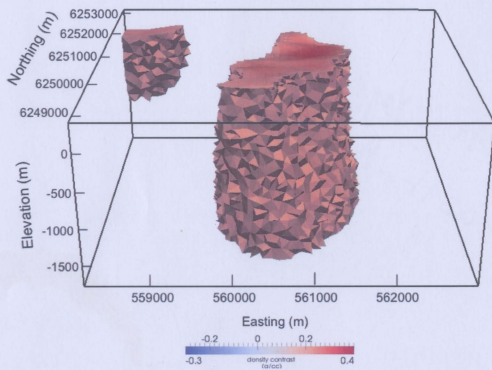


Figure 4.6: A perspective view of the recovered model for the unconstrained inversion results using the U_{zz} component showing the 0.20 g/cm^3 isosurface.

the northwest corner is larger and extends to a greater depth than the U_{zz} model.

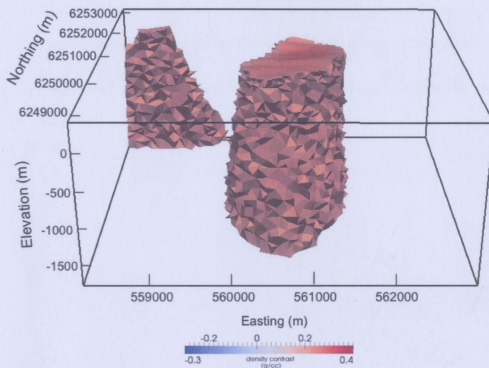


Figure 4.7: A perspective view of the recovered model for the unconstrained inversion results using the U_{xx} , U_{xy} , U_{yy} components showing the 0.20 g/cm^3 isosurface.

4.4.3 U_{xz} , U_{yz} , U_{zz} inversion

Inversion of the U_{xz} , U_{yz} , U_{zz} tensor components obtains a density contrast distribution using 5397 data points. The standard deviation of the data difference is 7.51 E for the U_{xz} component, 7.89 E for the U_{yz} component, and 9.29 E for the U_{zz} component.

The recovered density contrast ranges from -0.219 – 0.340 g/cm^3 (Table 4.2). A perspective view of the recovered model is shown in Figure 4.8. Two dense features are observed. The features have a higher maximum density contrast when compared to the U_{xx} , U_{xy} , U_{yy} model but a lower maximum density contrast compared to the U_{zz} model. The centrally located dense feature corresponding to the Asini prospect is less compact than the previous two models. This is especially true at depth where

the high density material extends laterally to the south. The second dense feature located in the northwest corner is similar in size to the U_{xx} , U_{xy} , U_{yy} model.

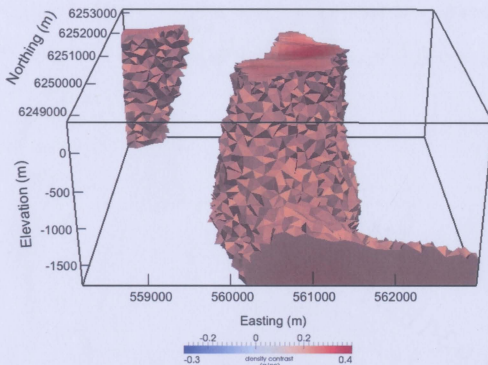


Figure 4.8: A perspective view of the recovered model for the unconstrained inversion results using the U_{xx} , U_{yz} , U_{zz} components showing the 0.20 g/cm^3 isosurface.

4.4.4 U_{xx} , U_{xy} , U_{xz} , U_{yy} , U_{yz} inversion

The standard deviation of the data difference is 7.57 E for the U_{xx} component, 6.11 for the U_{xy} component, 8.51 E for the U_{xz} component, 8.73 E for the U_{yy} component, and 9.13 E for the U_{yz} component. The density model is created using 8994 data points and the data misfit is 6493.56, well within the 5% error margin.

The recovered density contrast ranges from -0.169 – 0.304 g/cm^3 (Table 4.2). A perspective view of the recovered model is shown in Figure 4.9. Two dense features are observed. The resulting model is most similar to the U_{xx} , U_{yz} , U_{zz} model but has a lower maximum density contrast. The centrally located dense feature corresponding to

the Asini prospect is more compact than the U_{xz} , U_{yz} , U_{zz} model with the boundaries being significantly tightened to the source location of the structure. The second dense feature located in the northwest corner is similar in size compared to the U_{xz} , U_{yz} , U_{zz} model.

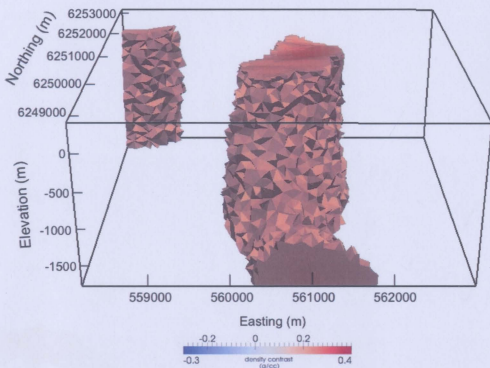


Figure 4.9: A perspective view of the recovered model for the unconstrained inversion results using the U_{xx} , U_{xy} , U_{xz} , U_{yy} , U_{yz} components showing the 0.20 g/cm^3 isosurface.

4.4.5 U_{xx} , U_{xy} , U_{xz} , U_{yy} , U_{yz} , U_{zz} inversion

Figure 4.10 shows the predicted gradiometer data and Figure 4.11 shows the data difference between the observed and predicted data. The standard deviation of the data difference is 7.31 E for the U_{xx} component, 5.88 E for the U_{xy} component, 8.13 E for the U_{xz} component, 8.20 E for the U_{yy} component, 8.76 E for the U_{yz} component, and 10.07 E for the U_{zz} component. The density model was created using 10784 data

points and the data misfit is 7810.89, well within the 5% error margin. The largest difference between the observed and predicted data is located over the northeastern edge of the Asini prospect troctolites in the U_{zz} component.

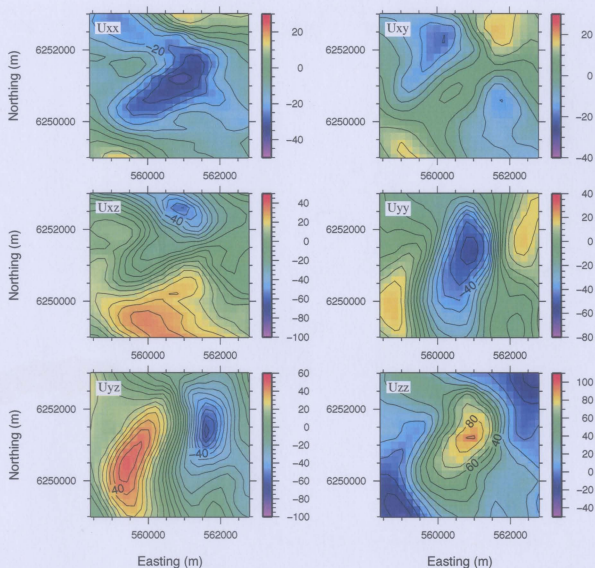


Figure 4.10: The predicted gradiometer data for the six component inversion. Units are in Eotvos. Contour interval is 5 E for U_{xx} , U_{xy} , U_{xz} , U_{yy} , and U_{yz} and 10 E for U_{zz} .

The recovered density contrast ranges from -0.181 – 0.324 g/cm^3 (Table 4.2). A perspective view of the recovered model is shown in Figure 4.12. Similar to all previous

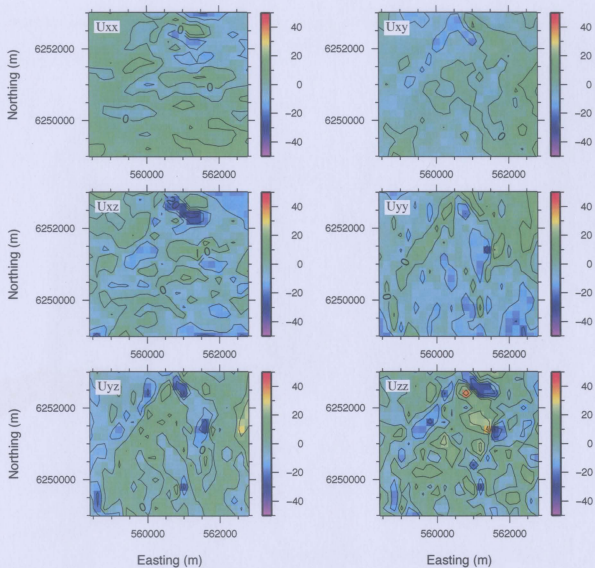


Figure 4.11: The data difference between the observed and predicted data for the six component inversion. Units are in Eotvos. Contour interval is 10 E for all components.

models, two dense features are observed. The resulting model is similar to U_{xx} , U_{yz} , U_{zz} model but has a lower maximum density contrast and boundaries that are significantly tightened to the source location of the structure. The resulting model is also similar to the U_{xx} , U_{xy} , U_{xz} , U_{yy} , U_{yz} model but with higher maximum density contrast and boundaries that are less compact. The second dense feature located in the northwest corner is similar in size to all previous models.

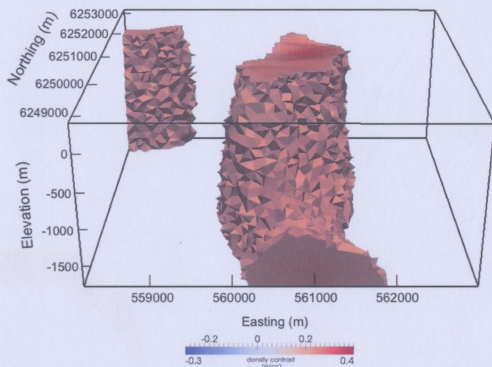


Figure 4.12: A perspective view of the recovered model for the unconstrained inversion results using the U_{xx} , U_{xy} , U_{xz} , U_{yy} , U_{yz} , U_{zz} components showing the 0.20 g/cm^3 isosurface.

4.5 Sarah prospect inversions

Following from the results obtained from the Mushuau intrusion and the successful inversion of six tensor components using the Asini prospect data, a subset of the data was selected to perform inversions over the Sarah prospect (Figure 4.13). The Sarah

prospect data set contains more data points and covers a larger geographic area than the Asini prospect data set.

4.5.1 Example 1

The modelling region is 6400 m by 6400 m by 2222 m (Easting by Northing by depth) and the topography has an elevation range of 422 m. The northern boundary overlaps with the Asini prospect model. A quality mesh was generated by using a minimum radius-edge ratio of $q = 2$ and a maximum tetrahedron volume of $a = 600,000$ giving a total of 299,801 cells. These are the same parameters used to generate the Asini prospect mesh.

Geologically-unconstrained gravity gradient inversions were performed using a zero-density initial model so that no assumptions were made about the geologic features. The density bounds were applied as a global constraint to the entire mesh and constrained to a lower bound of -5 g/cm^3 and an upper bound of 5 g/cm^3 . A distance weighting was used with $\beta = 1.5$ and $r_0 = 1$ (Equation 2.22).

4.5.2 U_{zz} inversion

The single-component inversion serves as a base model to compare whether the addition of more components increases the quality of the resulting model (Martinez and Li, 2011). The standard deviation of the data difference is 8.52 E, which is the same as the noise level observed in the full model inversion. The density model was created using 3547 data points and the data misfit is 2572.92, well within the 5% error margin.

The recovered density contrast ranges from -0.158 – 0.235 g/cm^3 (Table 4.3). A perspective view of the recovered model is shown in Figure 4.14 with all cells below 0.15 g/cm^3 removed for clarity. As expected, the result is similar to the southern portion of the model obtained by inverting the U_{zz} component for the entire data set

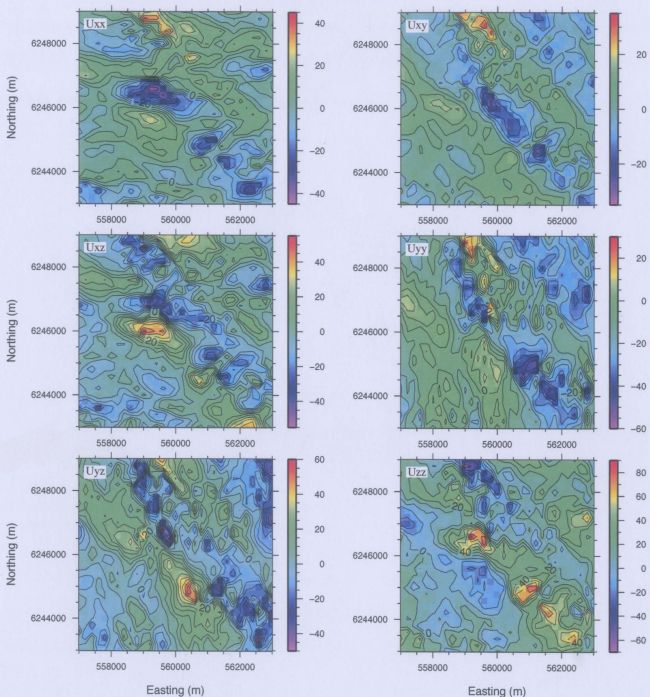


Figure 4.13: The subset of gradiometer data used to perform inversion over the Sarah prospect. Units are in Eotvos. Contour interval is 10 E for U_{xx} , U_{xy} , U_{xz} , U_{yy} , and U_{yz} and 20 E for U_{zz} .

(Figure 4.4). The remaining high density contrast shows five dense features. The four bodies striking northwest-southeast correspond to the troctolites of the Sarah prospect (labelled B through E on Figure 4.4). The fifth small dense feature is located along the northern boundary of the model in the region that overlaps with the Asini prospect model and may be associated with the troctolites of the Asini prospect.

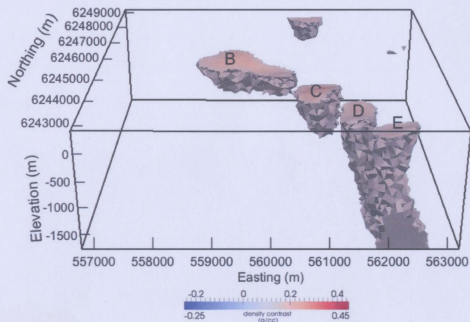


Figure 4.14: A perspective view of the Sarah prospect recovered model for the unconstrained inversion results using the U_{zz} component. All cells below 0.15 g/cm^3 have been removed.

Results could not be obtained using more than the single component due to computer memory limitations. Consequently, a second mesh with fewer cells was generated to attempt inversions with three or more tensor components.

4.5.3 Example 2: Layered model

The modelling region is 6400 m by 6400 m by 2222 m (Easting by Northing by depth) and the topography has an elevation range of 422 m. A quality mesh was generated using a minimum radius-edge ratio of $q = 2$. In order to reduce the number of

cells, a layered model was constructed (Figure 4.15). Different maximum tetrahedron volumes were applied to each layer resulting in a mesh with finer cells near the surface and coarser cells at depth (Table 4.1). The mesh has a total of 178,724 cells, 121,077 less cells than the previous mesh.

Geologically-unconstrained gravity gradient inversions were performed using a zero-density initial model so that no assumptions were made about the geologic features. The density bounds were applied as a global constraint to the entire mesh and constrained to a lower bound of -5 g/cm^3 and an upper bound of 5 g/cm^3 . A distance weighting was used with $\beta = 1.5$ and $r_0 = 1$ (Equation 2.22).

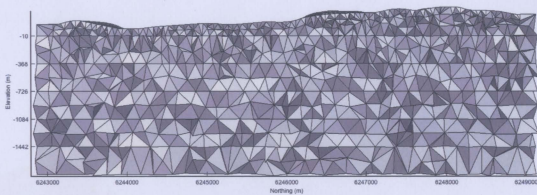


Figure 4.15: Vertical cross section through the layered model. The maximum tetrahedron volumes applied to each layer are listed in Table 4.1.

Table 4.1: The maximum tetrahedron volumes used in the layered model.

Layer	Depth to bottom (m)	Maximum volume (m^3)
1	-10	600,000
2	-368	1,000,000
3	-726	1,500,000
4	-1084	2,000,000
5	-1442	2,500,000
6	-1800	3,000,000

4.5.4 U_{zz} inversion

This result provides a comparison between the U_{zz} inversion result obtained using the previous initial model and the results obtained using the layered model. The standard deviation of the data difference is 8.51 E. The density model was created using 3547 data points and the data misfit is 2569.82, well within the 5% error margin.

Overall the model structure and density range are similar to that obtained in the previous U_{zz} inversion result (Figure 4.14). The recovered density contrast ranges from -0.153 – 0.235 g/cm^3 (Table 4.3). A perspective view of the recovered model is shown in Figure 4.16. Five dense features are observed. The four dense bodies striking southeast near the southern boundary of the model correspond to the troctolites of the Sarah prospect. The fifth dense feature is located along the northern boundary of the model and may be associated with the troctolites of the Asini prospect.

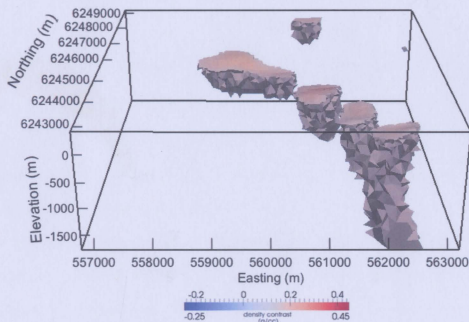


Figure 4.16: A perspective view of the Sarah prospect recovered model for the unconstrained inversion results using the U_{zz} component and the layered mesh. All cells below 0.15 g/cm^3 have been removed.

4.5.5 U_{xx} , U_{xy} , U_{yy} inversion

The recovered density contrast ranges from -0.191–0.405 g/cm³ (Table 4.3). The standard deviation of the data difference is 5.55 E for the U_{xx} component, 5.38 E for the U_{xy} component, and 6.50 E for the U_{yy} component. The density model was created using 10641 data points and the data misfit is 7657.17 well within the 5% error margin. A perspective view of the recovered model is shown in Figure 4.17. Six dense features are observed. The four dense bodies striking southeast near the southern boundary of the model correspond to the troctolites of the Sarah prospect. The fifth dense body is located near the northern boundary and is larger and deeper than that observed in the U_{zz} inversion. Again, it is likely associated with the troctolites of the Asini prospect. The sixth dense body is located near the eastern boundary. This body was not present in either of the previous Sarah prospect inversions using only the U_{zz} component, but it is present in the full model inversion (Figure 4.4).

4.5.6 U_{xz} , U_{yz} , U_{zz} inversion

The recovered density contrast ranges from -0.140–0.209 g/cm³. The standard deviation of the data difference is 8.16 E for the U_{xz} component, 7.50 E for the U_{yz} component, and 9.35 E for the U_{zz} component. The density model was created using 10641 data points and the data misfit is 7605.73, well within the 5% error margin. A perspective view of the recovered model is shown in Figure 4.18. Five dense features are observed. The four dense bodies striking southeast near the southern boundary of the model correspond to the troctolites of the Sarah prospect. Overall, these bodies are smaller than those recovered in inversions using the U_{zz} component and the inversions using the U_{xx} , U_{xy} , and U_{yy} components. The fifth dense body is located near the northern boundary and is larger than that observed in the U_{zz} inversions.

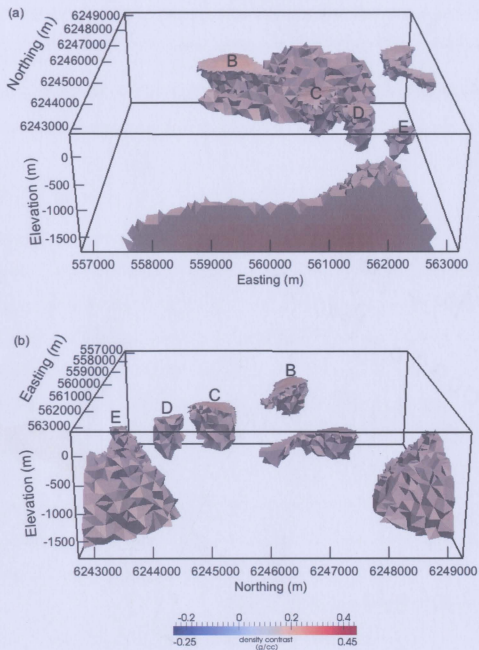


Figure 4.17: A perspective view of the Sarah prospect recovered model for the unconstrained inversion results using the U_{xx} , U_{xy} , U_{yy} components and the layered mesh. (a) The recovered density contrast looking north and (b) the recovered density contrast looking west. All cells below 0.15 g/cm^3 have been removed.

Again, it is likely associated with the troctolites of the Asini prospect.

4.5.7 Example 3: Layered model and decimated data set

The data set was decimated from 3547 observation points to 1774 observation points (Figure 4.19) to reduce the problem size and attempt five and six tensor component inversions. The layered model from the previous example is used here (Section 4.5.3).

4.5.8 U_{xx} , U_{xy} , U_{xz} , U_{yy} , U_{yz} inversion

The recovered density contrast ranges from -0.165 – 0.296 g/cm^3 (Table 4.3). The standard deviation of the data difference is 6.10 E for the U_{xx} component, 5.25 E for the U_{xy} component, 8.02 E for the U_{xz} component, 6.53 E for the U_{yy} component, and 7.65 E for the U_{yz} component. The density model was created using 8870 data points and the data misfit is 6413.39, well within the 5% error margin. A perspective view of the recovered model is shown in Figures 4.20. Five dense features are observed. The four dense bodies striking southeast near the southern boundary of the model correspond to the troctolites of the Sarah prospect. Overall, these bodies are smaller than those recovered in all previous inversions. The fifth dense body is located near the northern boundary and is larger than that observed in the U_{zz} inversions. Again, it is likely associated with the troctolites of the Asini prospect.

4.5.9 U_{xx} , U_{xy} , U_{xz} , U_{yy} , U_{yz} , U_{zz} inversion

Figure 4.21 shows the predicted gradiometer data and Figure 4.22 shows the data difference between the observed and predicted data. The standard deviation of the data difference is 5.79 E for the U_{xx} component, 5.20 E for the U_{xy} component, 8.24 E for the U_{xz} component, 6.29 E for the U_{yy} component, 7.47 E for the U_{yz} component,

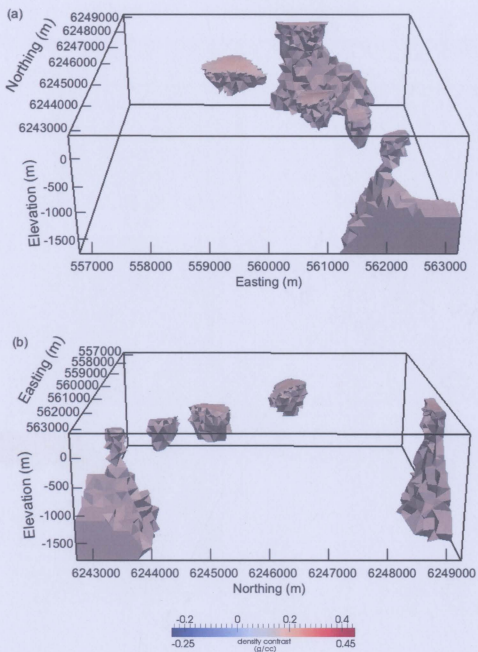


Figure 4.18: A perspective view of the Sarah prospect recovered model for the unconstrained inversion results using the U_{xx} , U_{yz} , U_{zz} components and the layered mesh. (a) The recovered density contrast looking north and (b) the recovered density contrast looking west. All cells below 0.15 g/cm^3 have been removed.

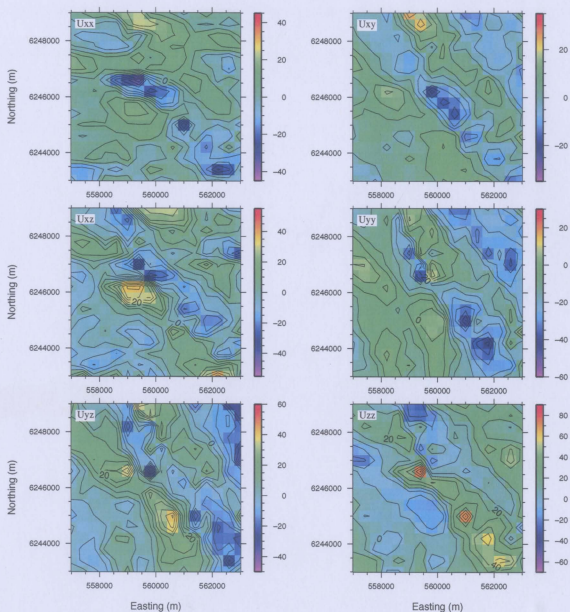


Figure 4.19: The decimated data set of gradiometer data used to perform inversion over the Sarah prospect. Units are in Eotvos. Contour interval is 10 E for U_{xx} , U_{xy} , U_{xz} , U_{yy} , and U_{yz} and 20 E for U_{zz} .

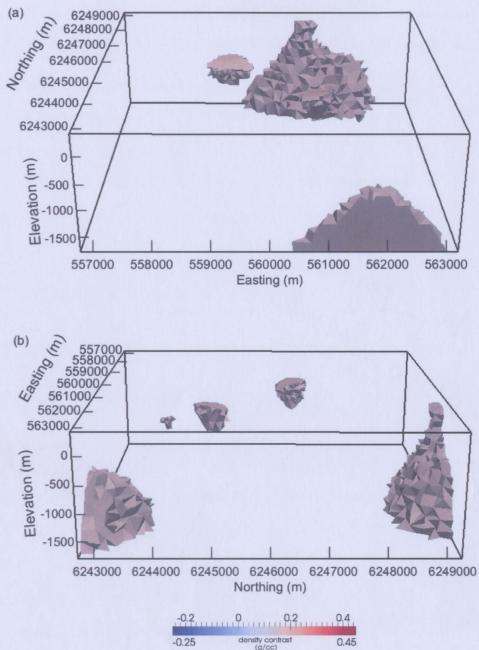


Figure 4.20: A perspective view of the Sarah prospect recovered model for the unconstrained inversion results using the U_{xx} , U_{xy} , U_{xz} , U_{yy} , U_{yz} components and the layered mesh. (a) The recovered density contrast looking north and (b) the recovered density contrast looking west. All cells below 0.15 g/cm^3 have been removed.

and 9.00 E for the U_{zz} component. The density model is created using 10644 data points and the data misfit is 7679.09, well within the 5% error margin.

The recovered density contrast ranges from -0.173–0.288 g/cm³ (Table 4.3). A perspective view of the recovered model is shown in Figure 4.23. Five dense features are observed. The four dense bodies striking southeast near the southern boundary of the model correspond to the troctolites of the Sarah prospect. Overall, these bodies are similar in size to those obtained in the U_{xz} , U_{yz} , U_{zz} inversion. The fifth dense body is located near the northern boundary and is larger than that observed in the U_{zz} inversions. Again, it is likely associated with the troctolites of the Asini prospect.

4.6 Summary of results

4.6.1 Generating unstructured tetrahedral meshes

The Mushuau intrusion mesh, Asini prospect mesh, and Sarah prospect mesh contained surfaces for the boundary of the modelling region and the topography. Creating the *poly* files for all three meshes was a simple process compared to the Voisey's Bay deposit forward modelling mesh since geological surfaces were not incorporated.

The size of the problem was again limited by available computer memory: if the problem was too large the memory necessary to solve the problem exceeded the available computer memory. Several approaches were taken to reduce the number of cells in the mesh and these are discussed in Section 4.6.3.

4.6.2 Geologically-unconstrained inversion

Only geologically-unconstrained inversions were performed to obtain subsurface models of the density contrast. This is a common first step in many exploration programs.

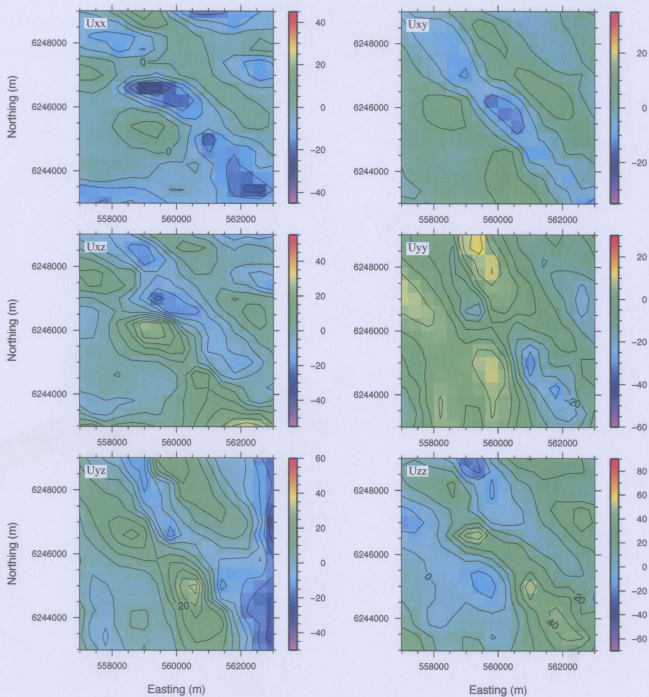


Figure 4.21: The predicted gradiometer data for the Sarah prospect six component inversion using the decimated data set. Units are in Eotvos. Contour interval is 10 E for U_{xx} , U_{xy} , U_{xz} , U_{yy} , and U_{yz} and 20 E for U_{zz} .

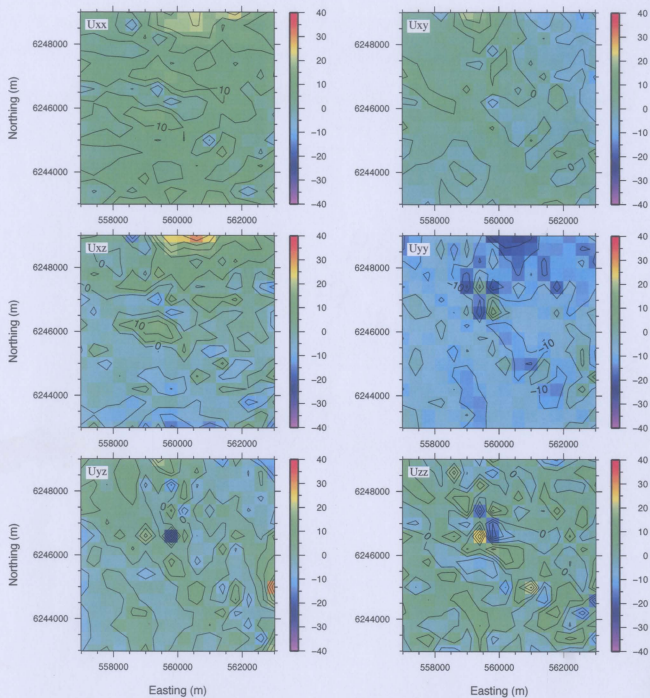


Figure 4.22: The data difference for the Sarah prospect between the observed and predicted data for the six component inversion. Units are in Eotvos. Contour interval is 5 E for all components.

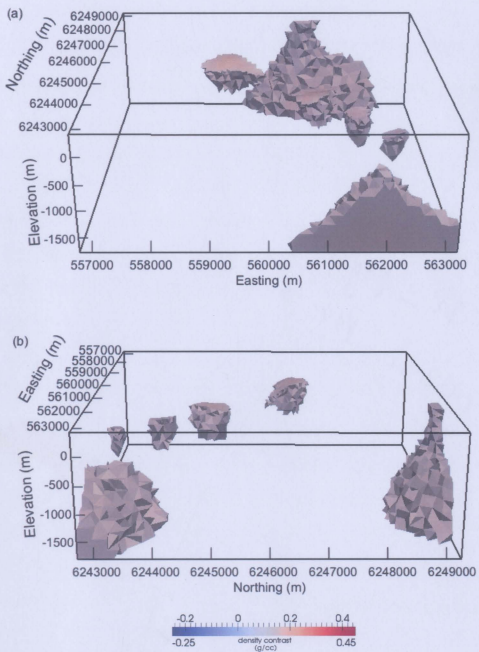


Figure 4.23: A perspective view of the Sarah prospect recovered model for the unconstrained inversion results using all six tensor components and the layered mesh. (a) Recovered density contrast looking north and (b) the recovered density contrast looking west. All cells below 0.15 g/cm^3 have been removed.

The recovered models are typical of minimum-structure inversion: the recovered features are diffuse and smeared out (Figure 4.23). Some of the key features are resolved in the models; such as the lateral location of the Asini and Sarah prospects. In the context of mineral exploration, this would be a valuable result in a green field situation but the value is diminished once a target has been identified and its delineation has begun.

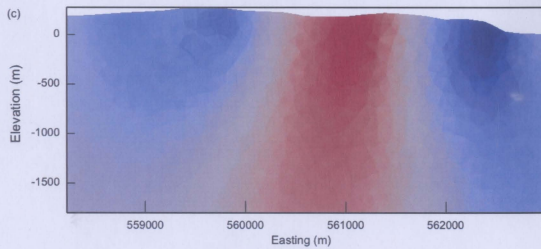
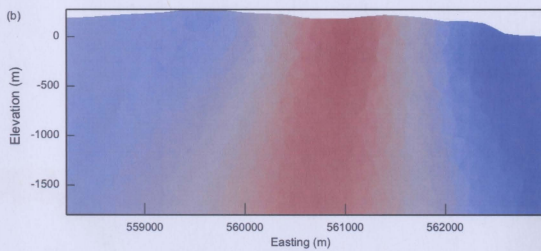
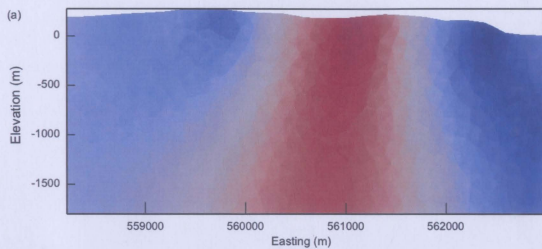
As demonstrated by the synthetic inversions of the Voisey's Bay deposits (Section 3.8.2), a reliable inversion result can only be recovered by including geological constraints as well as the standard mathematical constraints (Ash, 2007; McGaughey, 2007; Farquharson et al., 2008; Williams, 2008; Lelièvre, 2009; Williams et al., 2009). Geologically-constrained inversion was not investigated because geological data was not available.

4.6.3 Single versus multiple component inversion

The effect single and multiple components have on the resulting inverted model structure and recovered density contrast was investigated. Cross-sections are used to demonstrate the effect adding more tensor components has on the resulting models. The cross sections intersect the Asini prospect (Figure 4.23).

The Voisey's Bay geologically-unconstrained inversion results showed an increase in maximum density contrast when more tensor components were added. This was not observed in the Asini prospect or Sarah prospect inversion results (Tables 4.2 and 4.3). In the case of the Asini prospect, the highest maximum density contrast is observed in the U_{zz} inversion result and in the case of the Sarah prospect, the highest maximum density contrast is observed in the U_{xx} , U_{xy} , U_{yy} inversion result.

The main inhibitor to using multiple components to solve the inversion problem was computer memory. Several steps were taken to overcome the memory issues.



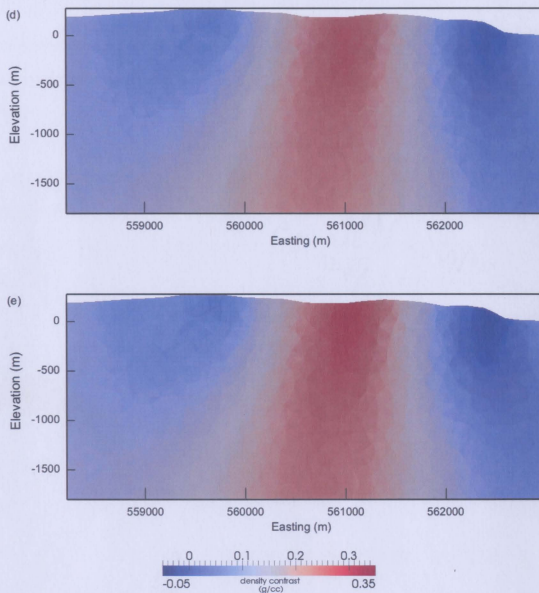


Figure 4.23: Vertical cross sections through the Asini prospect (Northing 6251800 m) to highlight the differences between single and multiple component inversion results: (a) U_{zz} ; (b) U_{xx} , U_{xy} , U_{yy} ; (c) U_{xz} , U_{yz} , U_{zz} ; (d) U_{xx} , U_{xy} , U_{xz} , U_{yy} , U_{yz} ; and (e) U_{xx} , U_{xy} , U_{xz} , U_{yy} , U_{yz} , U_{zz} .

First, the full dataset was divided into two smaller datasets to reduce the problem size (Asini prospect dataset and Sarah prospect dataset). The smaller Asini prospect dataset was successfully inverted using all six tensor components. Inversions were then attempted using the larger Sarah prospect dataset. Only the single tensor component inversion could be solved with available computer memory. Two steps were taken to reduce the Sarah prospect problem size. First, a layered model was created to decrease the number of cells in the mesh. This led to the successful inversion of three tensor components, but memory issues were encountered when five tensor components were inverted. The second step was to decimate the data set to decrease the number of data points and further reduce the problem size. The decimated data set combined with the layered model led to the successful inversion of five and six tensor components.

Table 4.2: Density range for the geologically-unconstrained Asini prospect inversions. Density values are in g/cm^3 .

Components	$\Delta\rho_{min}$	$\Delta\rho_{max}$
\bar{U}_{zz}	-0.212	0.350
U_{xx}, U_{xy}, U_{yy}	-0.112	0.285
U_{xz}, U_{yz}, U_{zz}	-0.219	0.340
$U_{xx}, U_{xy}, U_{xz}, U_{yy}, U_{yz}$	-0.169	0.304
$U_{xx}, U_{xy}, U_{xz}, U_{yy}, U_{yz}, U_{zz}$	-0.181	0.324

Table 4.3: Density range for the geologically-unconstrained Sarah prospect inversions. Density values are in g/cm^3 .

Components	$\Delta\rho_{min}$	$\Delta\rho_{max}$
<i>Initial model 1</i>		
U_{zz}	-0.158	0.235
<i>Layered mesh</i>		
U_{zz}	-0.153	0.235
U_{xx}, U_{xy}, U_{yy}	-0.191	0.405
U_{xz}, U_{yz}, U_{zz}	-0.140	0.209
<i>Layered mesh: decimated data set</i>		
U_{zz}	-0.147	0.218
$U_{xx}, U_{xy}, U_{xz}, U_{yy}, U_{yz}$	-0.165	0.296
$U_{xx}, U_{xy}, U_{xz}, U_{yy}, U_{yz}, U_{zz}$	-0.173	0.288

Chapter 5

Conclusions

The goals of this study were threefold:

1. Develop a forward modelling program for gravity gradient data capable of using an unstructured tetrahedral mesh. The forward modelling capability for gravity gradient data was inserted into an existing gravity inversion code to give a gravity gradient inversion code.
2. Demonstrate how unstructured tetrahedral meshes can be used to prescribe geological constraints.
3. Examine the utility of single and multiple component inversions.

5.1 Geophysical modelling

A new inversion program was developed in order to perform minimum-structure inversions using gravity gradient data and unstructured tetrahedral meshes. Very few gravity gradient inversion programs exist and those that do rely on the use of a rectilinear mesh (*e.g.* Li, 2001; Zhdanov et al., 2004). In order to use unstructured tetrahedral meshes, a forward modelling program was developed using an expression

for the gravitational attraction of a tetrahedron (Okabe, 1979). The program was written using Fortran and is a modification of the program used to solve for the vertical component of gravity (Appendix A). The inversion algorithm is capable of incorporating any known geological information as geological constraints and can perform either single or multiple component inversion to solve for a three dimensional distribution of density contrast.

The inversion algorithm was applied to a set of synthetic gravity gradiometry data generated from a model of the Voisey's Bay deposits and to a set of airborne gravity gradiometry data from the Mushuau intrusions, located north of Voisey's Bay in Labrador, Canada. The synthetic data inversions were used to demonstrate how unstructured tetrahedral meshes could be used to prescribe geological constraints and examine the utility of single and multiple component inversions. The real data inversions were used to test the algorithm on a real data set as well as examine the utility of single and multiple component inversions. Geologically-constrained inversion was not investigated using the real data set because geological data was not provided.

5.2 Geological constraints and unstructured tetrahedral meshes

An important capability of the *vinv* inversion program is its flexibility to include as much or as little geological information as is available into an initial density model and density bounds. This capability was utilized using the synthetic airborne gravity gradient data set based on the three dimensional model of the Voisey's Bay deposits.

Three dimensional geological Earth models typically use triangulated surfaces to represent geological contacts as determined by surface mapping and drilling because they are flexible enough to mimic complicated subsurface boundaries between geologic

units. The main advantage of unstructured tetrahedral meshes is their ability to easily use geological surfaces as geological constraints: unstructured tetrahedral meshes can honour geological contacts by directly incorporating the surfaces into the mesh. This is preferable to rectilinear meshes which always give a pixellated representation of the subsurface geology. However, unstructured tetrahedral meshes are not without their disadvantages: constructing a full geological model using Facetmodeller was time consuming and meshing problems were encountered using TetGen when the mesh contained several surfaces enclosing volumes of various sizes.

Geologically-unconstrained inversions can be used to locate possible anomalous regions during the early phases of exploration. Geologically-constrained inversion improves inversion results, but only if the density bounds are carefully selected. In other words, the density has to follow the geology. Adding geological constraints improves the recovered density contrast model over geologically-unconstrained results by better defining the density contrast as well as the size and depth extent of the ore bodies. As such, geological-constraints can be included to further refine the recovered density contrast model and enhance the potential for targeting. The final models are consistent with both the known geophysical and geological data and conversion from a rectilinear model to a triangulated geological model is not necessary.

5.3 Single and multiple component inversions

Another capability of the *vinv* inversion program is its flexibility to perform single or multiple component gravity gradient inversions. The program treats each new component as additional data so that if six tensor components are used at p observation locations, then the total number of data points is $6p$. Single and multiple component inversions were investigated using the synthetic data set based on the Voisey's Bay

deposits as well as the real data set from the Mushuau intrusions.

The Voisey's Bay geologically-unconstrained results demonstrate that incorporating the additional gravity gradient components into the inversion improves density results over single component inversion by better defining the size and depth extent of the ore bodies and troctolite. The results from multi-component inversion have tightened the boundaries of the recovered troctolite and ore bodies and shifted the centre of density contrast corresponding to the ore bodies towards the proper position indicated by the geologic model. The differences in the inversion models using single or multiple components were less apparent as more geological constraints were added. It is hard to judge whether or not the Asini prospect and Sarah prospect results were improved as more gravity gradient components were added to solve the inversion without available geological information for comparison.

The main inhibitor to using multiple gravity gradient components to solve the inversion problem was available computer memory. Several steps were taken to overcome the memory issues: large datasets were divided into multiple smaller datasets; layered models were constructed to decrease the number of cells in the mesh; datasets were decimated to further reduce the number of data points; and areas of well constrained geology used larger cell volumes to decrease the number of cells in the mesh.

Bibliography

- Ash, M.R. (2007). Constrained inversion of gravity data over the Ovoid and Mini-Ovoid in the Voisey's Bay Ni-Cu-Co deposit, Labrador. Unpublished. M.Sc. Thesis, Memorial University of Newfoundland
- Bell Geospace (2007). Inco Limited - final report acquisition and processing Air-FTG survey, Voisey's Bay, Canada; unpublished company report, Bell Geospace, 47 pages.
- Bell, R.E., Anderson, R, and Pratson, L. (1997). Gravity gradiometry resurfaces. The Leading Edge: 16, 55-59
- Bell, R.E. and Hansen, R.O. (1998). The rise and fall of early oil field technology: The torsion balance gradiometer. The Leading Edge: 17, 81-83
- Blakely, R.J. (1996). Potential Theory in gravity and Magnetic Applications. Cambridge University Press, 441 pp
- Boggs, D.B. and Dransfield, M.H. (2004). Analysis of errors in gravity derived from FALCON airborne gravity gradiometer. In Airborne Gravity 2004, the ASEG-PESA Airborne Gravity Workshop, Extended Abstracts, R. Lane (Ed): 135-141
- Boggs, D.B., Maddever, R.A.M, Lee, J.B., Turner, R.J., Downey, M.A., and Drans-

- field, M.H. (2007). First test survey results from the Falcon helicopter-borne airborne gravity gradiometer system. Preview: 126, 26-28
- Bosch, M. and McGaughey, J. (2001). Joint inversion of gravity and magnetic data under lithologic constraints. The Leading Edge: 20, 877-881
- Constable, S.C., Parker, R.L., and Constable, C.G. (1987). Occam's inversion: A practical algorithm for generating smooth models from electromagnetic sounding data. Geophysics: 52, 289-300
- DiFrancesco, D., Meyer, T., Christensen, A., and FitzGerald, D. (2009). Gravity gradiometry - today and tomorrow. Paper presented at 11th SAGA Biennial Technical Meeting and Exhibition, Swaziland
- Dransfield, M. (2007). Airborne gravity gradiometry in the search for mineral deposits. In Proceeding of Exploration 07: Fifth Decennial International Conference on Mineral Exploration, B. Milkereit (Ed): 341-354
- Evans-Lamswood, D.M., Butt, D.P., Jackson, R.S., Lee, D.V., Muggridge, M.G., Wheeler, R.I., and Wilton, D.H.C. (2000). Physical controls associated with the distribution of sulfides in the Voisey's Bay Ni-Cu-Co deposit, Labrador. Economic Geology: 95, 749-769
- Farquharson, C.G., Ash, M.R., and Miller, H. G. (2008). Geologically constrained gravity inversion for the Voisey's Bay ovoid deposit. The Leading Edge: 2, 64-69 (DOI: 10.1190/1.2831681)
- Fowler, C.M.R. (2005). The Solid Earth An Introduction to Global Geophysics. Cambridge University Press, 685 pp

- Fullagar, P.K. and Pears, G.A. (2007). Towards geologically realistic inversion. In Proceeding of Exploration 07: Fifth Decennial International Conference on Mineral Exploration, B. Milkereit (Ed): 444-460
- Fullagar, P.K. and Pears, G.A. (2010). From gravity gradient to density gradient. In Airborne Gravity 2010, the ASEG-PESA Airborne Gravity Workshop, Extended Abstracts, R. Lane (Ed): 79-86
- Kerr, A. and Ryan, B. (2000). Threading the eye of the needle: lessons from the search for another Voisey's Bay in Labrador, Canada. *Economic Geology*: 95, 725-748.
- Hansen, R. (1999). The gravity gradiometer: basic concepts and tradeoffs. *The Leading Edge*: 18, 478-479
- Hatch, D., Murphy, C., Mumaw, G., and Brewster, J. (2006). Performance of the Air-FTG system aboard an airship. Paper presented at AESC 2006, Melbourne, Australia.
- Huminicki, M.A.E., Sylvester, P.J., Lastra, R., Cabri, L.J., Evans-Lamswood, D., and Wilton, D.H.C. (2008). First report of platinum-group minerals from a hornblende gabbro dyke in the vicinity of the Southeast Extension Zone of the Voisey's Bay Ni-Cu-Co deposit, Labrador. *Mineralogy and Petrology*: 92, 129-164
- Kerr, A. (2003). Voisey's Bay and the nickel potential of Labrador: A summary for the nonspecialist. Current Research, Newfoundland Department of Mines and Energy, Geological Survey, Report 02-I, 231-239
- Lelièvre, P.G. (2009). Integrating geologic and geophysical data through advanced constrained inversions. Unpublished. Ph.D. Thesis, The University of British Columbia

- Lelièvre, P.G., Farquharson, C.G., and Hurich, C.A. (2010). Joint inversion of seismic travel times and gravity data on unstructured grids with application to mineral exploration. Paper presented at SEG Denver 2010 Annual Meeting, Society of Exploration Geophysicists.
- Lelièvre, P.G., Carter-McAuslan, A., Tycholiz, C., Farquharson, C.G., and Hurich, C.A. (2012). Refining 3D Earth models through constrained joint inversion on flexible unstructured meshes. Paper presented at KEGS Symposium 2012, Toronto, Ontario, Canadian Exploration Geophysical Society
- Li, C., Lightfoot, P.C., Amelin, Y., Naldrett, A.J. (2000). Contrasting petrological and geochemical relationships in the Voisey's Bay and Mushuau intrusions, Labrador, Canada: implications for ore genesis. *Economic Geology*: 95, 771-799
- Li, X. (2010). Efficient 3D gravity and magnetic modeling. Paper presented at Electromagnetic, Gravity, and Magnetic (EGM) Methods International Workshop.
- Li, Y. (2001). 3-D inversion of gravity gradiometer data. Paper presented at SEG San Antonio 2001 International Exposition and Annual Meeting, Society of Exploration Geophysicists.
- Li, Y., and Oldenburg, D.W. (1996). 3-D inversion of magnetic data. *Geophysics*: 61, 394-408
- Li, Y., and Oldenburg, D.W. (1998). 3-D inversion of gravity data. *Geophysics*: 63, 109-119
- Li, Y., and Oldenburg, D.W. (2003). Fast inversion of large scale magnetic data using wavelet transforms and a logarithmic barrier method. *Geophysical Journal International*: 152, 251-265

- Martinez, C., Li, Y., Krahenbuhl, R., and Braga, M. (2010). 3D inversion of airborne gravity gradiometry for iron ore exploration in Brazil. Paper presented at SEG 80th Annual International Meeting.
- Martinez, C., and Li, Y. (2011). Inversion of regional gravity gradiometer data over the Vredefort Impact Structure, South Africa. Paper presented at SEG San Antonio 2011 Annual Meeting, Society of Exploration Geophysicists.
- McGaughey, J. (2007). Geological models, rock properties, and the 3D inversion of geophysical data. In Proceeding of Exploration 07: Fifth Decennial International Conference on Mineral Exploration, B. Milkereit (Ed): 473-483
- Murphy, C.A. (2004). The Air-FTG airborne gravity gradiometer system. In Airborne Gravity 2004 - Abstracts from the ASEF-PESA Airborne Gravity 2004 Workshop, R.J. Lane (Ed). Geoscience Australia Record: 2004/18, 7-14
- Murphy, C.A., Brewster, J., and Robinson, J. (2007). Evaluating Air-FTG survey data: bringing value to the full picture. Preview: 126, 24-25
- Nabighian, M.N., Ander, M.E., Grauch, V.J.S., Hansen, R.O., LaFehr, T.R., Li, Y., Pearson, W.C., Peirce, J.W., Phillips, J.D., and Ruder, M.E. (2005). Historical development of the gravity method in exploration. Geophysics: 70, 63ND-89ND
- Nagy, D. (1966). The gravitational attraction of a right rectangular prism. Geophysics: 31, 362-371
- Nettleton, L.L. (1942). Gravity and magnetic calculations. Geophysics: 7, 293-310
- Okabe, M. (1979). Analytical expressions for gravity anomalies due to homogeneous polyhedral bodies and translations into magnetic anomalies. Geophysics: 44, 730-741

- Inversion for applied geophysics: a tutorial. In *Near Surface Geophysics*, D.K. Butler (Ed), Society of Exploration Geophysicists, Tulsa, Oklahoma
- Pawlowski, B. (1998). Gravity gradiometry in resource exploration. *The Leading Edge*: 17, 51-52
- Pedersen, L.B., and Rasmussen, T.M. (1990). The gradient tensor of potential field anomalies: some implications on data collection and data processing of maps. *Geophysics*: 55, 1558-1566
- Pilkington, M. (2012). Analysis of gravity gradiometer inverse problems using optimal design measures. *Geophysics*: 77, G25-G31
- Rawlings-Hinchey, A.M., Sylvester, P.J., Myers, J.S., Dunning, G.R., Kosler, J. (2003). Paleoproterozoic crustal genesis: calc-alkaline magmatism of the Torngat Orogen, Voisey's Bay area, Labrador. *Precambrian Research*: 125, 55-85
- Reynolds, J.M. (1997). *An Introduction to Applied and Environmental Geophysics*. John Wiley & Sons, 796 pp
- Ryan, B. (2000). The Nain-Churchill boundary and the Nain Plutonic Suite: A regional perspective on the geologic setting of the Voisey's Bay Ni-Cu-Co deposit. *Economic Geology*: 95, 703-724
- Shewchuk, J.R. (1996). Triangle: Engineering a 2D quality mesh generator and Delaunay triangulator. In *Applied Computational Geometry: Towards Geometric Engineering*, M.C. Lin and D. Manocha (Ed), First ACM Workshop on Applied Computational Geometry, Springer-Verlag, Berlin: 1148, 203-222
- Shewchuk, J.R. (2002). Delaunay refinement algorithms for triangular mesh generation. *Computational Geometry: Theory and Applications*: 22, 21-74

- Si, H. and Gartner, K., (2004). An algorithm for three-dimensional constrained Delaunay tetrahedralizations. Paper presented at International Conference on Engineering Computational Technology.
- Si, H., and Gartner, K., (2005). Meshing piecewise linear complexes by constrained Delaunay tetrahedralization. Paper presented at International Meshing Roundtable
- Si, H. (2007). Tetgen: A quality tetrahedral mesh generator and 3D Delaunay triangulator. <http://tetgen.berlios.de>, accessed in 2011.
- Telford, W.M., Geldart, L.P., and Sherriff, R.E. (1990). Applied Geophysics. Cambridge University Press, 770 pp
- West, G.F., and Bailey, R.C. (1988). Inverse methods in geophysical exploration. In Exploration 87, G.D. Garland (Ed.), Ontario Geological Survey Special: 3, 191-212
- Williams, N.C. (2008). Geologically-constrained UBC-GIF gravity and magnetic inversions with examples from the Agnew-Wiluna greenstone belt, western Australia. Unpublished. Ph.D. Thesis, The University of British Columbia
- Williams, N.C., Oldenburg, D., and Lelievre, P. (2009). Constraining gravity and magnetic inversions for mineral exploration using limited geological data. Paper presented at 20th ASEG Conference in Adelaide, Australia.
- Zhdanov, M.S., Ellis, R., and Mukherjee, S. (2004). Three-dimensional regularized focusing inversion of gravity gradient tensor component data. Geophysics: 69, 925-937

Appendix A

Forward modelling program:

gravity_fwd

The program *gravity_fwd* was written by Dr. Peter Lelièvre, a post-doctoral fellow at Memorial University of Newfoundland. The program can be used to generate the vertical component of gravity, the gravity gradient tensor, or magnetic data from an unstructured tetrahedral grid for a specified set of observation points by summing the contribution from each cell (Equation 2.12). The portion of the program used to generate the vertical component of gravity was written by Hormoz Jahandari, a Ph.D Candidate in Dr. Colin Farquharson's research group. Hormoz Jahandari's program was then modified to generate the gravity gradient by the author (Cassandra Ty-choliz). The original gravity gradient code is included on attached disc; the original code was modified by Dr. Peter Lelièvre to be included within the *gravity_fwd* program. The program *gravity_fwd* references an input file *gravity_fwd.inp*; the contents of an example file are shown in Table A.1.

The data type is defined by the *ismag* and *istensor* parameters. The *ismag* parameter specifies if the forward modelling is for magnetic or gravity data. The parameter

Table A.1: The *gravity_fwd.inp* input file used for forward modelling. The contents of the file control parameters and reference necessary elements for executing the *gravity_fwd* forward modelling program.

ismag	'f'	! set to true if modelling magnetic data instead of gravity
istensor	't'	! specifies the type of gravity data
zdir	1	! specifies the coordinate system
gridtype	'unstructured'	! the type of grid
meshfile	'meshfile.node'	! file containing mesh information
modelfile	'modelfile.ele'	! file containing model information
obsfile	'obsfile.node'	! file containing the observation locations
ai	1	! attribute index to use as the model
gmul	1.0	! multiplicative scalar to convert model to density
gadd	0.0	! additiative scalar to convert model to density
comps	ttttt	! specifies which tensor components to use

is set to f to model gravity or gravity gradient data and t to model magnetic data. The *istensor* parameter specifies the type of gravity data to forward model. The parameter is set to t to model gravity gradient data or f to model the vertical component of gravity.

The unstructured tetrahedral grid is defined by the *zdir*, *gridtype*, *meshfile*, and *modelfile* parameters. A *zdir* parameter equal to 1 indicates the x-axis points to the east, y-axis to the north, and z-axis vertically upward; whereas a *zdir* of -1 indicates the x-axis points to the north, y-axis to the east, and z-axis vertically downward. The *gridtype* parameter can be specified as unstructured or rectilinear. For the purposes of this project only unstructured grids were used. The *meshfile* and *modelfile* parameters refer to *node* and *ele* files, respectively, generated using TetGen (Section 2.2.2).

The density values are contained in the *modelfile* as an attribute index, *ai*. If m is the model value (attribute index) in a particular cell, then the density used for that cell is $density = gmul * m + gadd$. If the model values, m are the true density values, then *gadd* can be set to the background density value in order to obtain the

anomalous density relative to the background density.

The *obsfile* parameter specifies a *node* file that contains observation point information. The file contains information on include the number of observation points and their coordinates (node index, Easting, Northing, elevation).

Two output files are produced by *gravity_fwd*. Both files contain the forward modelled data information. The *node* file contents include the number of data points, their coordinates, and six gravity gradient tensor components (node index, Easting, Northing, elevation, U_{xx} , U_{xy} , U_{xz} , U_{yy} , U_{yz} , U_{zz}). The *vtu* file is used for visualization purposes in a program called ParaView.

Appendix B

Inversion program: *vinv*

The inversion program, *vinv* (Versatile INVersion code) was written by Dr. Peter Lelièvre using Fortran95 and can be used for single or joint data inversions. The program requires a number of input files to specify the parameters of the subsurface of the area of interest. The program is flexible enough to incorporate geological constraints using an initial model. The program *vinv* references an input file *vinv.inp* which in turn references a second file *gravity_inv.inp*; the contents of example files are shown in Tables B.1 and B.2.

The unstructured tetrahedral grid is defined by the *zdir*, *gridtype*, *meshfile*, *modelfile*, and *neighfile* parameters. A *zdir* parameter equal to 1 indicates the x-axis points to the east, y-axis points to the north, and z-axis points vertically upward. The *gridtype* parameter can be specified as unstructured or rectilinear. For the purposes of this project only unstructured grids were used. The *meshfile*, *modelfile*, and *neighfile* parameters refer to *node*, *ele*, and *neigh* files, respectively, generated using TetGen (Section 2.2.2).

The *initfile* and *boundsfile* parameters are used to perform constrained inversions and refer to an initial density model and density bounds contained in an *ele* file (node

Table B.1: The *vinv.inp* input file. The contents of the file control parameters and reference necessary elements for executing the *vinv* minimum-structure inversion program. This file calls on the *gravity_fvd.inp* file for additional inversion parameters.

<i>zdir</i>	1	! specifies the coordinate system
<i>gridtype</i>	'unstructured'	! the type of grid (the other option is 'rectilinear')
<i>meshfile</i>	'meshfile.node'	! file containing mesh information
<i>modelfile</i>	'modelfile.ele'	! file containing model information
<i>neighfile</i>	'neighfile.neigh'	! another file containing mesh information
<i>ndatasets</i>	1	! number of data sets to invert
<i>datatype</i>	1 'gg'	! type of data
<i>datainp</i>	1 ' <i>gravity_inv.inp</i> '	! input file
<i>chifact</i>	1 1.0	! normalized target misfit
<i>initfile</i>	1 'initfile.ele'	! file containing an initial model
<i>initindex</i>	1 1	! attribute index to use in an initial model file
<i>initvalue</i>	1 0.0	! initial model value
<i>usebounds</i>	't'	! set to true 't' for bound-constrained inversion
<i>boundsfile</i>	1 'boundsfile.ele'	! file containing model bounds
<i>lowerindex</i>	1 1	! attribute index for lower bound in a boundsfile
<i>upperindex</i>	1 2	! attribute index for upper bound in a boundsfile
<i>lowervalue</i>	1 0.0	! lower bound value for entire mesh
<i>uppervalue</i>	1 5.0	! upper bound value for entire mesh
<i>betainit</i>	0.0	! initial beta value

index, node 1, node 2, node 3, node 4, initial density). These values are determined from any available geological information. Default values are used where information is unavailable. The initial model consists of the best estimate of the arithmetic mean density value in each cell in the model. Bounds impose a range of values if the density varies or is difficult to define. Bounds can be applied to individual cells or to the entire mesh (Williams et al., 2009). If density bounds are applied to individual cells, *boundfile* refers to an *ele* file containing the density bound information (node index, node 1, node 2, node 3, node 4, lower bound, upper bound). The parameters *lowerindex* and *upperindex* indicate which attribute index to use for the lower and upper density bound for that particular cell. If applying the bounds to the entire

Table B.2: The *gravity_inv.inp* input file used for minimum-structure inversion. The contents of the file controls depth/distance/sensitivity weighting. It also specifies the data file and which tensor components to invert.

istensor	't'	! specifies the type of gravity data
zdir	1	! specifies the coordinate system
gridtype	'unstructured'	! the type of grid (the other option is 'rectilinear')
meshfile	''	! file containing mesh information
modelfile	''	! file containing model information
datafile	''	! file containing the data information
ai	1	! attribute index to use as the model
gmul	1.0	! multiplicative scalar to convert model to density
gadd	0.0	! additive scalar to convert model to density
wmode	'distance'	! defines what type of weighting is used
wbeta	1.0	! distance/sensitivity weighting strength
wnorm	2.0	! distance/sensitivity weighting norm
wpower	2.0	! depth/distance/sensitivity weighting power
wzero	1.0	! depth/distance/sensitivity weighting z0/r0
comps	ttttt	! specifies which tensor components to use

mesh, the parameter *boundsfile* is set to null. In this case, the parameters *lowervalue* and *uppervalue* are used to specify the lower and upper density bounds applied to the entire mesh.

The *chifact* parameter controls the acceptable misfit between observed and predicted data for the whole data set. For a synthetic data set, with random Gaussian noise added, a *chifact* of 1.0 is usually acceptable. Otherwise, with a real data set, the *chifact* can be changed to better fit the data or limit the amount of spurious structure in the model.

The *ndatasets*, *datatype* and *datainp* parameters specify the type of data to invert and the input file to find additional data parameters. For a single data inversion, *ndatasets* is set to 1. If using gravity gradient data, the *datatype* is set to *gg*. Within the *gravity_inv.inp* file, the *datafile* parameter specifies the data contained in a *node* file with information on the observation locations, gravity gradient data, and data

uncertainties (node index, Easting, Northing, elevation, U_{xx} , σ_{xx} , U_{xy} , σ_{xy} , U_{xz} , σ_{xz} , U_{yy} , σ_{yy} , U_{yz} , σ_{yz} , U_{zz} , σ_{zz}).

Parameters *gmul* and *gadd* are set to 1.0 and 0.0, respectively, in order to recover the density contrast.

The *wmode* parameter specifies the type of weighting to use and can be set to *none*, *depth*, *distance*, or *sensitivity*. When *wmode* is set to *none*, the *wbeta*, *wnorm*, *wpower*, and *wzero* parameters are ignored. If depth weighting (Equation 2.20) is used then *wzero* is the average survey height in the input coordinate system (z_0 in Equation 2.20) and *wpower* is an adjustable parameter used to match the weighting function to the kernel's decay with depth (β in Equation 2.20). If distance weighting (Equation 2.21) is used then *wzero* is some small value such as half the smallest cell dimension (r_0 in Equation 2.21), *wpower* is chosen to match the weighting function to the kernel's decay with distance (β in Equation 2.21), *wnorm* = 2, and *wbeta* = 1. For the purposes of this project, sensitivity weighting was not used.

Finally, the *comps* parameter specifies which tensor components to use in the inversion. If all six components are used in the inversion, *comps* is set to *ttttt*. If only the U_{zz} component is used, *comps* is set to *fffft*.

Appendix C

Voisey's Bay models

C.1 Forward modelling files

The files provided on the attached disc correspond to the synthetic airborne data in Section 3.3. The *Forward modelling* folder contains an *Input files* folder and an *Output files* folder. The *Input files* folder contains the input (*inpfile*), model (*elefile*, *nodefile*, and *polyfile*), and observation point (*nodefile*) files used in the *gravity_fwd* program. The *Output files* folder contains the synthetic airborne data. The synthetic airborne data corresponds to Figure 3.4 and the noise contaminated synthetic data corresponds to Figure 3.5. The *vtufile* is used for visualization in Paraview.

C.2 Data misfit versus model norm

A series of preliminary inversions using a coarse mesh and a range of *chifact* values were carried out in order to select the optimal regularization parameter using a plot of data misfit versus the model objective function. The ideal *chifact* value will reproduce will reproduce a data misfit value that equals the total number of data points multiplied by the *chifact* value to within a 5% error margin. A *chifact* value of one

was found to provide the optimal trade-off between model structure and data misfit (Figure C.1).

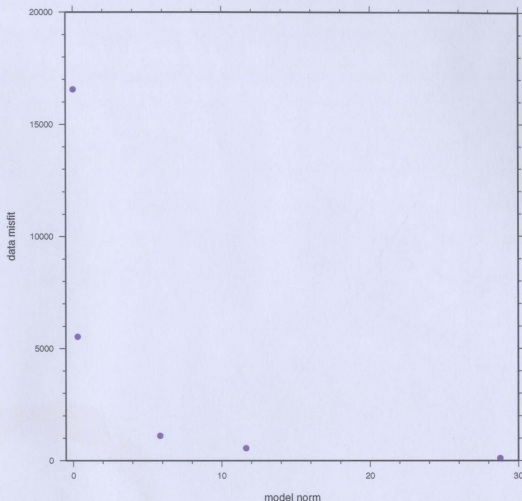


Figure C.1: Trade-off curve for Voisey's Bay inversions using $chifact = 10, 5, 1, 0.5, 0.1$ (left to right).

C.3 Inversion files

The files provided on the attached disc correspond to the geologically-unconstrained inversions (Sections 3.4), constrained using drill hole data (Section 3.5), constrained using the troctolite surface (Section 3.6), and constrained using the true model (Section 3.7). The *Inversion* folder contains four folders, one for each example. Within

each examples folder there is an *Input files* folder and an *Output files* folder. The *Input files* folder contains the input files used in the *vinv* program. There are 15 input files (two for each of the five different tensor component combinations) in the geologically-unconstrained, constrained using drill hole data, and true model folders. There are 17 input files in the troctolite surface folder; the two extra files are for the example in Section 3.6.7. The *Output files* folder contains the recovered density models (*elefile* and *vtufile*) and predicted gravity gradiometer data (*nodefile* and *vtufile*). There are 20 density model files and predicted gravity gradiometer data files in the geologically-unconstrained, constrained using drill hole data, and true model folders. There is 24 density model files and predicted data files; the four extra files are for the example in Section 3.6.7.

Appendix D

Mushuau models

D.1 Coordinate transform

The coordinate transform was determined experimentally. A preliminary inversion was completed using the U_{zz} component only. The resulting density model was forward modelled using *gravity_fwd*. The forward modelled data was used to determine the coordinate transform from a left hand coordinate system to a right hand coordinate system: the U_{xx} and U_{yy} data were switched and the U_{xz} and U_{yz} data were switched.

D.2 Data misfit versus model norm

A series of preliminary inversions using a coarse mesh and a range of *chifact* values were carried out in order to select the optimal regularization parameter using a plot of data misfit versus the model objective function. The ideal *chifact* value will reproduce a data misfit value that equals the total number of data points multiplied by the *chifact* value to within a 5% error margin. A *chifact* value of 0.75 was found to provide the optimal trade-off between model structure and data misfit (Figure D.1)

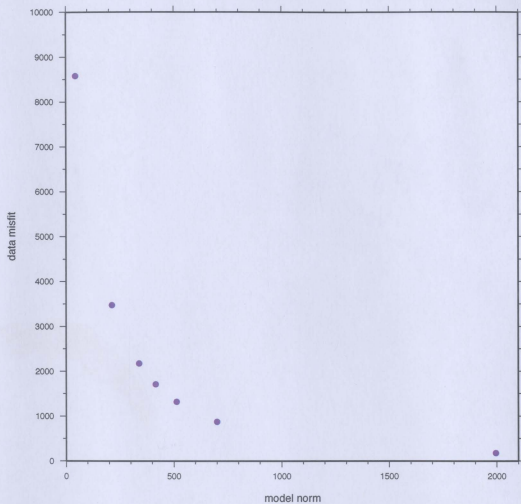


Figure D.1: Trade-off curve for Asini project inversions using $chifact = 5, 2, 1.25, 1, 0.75, 0.5, 0.1$ (left to right).

D.3 Inversion files

The files provided on the attached disc correspond to the Mushuau Intrusion inversion (Section 4.3), the Asini prospect inversions (Section 4.4), and the Sarah model inversions (Section 4.5).

The *Mushuau Intrusion* folder contains a *Model* folder and an *Inversion* folder. The *Model* folder contains the corresponding *polyfile*, *elefile*, *neighfile*, *nodefile*, *vtufile* for the Mushuau Intrusion inversion starting model. The *Inversion* folder contains an *Input files* folder and an *Output files* folder. The *Input files* folder contains the input files used in the *vinv* program (*inpfile*). The *Output files* folder contains two density model files (*elefile* and *vtufile*) and two predicted gravity gradiometer data for the single component inversion (*nodefile* and *vtufile*).

The *Asini prospect* folder contains a *Model* folder and an *Inversion* folder. The *Model* folder contains the corresponding *polyfile*, *elefile*, *neighfile*, *nodefile*, *vtufile* for the Asini prospect inversion starting model. The *Inversion* folder contains an *Input files* folder and an *Output files* folder. The *Input files* folder contains the input files used in the *vinv* program. The *Output files* folder contains the density model files and the predicted gravity gradiometer data. There are ten density model files; two for each of the five different tensor combinations. There are also ten predicted gravity data files; two for each of the five different tensor combinations.

The *Sarah prospect* folder contains a *Fine mesh* folder and a *Layered mesh* folder. Both folders contain a *Model folder* with the corresponding model files and an *Inversion folder* with corresponding *Input files* and *Output files* folders. In the *Output* folder for the *Fine mesh* there are two density model files and two predicted data models for the single component inversion. In the *Layered mesh* folder there are two folders: one for the *Full data set* examples and one for the *Decimated data set* examples. In the *Output files* folder for the *Full data set* examples there are six density

model files and six predicted data files; two each for the single and three component inversions. In the *Output files* folder for the *Decimated data set* examples there are six density model files and six predicted data files; two each for the single, five, and six component inversions.



